Université de Montréal

Optical pH sensor based on carbon nanomaterials and metal redox chemistry

Par
Natasha Shoghi

Département de Chimie
Faculté des arts et des sciences

Thèse présentée à la Faculté des études supérieures et postdoctorales en vue de l'obtention du grade de doctoral ès sciences (Phd.) en chimie

March 2021

Université de Montréal

Département de Chimie Faculté des Arts et Sciences

Cette thèse intitulée

Optical pH sensor based on carbon nanomaterials and metal redox chemistry.

Présentée par

Natasha Shoghi

A été évalué(e) par un jury composé des personnes suivantes

Dominic Rochefort

Président-rapporteur

Richard Martel

Directeur de recherche

Antonella Badia

Membre du jury

Eric Anglaret

Examinateur externe

Résumé

La plupart des capteurs de pH fonctionnent dans des conditions potentiométriques en utilisant un schéma simple à deux électrodes. Plus généralement, un pH mètre classique mesure le potentiel électrique de la solution à l'aide d'une électrode en verre (pH) contre une autre électrode (référence), dont le potentiel électrochimique est connu et insensible au pH. Les capteurs de pH modernes sont robustes, précis et peu coûteux, mais ils sont limités par les tailles macroscopiques des électrodes. Ils nécessitent également des contacts électriques et sont souvent affectés par des erreurs liées à la contamination des petites jonctions liquides des électrodes. Cette thèse concerne l'amélioration des mesures de pH aux interfaces nanométriques et explore la miniaturisation du capteur de pH pour des mesures (optiques) locales et à distance. En tirant parti d'une technique optique non destructive basée sur la spectroscopie Raman et de la chimie redox des métaux, ce travail vise à développer un capteur de pH à distance à base de nanomatériaux de carbone, à savoir le nanotube de carbone à simple paroi (SWCNT) et le graphène monofeuillet.

En utilisant la réponse Raman très sensible des SWCNT métalliques, nous avons conçu une sonde optique sensible au pH constituée d'un SWCNT en contact direct avec un couple redox platine. Lorsqu'elle est placée dans une solution tampon, la sonde Pt-SWCNT montre un fort décalage Raman de la bande G du nanotube en fonction du pH, qui est attribué au dopage par transfert de charge de l'électrode de référence SWCNT. La mesure du potentiel référencé est démontrée à l'aide d'une version nanométrique de l'électrode Pt-SWCNT, ainsi que par la surveillance précise du pH dans des solutions de différentes forces ioniques. Des expériences contrôlées à force ionique constante montrent des mesures de pH sur toute la gamme entre 1 et 12 avec une précision allant jusqu'à ± 500 mpH. Cette étude explore également l'influence de différents métaux de transition (Pt, Ru et Pd), du caractère électronique des SWCNTs et des substrats de soutien sur les détection de pH. Un modèle basé sur le transfert d'électrons entre le système métallique redox et le SWCNT est proposé et testé à l'aide de mesures de conductance électrique.

En raison des propriétés exceptionnelles du graphène, telles qu'un comportement semi-métallique et une surface relativement inerte, le graphène a été sélectionné comme deuxième nanomatériau pour approfondir la détection Raman-pH. À partir de l'étude avec les SWCNT, qui détermine qu'une réponse optimale est obtenue avec le couple redox Pt / PtO, nous explorons la réponse Raman du graphène recouvert d'une fine couche de Pt dans différentes solutions tampons avec pH

entre 1 et 12. Les spectres montrent des preuves claires de transfert de charge et dopage du graphène en contact avec le couple redox platine. Un décalage Raman significatif avec le pH est noté dans la région de la bande G et également dans la bande D, ce qui est cohérent avec le comportement trouvé avec le système Pt-SWCNT métallique. Une analyse du décalage Raman permet de mieux comprendre le comportement de dopage observé à différents pH. L'analyse fournit une estimation du potentiel et confirme le comportement Nerstien du capteur de pH.

La détection de pH redox à l'échelle nanométrique avec des nanomatériaux de carbone permet de résoudre les principales limitations mises en évidence ci-dessus, à savoir la couverture de toute la gamme de pH et une miniaturisation claire du capteur jusqu'à l'échelle nanométrique. Bien que la précision nécessite une amélioration supplémentaire, ce travail démontre pour la première fois un schéma de détection optique du pH qui est analogue à un capteur de pH conventionnel équipé d'une référence interne intégrée.

Mots-clés : capteur de pH, nanotubes de carbone à paroi simple, graphène, couple redox Pt, spectroscopie Raman.

Abstract

Most pH sensors operate under potentiometric conditions using a simple two-electrode scheme. More generally, a conventional meter measures the electrical potential of the solution using a glass electrode (pH) against another electrode (reference), whose electrochemical potential is known and insensitive to pH. Modern pH sensors are robust, accurate and low cost, but they are limited by the macroscopic electrode size. They also require electrical contacts and they are often affected by errors associated with the contamination of the small electrode liquid junctions. This thesis targets pH measurements at nanoscale interfaces and explores the miniaturization of the pH sensor for local and remote (optical) measurements. By taking advantage of a non-destructive optical technique based on Raman spectroscopy and of the redox chemistry of metals, this work aims to develop a remote pH sensor based on carbon nanomaterials, namely the single walled carbon nanotube (SWCNT) and the graphene in the form of a single layer.

By making use of the highly sensitive Raman response of metallic SWCNTs, we devised a pH responsive optical probe consisting of a SWCNT in direct contact with a platinum redox couple. When placed in a buffer solution, the Pt-SWCNT probe shows strong Raman shifts of the nanotube G-band as a function of pH, which is ascribed to charge transfer doping of the SWCNT reference electrode. Referenced potential measurements are demonstrated using a nanoscale version of the Pt-SWCNT electrode, along with the accurate monitoring of pH in solutions of different ionic strengths. Controlled experiments at a constant ionic strength show pH measurement across the full range between 1 to 12 with a best accuracy of ±500 mpH unit. This study also explores the influence of different transition metals (Pt, Ru and Pd), of semiconducting *vs.* metallic SWCNTs, and supporting substrates on pH sensing. A model based on electron transfer between the redox metal system and the SWCNT is proposed and tested using electrical conductance measurements.

Due to the outstanding properties of graphene, such as a semi metallic behavior and its relatively inert surface, graphene was selected as a second nanomaterial to further investigate the Raman-pH sensing. From the study with SWCNTs, which determines optimal response with the Pt/PtO redox couple, we explore the Raman response of graphene coated with a thin layer of Pt in different buffer solutions of pH between 1 and 12. The spectra show clear evidence of charge transfer and doping of graphene in contact with the platinum redox couple. Significant Raman shift with pH is noted in the region of the G-band and also in D-band, which are consistent with the behavior found

with the metallic Pt-SWCNT system. An analysis of the Raman shift provides a better understanding of the doping behavior observed for different pH. The analysis provides an estimate of the potential and confirms the Nernstian behavior of the pH sensor.

Redox pH sensing at the nanoscale using carbon nanomaterials solves the main limitations highlighted above, namely coverage of the full pH range and a clear miniaturization of the sensor down to the nanometer scale. Although the accuracy requires further improvement, this work demonstrates for the first time an optical pH sensing scheme that is analogous to a conventional pH sensor equipped with a built-in internal reference.

Keywords: pH sensor, Single-Walled Carbon Nanotubes, graphene, Pt redox couple, Raman spectroscopy.

Table of Contents

List of Figures

List of Tables

Abbreviations

CNTs	Carbon Nanotubes
SWCNTs	Single-Walled Carbon Nanotubes
Referenced electrode	RE
FET	Field Effect Transistor
ISFET	Ion Sensitive Field-Effect Transistors
MOSFET	Metal-Oxide-Semiconductor Field-Effect Transistor
P3HT	Poly(3-HexylThiophene)
AgCl	Silver Chloride
MMO	Metal-Metal Oxide
GO	Graphene Oxide
GQDs	Graphene Quantum Dots
SERS	Surface-Enhanced Raman Scattering Processes
TERS	Tip-Enhanced Raman Spectroscopy
PANI	Polyaniline
DNA	Deoxyribonucleic Acid
p-ATP	p-Aminothiophenol
TEM	Transmission Electron Microscopy
AFM	Atomic Force Microscopy
0D	zero-Dimensional
1D	one-Dimensional
2D	two-Dimensional
DOS	Density of States
VHS	Van Hove Singularity
A Mode	Acoustic Mode
O Mode	Optical Mode
L	Longitudinal

RBM	Radial Breathing Mode
SHE	Standard Hydrogen Electrode
El-Ph	Electron–Phonon
CVD	Chemical Vapor Deposition
PMMA	Poly Methyl Methacrylate Solution
RIE	Reactive Ion Etching
SC	Sodium Cholate Polymer
SDS	Sodium Dodecyl Sulfate
PTFE	Polytetrafluoroethylene
e-beam	Electron Beam
IPA	Isopropanol
APTES	(3-Aminopropyl)Triethoxysilane
ORR	Oxygen Reduction Reaction
Pt/PtO	Platinum/Platinum Oxide
G_f	G_{fanon}
O_2/H_2O	Oxygen/Water
Pt-SWCNTs	Platinum Coated Single-Walled Carbon Nanotubes
Pt_N-SWCNTs	Single-Walled Carbon Nanotubes Decorated with Nanoparticles of Platinum
M-SWCNTs	Metallic SWCNTs
Pt_N-M-SWCNTs	Single-Walled Carbon Nanotubes Decorated with Nanoparticles of Platinum
Pd_N-M-SWCNTs	Single-Walled Carbon Nanotubes Decorated with Nanoparticles of Palladium
Ru_N-MSWCNTs	Single-Walled Carbon Nanotubes Decorated with Nanoparticles of Ruthenium
Pd/PdO	Palladium/Palladium Oxide
Ru/RuO_x	Ruthenium/ Ruthenium Oxide
DDQ	2,3-Dichloro-5,6-Dicyano-p-Benzoquinone

Acknowledgements

This research wouldn't have been possible without the guidance of my supervisor, Prof. R. Martel. I would like to express my deepest gratitude to him for welcoming me to his group and for his patient discussions about my project, encouragement and advice, which he has provided throughout my time as his student. I will never forget it. It also gives me great pleasure in acknowledging the support, help and kindness of Prof. Antonella Badia.

I'd like to take this opportunity to thank those around me who made this possible. I want to thank my friends and colleagues, Suraj Mal, Monique Tie and Leonard Schue for their time and professional help to solve the problems during my PhD's program and Charlotte Allard, Amira Bencherif and Carl Charpin for their kind personality, endless understanding, professional help and for giving me their time in listening to me and helping me work out my problems.
I also wish to thank Etienne Gaufrès and Nathalie Tang for teaching me important skills that will help me academically and personally and for their valuable advice.

I would like to gratefully acknowledge the help of Joel Bouchard for technical support and Christophe Clement, Samir Elouatik, and Marie-Helene Bernier for providing their expertise in characterizing my samples.

Finally, I express my heartfelt gratitude to my beloved family for loving considerations and great confidence in me all through these years, and my great thanks to my parents and siblings for their encouragement, constant support, trust, and love.

Special thanks to my twin flame Reza, without whose endless moral support, this task could have never been completed.

“Dedicated to the memory of my Father who always believed in my ability to be successful in the academic area. You are gone but your belief in me has made this journey possible.”

Chapter 1: Introduction

1-1 Definition of pH

In the 17th century, when the clarification of chemical concepts began, Robert Boyle (1627-91) gave the first distinction between acids and bases (he called bases alkalies). He found that acidic solutions could redden some kinds of vegetable juice (like cabbage juice), whereas basic ones would change the color to blue. He was the first scientist to employ such juices to distinguish between an acidic and a basic reaction and his work was a precursor for the use of indicators to label acidic and basic solutions[1]. However, he did not have a reasonable definition of acids and bases.

In the late 1800s, Svante Arrhenius proposed that water could dissolve many compounds by separating them into their individual ions. Arrhenius found out that acids are compounds which contain hydrogen and can dissolve in water to release hydrogen ions (H^+), and that bases are substances that can also dissolve in water to release hydroxide ions (OH^-) in solution. The hydrogen ion in aqueous solution is too reactive to remain isolated as a bare nucleus. Because of its extraordinarily high charge density, the proton strongly bounds to any part of a nearby atom or molecule which has an excess of negative charge. In the case of water as the solvent, the hydrogen ion immediately bonds to the water molecule through the lone pair electrons of the oxygen atom and forms a hydronium ion (H_3O^+), which has a pyramidal shape. In the presence of a proton, H_2O is in a sense acting as a base here and produces a hydronium ion[2].

In 1909, Sorensen made use of two existing techniques, namely the hydrogen electrode and the saturated calomel reference electrode (RE)[3]. The RE maintains a constant potential, while the hydrogen electrode builds up a potential proportional to the hydrogen ion (H^+) concentration of the solution. The potential difference between this two-electrode system depends on the hydrogen ion (H^+) concentration of the solution. He defined pH as the negative logarithm base 10 of the H^+ concentration. The first definition of pH by Sorenson in 1909 was based on his calculations of the electromotive force which could be used in conjunction with the Gibbs energy (equation (1-1)):

$$\triangle G = \triangle G^0 + RT\ ln\ Q \qquad (1\text{-}1)$$

where ΔG and ΔG^0 are the Gibbs energy change and the same under standard state. R, T, and Q are the gas constant, absolute temperature, and the reaction quotient, respectively.

In 1932, two main general definitions of pH were discussed in the scientific community[4]. The first definition considered pH as a negative logarithm base 10 of the concentration of H^+, as Sorensen described it previously, and the second one was a function of the activity of H^+. In that case, ion activity was used in the definition to account for the interaction of ions within a solution, which can cause some ions to deviate from ideal behavior and effectively appear inactive. In 1948, pH measurements were practiced under equation (1-2) (where pH is a function of the H^+ activity):

$$pH(X) - pH(S) = \frac{[E(X) - E(S)]}{\left(\frac{RT}{F\,ln10}\right)} \qquad (1\text{-}2)$$

where $pH(X)$ and $pH(S)$ are the pH of an unknown solution (X) and a reference solution (S), $E(X)$ and $E(S)$ are the potentials of the cell containing the standard solution and the unknown sample and the quantities R, T, and F represent the gas constant, temperature and the Faraday constant, respectively. According to equation (1-2), there is a link between the measured potential difference ($E(X) - E(S)$) and the pH difference between the unknown solution and the reference solution, $pH(X) - pH(S)$.

Nowadays, the second definition of pH (pH as a function of H^+ activity) is the most accepted because of the dependency of the electrode potential to the ion activity. Furthermore, the pH dependency on temperature is another reason that H^+ activity presents a better mode of measurement, since H^+ activity varies in a directly proportional manner with temperature[4]. Though the history of the definition of pH has seen many changes and modifications, today's measurements are based on this latest definition.

1-2 Importance of pH Measurement

The measurement and control of the pH is important and fundamental in many applications such as food processing, pharmaceutical manufacturing, biomedical system, industrial processing and environmental and clinical monitoring, to name a few. In environmental science, the quality of

water has become a global issue of concern in many aspects, including the quality of human life, industrial processes, agricultural activities, and climate changes[5]. The pH of the water has for example been identified as one of the most important parameters affecting the quality of the water. In fact, chemical, biological, and physical factors can affect the pH of water[6,7]. For example, the pH of rainwater is controlled by the dissociation of dissolved CO_2 and is naturally acidic (around a pH of 5.6). Due to the excessive release of CO_2 and some pollutants, rain is becoming excessively acidic[8] due to the dissolution of additional CO_2 in water to form carbonic acid:

$$CO_2 + H_2O \rightleftharpoons H_2CO_3 \qquad (1\text{-}3)$$

The acidity of rainwater in some places has increased and reaches harmful levels (pH between 4.0 and 5.0)[9]. The acidic rainwater removes minerals and nutrients from soils, which are essential for plants to grow. Therefore, various environmental organizations are trying to reduce the pollutants that cause acid rain, and the pH measurement is a good indicator for environmental monitoring[10].

In the food industry, the pH value of food products is an important factor that affects food characteristics, such as color, texture and taste[11]. For example, the pH value of most food products varies between 3.5 and 7.0 and variation of pH could have an effect on pigments, which are responsible for the color of fruits, vegetables and meat[12-14]. The texture of food products plays an important role in the quality of the food and could influence consumer satisfaction. Texture in vegetables is often related to cell wall structure and composition, and the pH value during the food processing and preservation processes affects the firmness and softness of vegetables. For example, Doesburg[15] showed that plant tissues have the highest firmness at pH values between 4.0–4.5 which decreased at both higher and lower pH. The pH value also has a great impact on water-holding capacity and tenderness of meat and fish that are improved at acidic conditions below the typical pH of *post-mortem*[16, 17]. Thus, measuring and controlling the pH has a significant impact in the production of safe, high-quality products.

Furthermore, many physiological processes show a strong dependency on pH and could be monitored through the changes of this value. For example, in wound healing, which is a complex regeneration process, the pH value within the wound environment affects indirectly and directly all biochemical reactions involved in the healing process. For several decades, physicians thought that low pH favored wound healing but new investigations have shown that some healing processes require an alkaline pH[18, 19]. Research also shows that humans who have problems regulating their

pH are more at risk of infection. Decreasing the pH on the surfaces of implanted medical devices has been related to bacterial colonization of the implant[20, 21]. There has also been an established link in the literature between cancer cells and pH, in which cancer cells show lower pH compared to the normal cell. Cancer cells are known to acidify their environment and, consequently, the interior of the cells is alkalized. The deregulated pH of cancer cells promotes cellular processes that are sensitive to small changes in pH, including cell proliferation, migration and metabolism. This, in turn, affects the activity of proteins, which are regulated within a narrow cellular range of pH[22, 23].

1-3 pH Measurement Techniques

There are two main approaches involved in pH measurements, the potentiometric approach and the optical approach. The first one includes the popular and commonly used potentiometric glass electrode, Ion Sensitive Field-Effect Transistors, Metal-Metal Oxide pH Sensors and Metal Oxide-Metal Oxide pH Sensors. The second one includes titrations and pH sensing based on optical measurements such as UV-VIS absorption spectroscopy and photoluminescence (PL). All these techniques are described below.

1-3-1 Potentiometric Methods

The most popular and common techniques of potentiometry are described here.

1-3-1-1 Glass pH Electrodes

The well-known glass pH sensor measures the pH value based on the potential difference between a glass electrode and a reference electrode. The glass pH electrode consists of a thin membrane made of a specific type of glass that is selectively permeable to hydrogen ions and gives a potential difference that is proportional to the concentration of ions. This electrode is placed at the end of a glass tube (Figure 1.1). The internal solution consists of a buffer solution (usually 0.1 mol/L sodium chloride), in which a silver (Ag) wire covered by a silver chloride (AgCl) coat is immersed. This wire forms the electrical connection. The pH value of the internal solution is usually 7. The reference electrode is located in the outer glass tube and it also contains Ag/AgCl in buffer solution. The potential difference between the measuring system and the reference system is determined and this difference is created by penetrating hydrogen ions of the measuring solution into a small portion of the hydrated layer of the outer boundary area of the glass membrane and by

the hydrogen ions of the inner buffer solution of pH= 7 to the hydrated layer of inner boundary area of the bulb.

If the hydrogen ion activity (which is related to the pH) differs from the activity of the outer part, a measurable potential difference is created. Thus, if the inner activity of hydrogen ions is lower (or higher) than that of the outer, the pH of the solution is acidic, i.e. pH< 7 (higher, i.e. pH > 7). In the case of equal activity of the inner and outer parts, the pH value is neutral (pH=7). The potential of the system, which is related to pH, can be calculated using the Nernst equation:

$$E = constant + 2.303\frac{RT}{nF} log\ \alpha_H^S \qquad (1\text{-}4)$$

where R is the universal gas constant, T is temperature, n is the charge of the species, F is the Faraday constant and α_H^S is the activity of the hydrogen ion in the solution. The constant term is the sum of the potential differences of the other interfaces evaluated relative to the reference electrode (i.e, a standard cell potential)[24, 25].

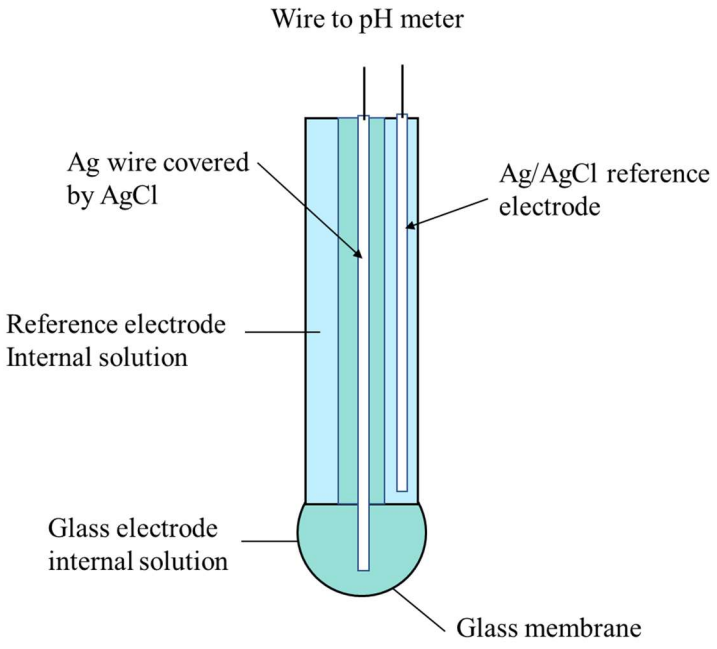

Figure 1.1. Schematic of a standard glass pH electrode

The glass electrode can measure potentials in the range of a few hundred millivolts. The glass electrode presents several advantages such as its stability, non-expensiveness and short response

time. The glass pH electrode also is usable over a wide working range and possesses high accuracy. However, there are some difficulties and disadvantages to the use of the pH glass electrode, which include a acid and basic errors, difficulty in miniaturization, leakage of the reference electrode buffer into the sample solution, fragility and storage problems (needs to be correctly stored and can't be dry)[26].

1-3-1-2 Ion Sensitive Field-Effect Transistors (ISFET)

Ion-selective field effect transistors (ISFETs) are another common technique to measure the pH, which were developed more than 40 years ago[27]. These transistors belong to the wider category of field effect transistors (FETs) and are used for measuring ion concentrations in solution. The structure of the ISFET is similar to that of a MOSFET (metal-oxide-semiconductor field-effect transistor), but the metal gate is replaced by a sample solution with a reference electrode immersed in the solution and an ion-sensitive membrane for detecting a specific analyte (figure 1.2). This membrane is sensitive to positive proton and causes the approach of negative charge to the other side of the membrane. Therefore, a current flow between source and drain. The existence of proton close to the membrane creates, depending on concentration, more or less negative charges on the other side of membrane, forming a gating effect that increases or decreases the FET current[28, 29].

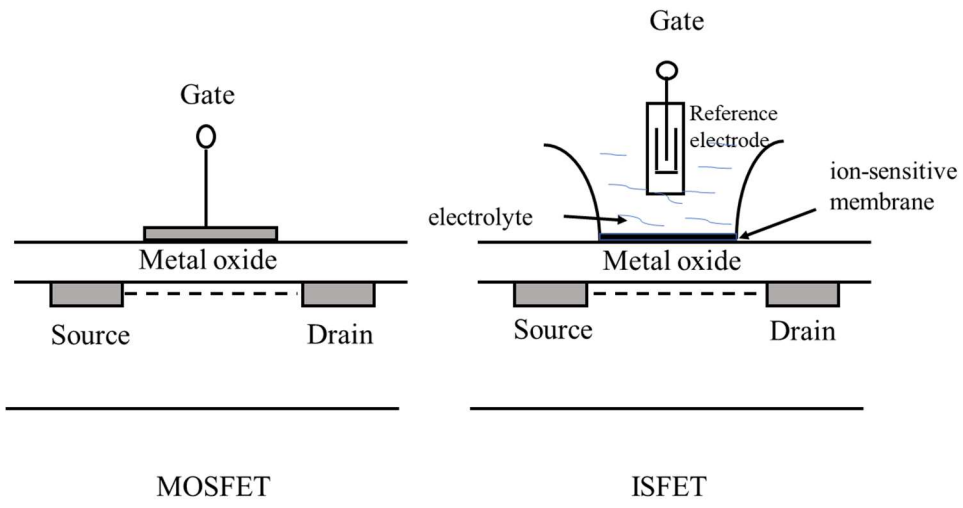

Figure 1.2. Structure of metal–oxide–semiconductor field-effect transistor (MOSFET) (left) and ion sensitive field-effect transistor (ISFET) (right).

Using ISFETs as a pH sensor could solve some of the problems of the glass pH electrode such as the size of the ISFET pH sensor, which is smaller than a glass bulb pH sensor, unbreakable and

can be stored dry. ISFET pH sensors are otherwise limited by the size of the reference electrode, and the fact that they are more expensive and less accurate and sensitive than pH glass electrodes[30]. Nowadays, there is a lot of research focusing on reducing the price of the transistor setup and on miniaturizing the reference electrode toward micrometer sizes[31-33].

To have a cost effective, flexible and disposable pH sensor, M. Münzer *et al.* compared two different semiconducting materials as a channel: carbon nanotubes (CNT) networks and poly(3-hexylthiophene), which is mainly known for its application in organic solar cells. Both devices show sensitivity to the pH in buffer in a way that the electrical current increases with higher pH values, but carbon nanotube transistors show faster response and this agrees with their higher hole mobility compared with polymeric semiconductors. They also showed that the carbon nanotubes transistors were more stable compared to the P3HT transistors[34].

Back and Shim showed that single-walled carbon nanotubes (SWCNT) transistors exhibit significant pH-dependent electron-transport properties. They observed a negative shift of the threshold Voltage with decreasing pH, which is ascribed to a p-doping of the SWCNTs. They also showed that the increase of the electrolyte concentration leads to a screening of the pH-induced changes[35].

Tang *et al.* demonstrated that SWCNTs and graphene decorated with nanoparticles of platinum and placed as a channel in a FET induce a negative shift of the threshold Voltage in acidic solutions and a decrease in current compared to uncoated SWCNTs, which is ascribed to a p-doping. This research highlighted for the first time a doping mechanism of platinum decorated SWCNTs at different pH values[36].

Many efforts have been invested to minimize the size of the reference electrodes such as using a uniquely microfabricated parylene tube structures filled with chloride rich electrolyte and a 50 μm diameter silver (Ag) wires covered with a 7.4 μm thick silver chloride (AgCl) layer, which is inserted inside the parylene tube[37]. Screen-printed silver/silver chloride (Ag/AgCl) reference electrode have also been developed[38].

Kakiuchi *et al.* showed that the ion-gel reference electrode could improve the accuracy of ISFETs by at least one order of magnitude[39]. To increase the sensitivity, a passivation layer is used as a hydrogen ion sensitive membrane but a reference electrode is still needed. Szkopek *et al.* recently

presented a new ISFET pH sensor made of encapsulated graphene deposited on an ultrathin layer of parylene, which is hydrophobic, and coated with an ultrathin pH-sensing layer made of either aluminum oxide or tantalum pentoxide. This ISFET configuration helped reduce the detection limit to 0.1 mpH[40].

1-3-1-3 Metal-Metal Oxide pH Sensors

As mentioned earlier, the glass pH electrode is the most commonly used method to measure pH because of its stability, response time, lifetime and accuracy but it also comes with some limitations, such as the cumbersome size of the electrode and the difficulty in obtaining a proper response to pH in some corrosive environments (e.g., in hydrogen fluoride solutions). These drawbacks justify the introduction of new techniques. A recent method used to overcome some of the above constraints is the use of a metal-metal oxide (MMO) for pH sensing. Metals such as Sb, Sn, Fe, Ir, Ag, Cu or Zn, which are covered by an oxide coating, are used in this technique, which is based on the reduction-oxidation (redox) reaction on the surface of the metal. A reference electrode is also used in this technique[41].

The most well-known example of this MMO technique is the antimony electrode, which can be used in harsh conditions where the glass pH electrode is not stable, such as in HF[42]. The potential of an antimony-based MMO electrode can be determined by the equilibrium relation and the Nernst equation[41, 43]:

$$Sb_2O_3 + 6H^+ + 6e^- \leftrightarrows 2Sb + 3H_2O \qquad (1\text{-}5)$$

$$E = E_0 + \frac{0.059}{6} \log \frac{1}{[H^+]^6} = 0.152 - 0.0583\, pH \qquad (1\text{-}6)$$

where E and E_0 are respectively the electrode potential and standard potential and $[H^+]$ is the proton concentration. $Sb - Sb_2O_3$ electrodes do not reach the expected Nernstian behavior, which reduces the slope compared to theoretical slope and decreases the sensitivity of these electrodes in alkaline conditions (equation 1-6). Also, these electrodes are not suitable for long term applications due to the drift of potential response[44].

However, researchers are still trying to improve the stability of the electrode, for example, by modifying the antimony with cation-conducting polymers like Nafion[45]. To further improve the

sensitivity of MMO pH sensors, researchers found that the stacking two different metal oxides could provide a good pH response. This kind of sensor is called the Metal oxide-Metal oxide pH sensor.

1-3-1-4 Metal Oxide-Metal Oxide pH Sensors

Researches have shown that the oxides of Pt, Pd, Rh, Ru and Ir can be used as a pH sensor[46, 47]. Kreider *et al.*[47] and Fog *et al.*[46] showed that Ir and Ru oxides are the most promising for pH sensing. For the Ir oxide, the redox reaction involved after the hydration of the IrOx is:

$$2\,IrO_2 + 2\,H^+ + 2\,e^- \rightleftarrows Ir_2O_3 + H_2O \qquad (1\text{-}7)$$

It is obvious from equation 1-7 that for every two protons, two electrons are required. Therefore, the current and the cell Voltage measured by the electrode are related to the pH value of the solution. This kind of metal oxide electrode shows good sensitivity with a Nernstian response of 59 mV/pH[48].

Later electrochemical techniques could solve many of the problems facing the glass electrode, but the need of a reference electrode makes the miniaturization of the pH sensor extremely complicated.

1-3-2 Optical pH Sensing

As said before, the potentiometric method, especially the glass pH electrode, is widely used to measure the pH value. A glass pH electrode is reliable and easy to operate, and has the advantages of being relatively low cost, offering rapid measurements over a wide range of pH. However, glass pH electrodes are generally big, limited by rigid design, suffer from leakages of electrolytes and are fragile against aggressive analytes such as alkaline solutions or fluoride ions. Other potentiometric methods tried to overcome these limitations, but they still need a reference electrode, which makes a miniaturization of the sensing device more difficult.

Optical pH sensors don't need reference electrodes and can be miniaturized. They also do not require a separate reference sensor, do not suffer from electrical interferences and could provide both invasive and remote pH measurements. Optical pH sensors have therefore attracted the interest of researchers for overcoming the limitations of potentiometric methods. Other advantages

associated with optical pH sensors include low energy consumption, capability of continuous measurements and ease of handling [49].

Optical sensors consist of reagents associated with a change in their optical properties on interaction with the analyte of interest. The most common optical properties for that purpose are absorption, fluorescence intensity, light scattering, reflectance, refractive index, and light polarization [50]. Optical pH sensors have been developed for over 40 years, [51, 52] but only few have been commercialized[53]. In optical pH sensing, changes in pH value are detected using pH indicators, which are typically weak organic acids or bases having specific optical properties (e.g., color) related to their protonated (acidic) and deprotonated (basic) forms. For example, the absorption or fluorescence properties of dyes change with a change in proton concentration (or pH)[54]. The important challenges for optical pH sensors are the need of a robust pH indicator that does not photobleach as well as the formulation of an inert matrix material in which the dye can be immobilized while also allowing fast diffusion of protons[52, 55-58].

The highest sensitivity of pH indicators is observed at pH close to the pK_a at which their optical properties (such as absorption, fluorescence, light scattering or reflectance) change as a function of the pH of the environment. The dynamic range of optical pH sensors is usually limited to acid dissociation constants ($pK_a \pm 1.5$). Therefore, pH indicators with two pK_a values or groups of similar dyes with different pK_a values to cover the full range of pH (from 0 to 14) have been used[59, 60]. Recently, Tormo et al. discussed using ruthenium metal−ligand complexes as luminescent pH indicators[61].

Nowadays, nanomaterials such as silica and polymer nanoparticles are used to encapsulate the indicators for pH sensing in cells for example. Burns *et al.* fabricated optical pH-sensitive silica nanoparticles (NPs), which were used to detect pH in rat basophilic leukemia mast cells[62].

Much effort has been invested in finding proper indicators and stable solid matrices, but further improvements of the optical sensing technologies are still needed in order to increase the performance of these devices, such as increasing the working range and the sensitivity.

1-3-2-1 Optical pH Sensing with Carbon Nanomaterials

Carbon-based nanomaterials like graphene, graphene oxide, graphene quantum dot and carbon nanotube have unique mechanical, electrical and optical properties, which make them good candidates for optical pH sensing. Some of recent research related to optical pH sensing with these materials are described here.

Graphene Oxide (GO). The GO is the oxidized form of graphene. It is a single-atomic-layered material which is chemically rich (because of the π electrons). It forms 2-dimensional (2D) flat surfaces that can be used for chemical functionalization with nanoscopic functional groups. Graphene oxide is easy to process since it is dispersible in water and other solvents. The GO can be functionalized with pH indicators, which are optically active, such as thiophene dyes[64]. Graphene oxide acts as the solid matrix allowing high functionalization loading of pH reporting dyes and good control of the spacer length between the GO and dye. The GO intermediate during functionalization can be dissolved in several organic solvents, allowing its combination with indicator dyes that are not soluble in water[63]. Also, the addition of GO has a high impact on nanofibrous-based pH sensors, for example polyurethane/poly2-acrylamido- 2-methylpropanesulfonic acid /graphene oxide with indicator dyes showing quick response to pH variations over a wide range of pH (1–8)[64].

GO can also be used as a matrix for Lanthanide-doped up-conversion nanoparticles (as a replacement of organic dye) for pH sensing based on photoluminescence.[65]

Graphene Quantum Dots (GQDs). GQDs are fluorescent carbon-based nanomaterials similar to GO, regarding structural and physical properties, but they differ in size (less than 10 nm)[66]. The GQDs have several advantages compared to other carbon materials, such as ease of synthesis, alternative green synthetic procedure, ultra-small size, non-toxicity and excellent aqueous solubility[67, 68]. Kumawat *et al.* presented a new one pot microwave assisted synthesis of GQDs, which are used as optical pH sensors between pH=3 and pH=10 with a sensitivity of −50 ± 4mV/pH[69]. GQDs could also be used with polymers to increase the pH range like using poly (acrylic acid) and poly(2-vinylpyridine) quantum dot hybrids integrated on a single sheet graphene oxide[70].

Carbon Nanotubes. Another carbon material that has been investigated is carbon nanotubes (CNTs). They are cylindrical molecules that consist of rolled-up sheets of single-layer carbon atoms (graphene). They can be single-walled (SWCNT) with a diameter of the order of nanometer (nm) or multi-walled (MWCNT), consisting of multiple rolled layers of concentric nanotubes of graphene inside other nanotubes with diameters reaching more than 100 nm.

CNT-base nanocomposites are potential candidates for optical pH sensing[71, 72]. Composites of CNTs made with a wrapped polymer like polyaniline (PANI) have been designed, with pH dependency related to a change in the oxidation state of the PANI in PANI -carbon nanotube nanocomposite reflected by a change in color (optical change). It is also possible to miniaturize optical sensor devices using PANI-CNT nanocomposite- coated optical fibers. This kind of nanocomposite was developed both with MWCNTs[71] and SWCNTs[72] and can cover the whole range of pH.

The pH dependency of photoabsorption and photoluminescence of the SWCNTs wrapped by deoxyribonucleic acid (DNA) was also reported[73]. Similarly, Dai *et al.* reported that non-covalently functionalized SWCNTs with fluorescein-polyethylene glycol could show absorbance and fluorescence pH dependency[74].

p-Aminothiophenol (pATP)-functionalized MWCNTs have been shown to behave as a pH sensor for living cells. Gold/silver core-shell nanoparticles (Au@Ag NPs) on functionalized MWCNTs are reported to have a pH-dependent SERS performance. By using multiwalled carbon nanotubes as the substrate, the pH sensing range could be extended to pH 3-14. This nanocomposite is expected to have applications as an intracellular pH sensor for biomedical applications[75]. The same idea implemented by decorating SWCNTs with bimetallic nanoparticles (silver-coated gold) nanoparticles has formed a SERS-based sensor capable of measuring the pH over the range of 5.6 to 8.2 pH units[76].

Graphene. The pH dependency of the Raman response of graphene was also reported[77-79]. Paulus *et al.* made use of this phenomenon to analyze the metabolic activity of cells. They showed that the graphene Raman biosensor can detect various analytes such as immunoglobulin and dopamine by the dependency of the graphene Raman response to doping [77]. Camerlingo *et al.* also used this phenomenon (i.e. the pH dependency of the Raman response of graphene) to evaluate pH changes in the cells after X-Ray irradiation [78]. For the context of this thesis, we will see in the last chapter

that the response of graphene itself is unlikely here, but nevertheless the study is important because it showed a clear dependency of the Raman response to pH changes and serves as a proof of concept to use the approach of mapping pH.

Zuccaro *et al.* found a new technique to obtain chemical information after noncovalent attachment of a small quantity of functional moieties on graphene and also on carbon nanotubes. By using surface-enhanced Raman scattering processes (SERS), the technique does not affect the Raman signature of the underlying nanostructure and avoids expensive techniques like tip-enhanced Raman spectroscopy (TERS). In this research, they observed a clear signature in the Raman peaks of the pH sensitive polymers (polypyrrole and polyaniline) when deposited on graphene (or carbon nanotubes). They also monitored the Raman peaks of graphene (and carbon nanotube) by depositing nanoparticles of gold on top of the polymers[80]. Overall, much research was done on the Raman-pH dependency of polymers[81, 82], which could open up a new way for pH sensing when the polymers are combined with graphene or carbon nanotubes.

The use of carbon nanomaterials as optical pH sensors has opened the way to the miniaturization of the pH sensor, but the detection range of these kinds of sensors are limited and this is one of the main ongoing problems with optical pH sensors.

1-4 Scope of the Thesis and Objectives

In this thesis, we aim to develop a pH sensor based on carbon nanomaterials, which uses a non-destructive optical technique (Raman spectroscopy). The work targets a better understanding of redox pH sensing with nanomaterials and proposes new schemes for pH sensing that can solve the main limitations highlighted previously, namely a sensitivity to the full pH range and the feasibility of miniaturization of the device.

In order to do this, two types of nanomaterials, graphene and single-walled carbon nanotube, were examined. First, we chose SWCNTs because of the high intensity of their Raman peaks compared to graphene. Based on the knowledge of the Raman spectroscopy of carbon nanotubes as well as electrochemistry, we have explored the use of proper reduction-oxidation (redox) couples allowing charge transfer with the SWCNTs. The shifting fingerprints of the Raman peaks of SWCNTs were

used to monitor charge transfer in acidic and basic solutions. To achieve this goal we deposited a thin layer of platinum on the SWCNTs film.

To develop a practical pH sensor, we investigated the potential errors introduced by the local environment to the pH measurements:

1- the effect of the substrate.

2- the effect of the ionic strength of the buffer.

3- We also measured the resistance of the film of SWCNTs decorated with a chosen redox couple. To improve the Raman response with pH of the hybrids and explore the effect of semiconducting nanotubes, we worked with sorted metallic SWCNTs (metallic SWCNTs) and compared the results with those of unsorted SWCNTs (mixture of metallic and semiconducting SWCNTs). The metallic SWCNTs, which were wrapped with surfactants, were also decorated with nanoparticles of platinum using a one pot reaction and used to investigate the Raman-pH sensitivity of the hybrids. Different metals, which are well known for oxygen reduction reaction (such as platinum, palladium and ruthenium) were tested and Platinum was found to be best adapted for pH sensing.

In the second part of the project, we made use of the interesting optical and chemical properties of graphene and investigated the Raman-pH dependency of graphene coated with a thin layer of platinum. This last study was used to evaluate the charge transfer doping in relation with the expected Nernst behavior.

1-5 Thesis outline

This thesis is organized into 6 chapters, which includes this overview of the thesis as chapter 1.

In chapter 2, the theory needed to understand the thesis is described. This chapter covers the electronic and phononic structures of SWCNTs and graphene, important concepts in Raman spectroscopy of SWCNTs and graphene and the key notions behind charge transfer in these two nanomaterials. The effects of doping on the main Raman features of graphene and carbon nanotubes as well as the theory behind conductivity measurements are also explained.

Chapter 3 is devoted to the preparation of the samples and it is divided in seven sections. The first section is related to the growth of graphene and the transferring methods on substrates with position markers, which serves to accurately locate the Raman measurements in one spot. In the second section, the purification of different sources of carbon nanotubes and the functionalization with different metals (platinum, palladium and ruthenium), as well as methods to deposit them on substrates, are described. The next two sections are about the preparation of the buffer solutions and samples for sheet resistance measurements and the last three sections are devoted to the preparation of the samples for Transmission Electron Microscopy (TEM), Atomic Force Microscopy (AFM) and Raman measurements and to the description of these instruments.

In chapter 4, the dependency of the doping of laser ablation single walled carbon nanotubes to the solution pH is investigated, along with the effect of the substrate, the ionic strength of the buffer solution and other effects such as the Raman response of the semiconducting SWCNTs. In this chapter, the pH sensing of metallic SWCNTs functionalized with nanoparticles of platinum is compared with other nanoparticles (palladium and ruthenium). Finally, the results of pH sensing of unsorted SWCNTs decorated with nanoparticles of platinum and electrical resistance measurements of this sample are presented.

Chapter 5 covers the dependency of the Raman spectra of uncoated graphene and platinum coated graphene in the region of the G- and D- bands on the pH value. In chapter 6, finally, a general conclusion and the scientific contributions of this thesis are summarized.

Chapter 2: Theory and Main Concepts

In this chapter, the structure and the electronic and vibrational properties of graphene and carbon nanotubes are introduced. Basics notions of electrochemistry are also exposed along with the influence of charge transfer doping on the Raman G band of graphene and SWCNTs.

2-1 Structure of Carbon Nanotubes from Graphene

Carbon is the sixth element of the periodic table with six electrons in the 1s, 2s and 2p atomic orbitals. The four valence electrons ($2s^2$ $2p^2$) are involved in the covalent bonding of carbon materials through sp^n (n = 1, 2, 3) hybridized bonds[83, 84]. Diamond and graphite are two natural carbon allotropes, with sp^3 and sp^2 hybridization, respectively, exhibiting very distinct physical properties. They have remained for a long time the only known carbon allotropes until the discovery of fullerenes (C60) in 1985[85] also referred to as zero-dimensional (0D) carbon materials. A few years later, one-dimensional (1D) carbon nanotubes (CNTs)[86] were identified for the first time and a decade later, in 2004, the exceptional electronic properties of two-dimensional (2D) isolated graphene[87] were uncovered. The atomic structures of each member of the low-dimensional carbon materials family are related to one another, despite having unique properties. From a structural point of a view, graphene may be considered as the fundamental building block[88-90]. In particular, single-wall carbon nanotubes are often viewed as a monolayer graphene rolled up along a certain direction from which semi-conducting or metallic properties will emerge.

The crystal structure of graphene consists of a hexagonal network of carbon atoms (Figure 2.1a) sometimes called "honeycomb lattice", with two vectors $\overrightarrow{a_1}, \overrightarrow{a_2}$ forming the unit cell. There are different ways to roll graphene into a tube, which are defined by the chiral vector (or circumferential vector) $\overrightarrow{C_h}$ through the mathematical expression: $\overrightarrow{C_h} = n\overrightarrow{a_1} + m\overrightarrow{a_2} \equiv (n, m)$, where n and m are positive integers [91, 92]. The angle θ that $\overrightarrow{C_h}$ makes with $\overrightarrow{a_1}$, called the chiral angle (Figure 2.2), is used to differentiate three classes of carbon nanotubes: zigzag ($\theta = 0°$), armchair ($\theta = 30°$) and chiral $0° < \theta < 30°$.

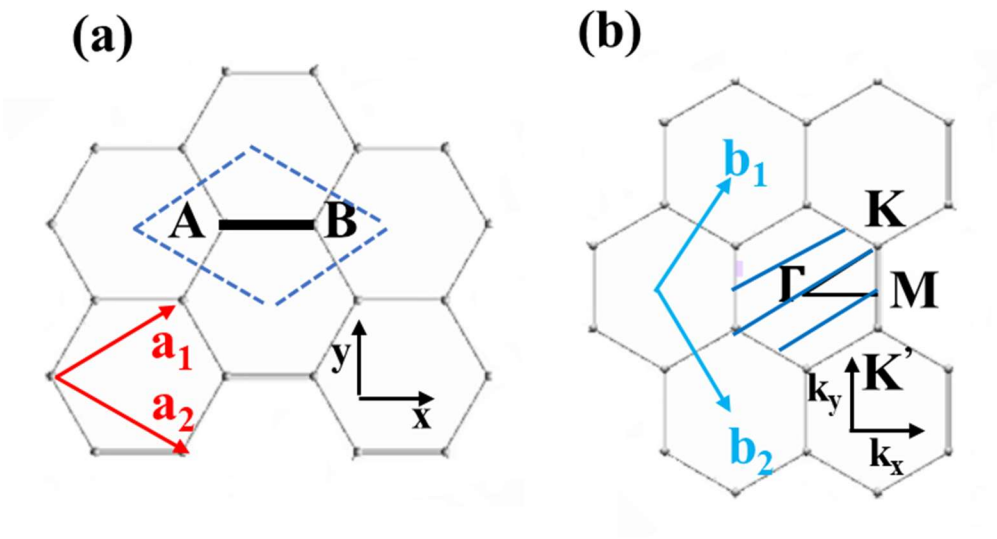

Figure 2.1. (a) The unit cell of graphene (inside the dashed blue line) contains two atoms A and B. (b) The Brillouin zone (hatched region), and high symmetry points M, K, and Γ. The real- and reciprocal-space unit vectors are shown by $\overrightarrow{a_1}, \overrightarrow{a_2}$ and $\overrightarrow{b_1}, \overrightarrow{b_2}$.

The diameter of the SWCNT can be calculated from this equation:

$$d_t = |\overrightarrow{C_h}| = a\sqrt{n^2 + m^2 + nm}\,. \quad (2\text{-}1)$$

The vector $\vec{T}$ In Figure 2.2 is called the translation vector and is the 1D unit vector of the SWCNT. It is oriented parallel to the SWCNT axis, and perpendicular to $\overrightarrow{C_h}$. The translation vector is defined as $\vec{T} = t_1\overrightarrow{a_1} + t_2\overrightarrow{a_2} \equiv (t_1, t_2)$. Defining the unit cell of carbon nanotube is more complex than graphene and could be shown with the rectangle OAB'B in Figure 2.2, in which the vectors $\overrightarrow{C_h}$ and $\vec{T}$ contain the unit cell of the SWNT.

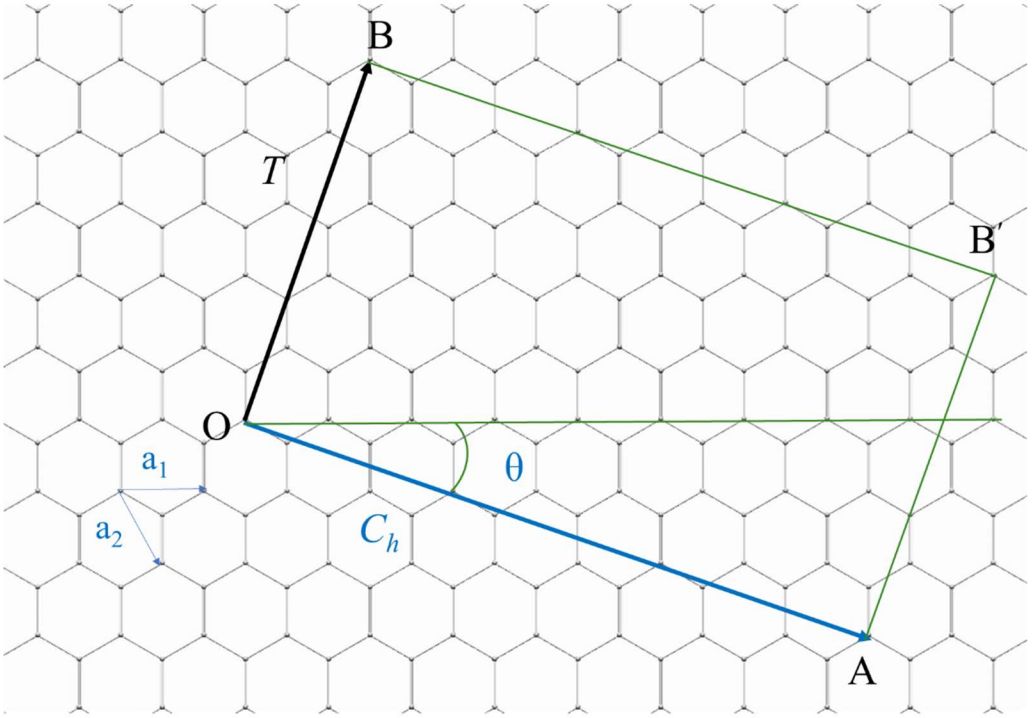

Figure 2.2. The unrolled honeycomb lattice of a nanotube. The chiral vector $\overrightarrow{C_h}$ and translation vector $\vec{T}$ chiral angle θ for a (6,3) SWCNT.

As said before, reciprocal space of graphene is described by the vectors $b_1^{\rightarrow}, b_2^{\rightarrow}$. In the same way, the reciprocal space of carbon nanotube can be described by two vectors, $\overrightarrow{K_1}$ and $\overrightarrow{K_2}$, which are the reciprocal space vectors. The $K_1^{\rightarrow}$ and $K_2^{\rightarrow}$vectors define the separation between the adjacent cutting lines and the length of cutting lines, respectively. The first Brillouin zone of the carbon nanotube is expressed as a section of $K_2^{\rightarrow}$ which is known as a cutting line[92, 93].

2-1-1 Electronic Structure

Much of the electronic structure of SWCNTs can be derived from that of 2D graphene (Figure 2.3). The extrema of the valence and conduction bands of graphene are located at the six corners (K points) of the Brillouin zone (Figure 2.3a). The zone center is called the Γ and M is the midpoint of high symmetry between adjacent K points, also known as the Dirac points (Figure 2.3(b))[94]. Around these points, the dispersion relations for the electronic bands are linear and form the so-called Dirac cones.

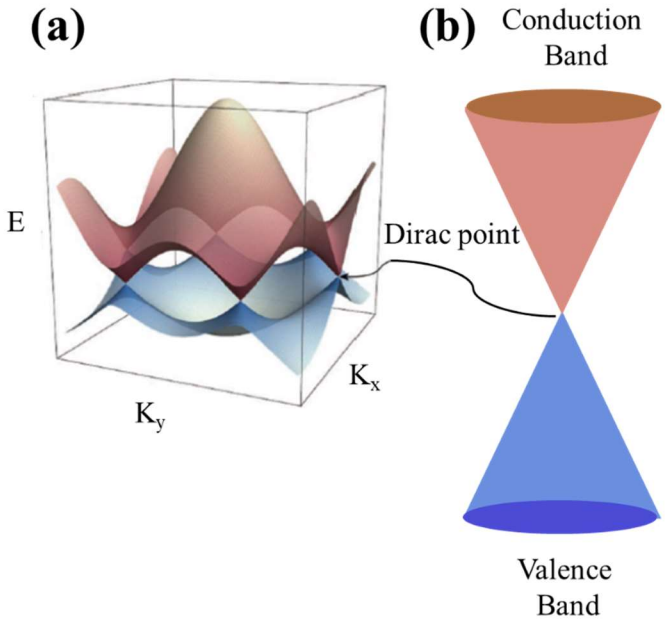

Figure 2.3. Electronic band structure. a) Band structure of graphene. b) Zoom on the linear dispersion region of electronic structure near the Fermi level, showing the vertically mirrored Dirac cones intersecting at the Fermi level. Adapted from reference [95][95]. Copyright © 2012 WILEY-VCH Verlag GmbH & Co. KGaA, Weinheim

The electronic band structure of SWNTs is strongly influenced by their cylindrical structure, which imposes new periodic boundary conditions on the electronic wavefunction [96]. Therefore, the electronic band structure of carbon nanotube consists of 1D sub-bands represented by cutting lines (not shown here) in the reciprocal space of 2D graphene.

If a cutting line passes through the K point, the nanotubes are metallic, otherwise it is semiconducting. More generally, the nanotubes that satisfy the conditions $MOD(2n + m\,, 3) = 0$ are metallic nanotubes (M-SWCNTs) and those for which $MOD(2n + m\,, 3\,) = 1\ or\ 2$ are semiconducting (usually referred to as $MOD1$ and $MOD2$ respectively)[84, 97, 98].

2-1-2 Density of States (DOS)

The electronic density of states (DOS) refers to the number of allowed electronic states at a given energy level. The density of states in a 1D system presents strong singularities, also known as the van Hove singularities (VHSs) shown in Figure 2.4. The DOS of semiconducting nanotubes (Figure 2.4b) contains a series of VHSs corresponding to the band edges of each hyperbolic band, while for metallic nanotubes, there is a constant DOS at low energies, followed by VHS for non-linear bands at higher energies (Figure 2.4a) [96, 99].

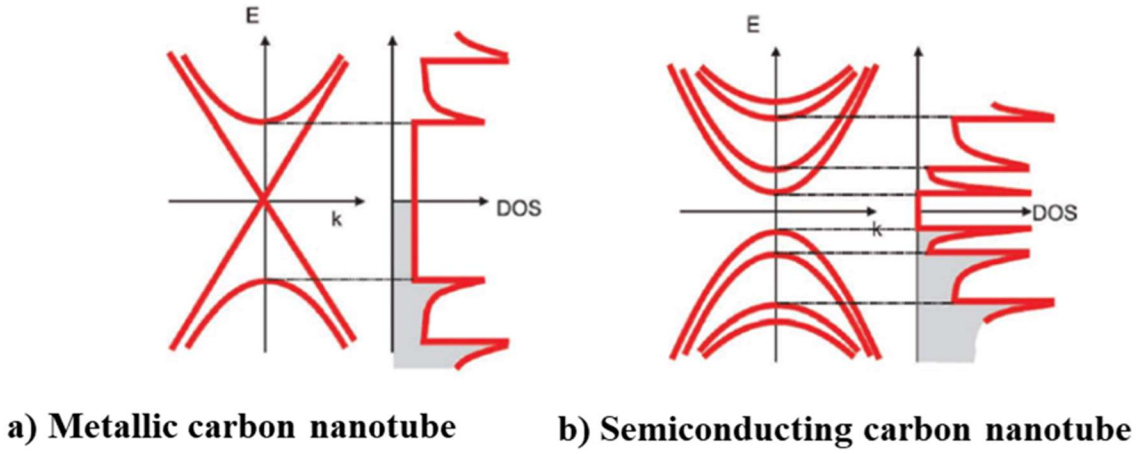

Figure 2.4. The electronic structure (left) and corresponding density of states (right) for a metallic nanotube (a) and a semiconducting nanotube (b). Adapted from reference [100][100]. Copyright © 2012 WILEY-VCH Verlag GmbH & Co. KGaA, Weinheim

2-1-3 Optical Transitions

The optical properties of SWNTs are governed by the electronic transitions between the joint DOS related to the VHSs of the valence and conduction bands. An optical transition from the i^{th} valence band to the j^{th} conduction band, of energy Eij, is optically allowed only if $i = j$[92]. The energies of the Eii for a specific (n, m) nanotube is widely used in absorption and in resonance Raman spectroscopies due to a matching between the incident or scattered light frequencies and the

electronic transitions of the VHSs of a selected nanotube [101-103]. The main optical transitions are labeled Sii and Mii for semiconductor and metallic nanotubes, respectively. The Kataura plots in Figure 2.5 presents the evolution of the Eii transition energies as function of the nanotube diameter, which values are systematically being used to characterize the optical properties of a given carbon nanotube [104, 105].

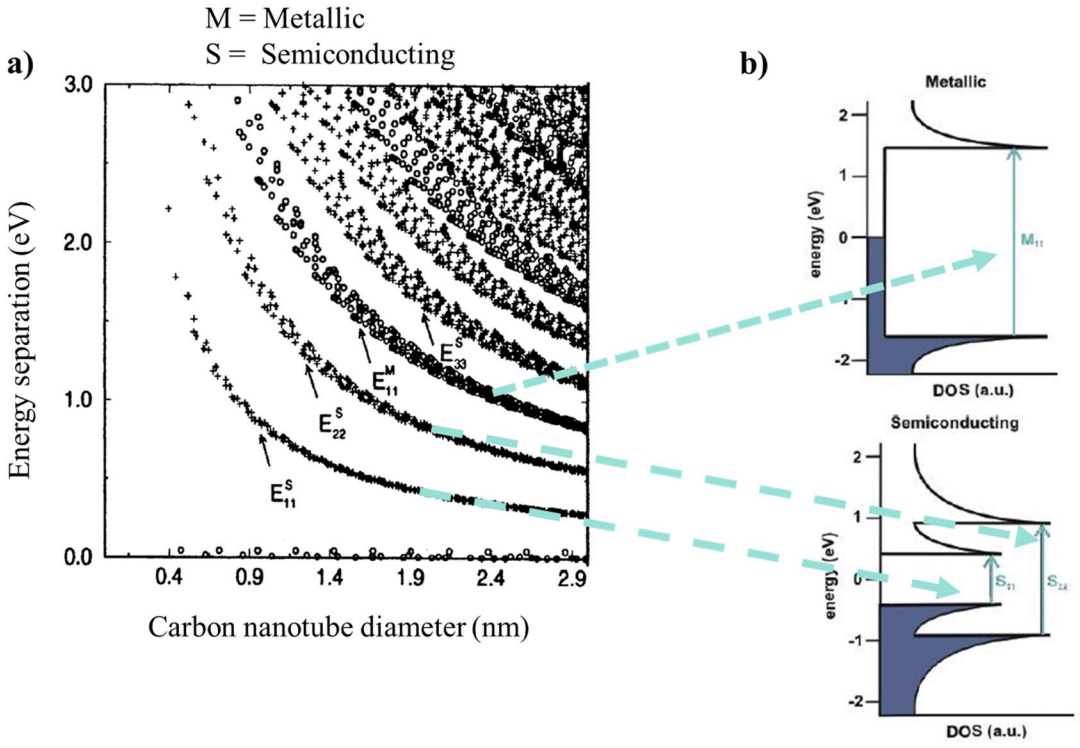

Figure 2.5. The Kataura plot displaying the calculated energy separations between van Hove singularities with nanotube diameters below 3.0 nm (a). Schematic of the density of states of semiconducting and metallic carbon nanotubes. Arrows indicate the allowed transitions for light absorption. Adapted from reference [106][106] with permission from the Royal Society of Chemistry.

2-1-4 Phonon Structure of Graphene and Carbon Nanotubes

The phonon dispersion relation of a carbon nanotube can be obtained from those of the 2D graphene sheet using the same approach as was used here before to find the electronic structure [96]. With two atoms in the unit cell, 2D graphene presents, based on symmetry arguments, six phonon modes. Three of them originate from the Γ point of the Brillouin zone and correspond to the acoustic (A) modes. The three remaining are optical (O) modes, one non-degenerate out-of-plane mode and two in-plane modes that remain degenerate as we move away from the Γ point. Depending on the vibrational amplitude parallel or perpendicular to the basal plane, there are longitudinal (L) and transverse (T) modes respectively (Figure 2.6) [93].

For carbon nanotubes, the phonon dispersion relations further depend on the indices (n,m) or equivalently in the diameter and chiral angle of the nanotube, an example of the phonon dispersion for a (10,10) SWNT is presented in Figure 2.6c. By superimposing the N "cutting lines" on the six phonon frequency plot in the reciprocal space of graphene, sharp spikes appear on the phonon density of states of carbon nanotube (Figure 2.6d), which is similar to what is observed for the electronic DOS. Owing to symmetry selection rules, there is no allowed infrared mode for the graphene itself and only a few of the modes are Raman and infrared active for the nanotubes [107, 108].

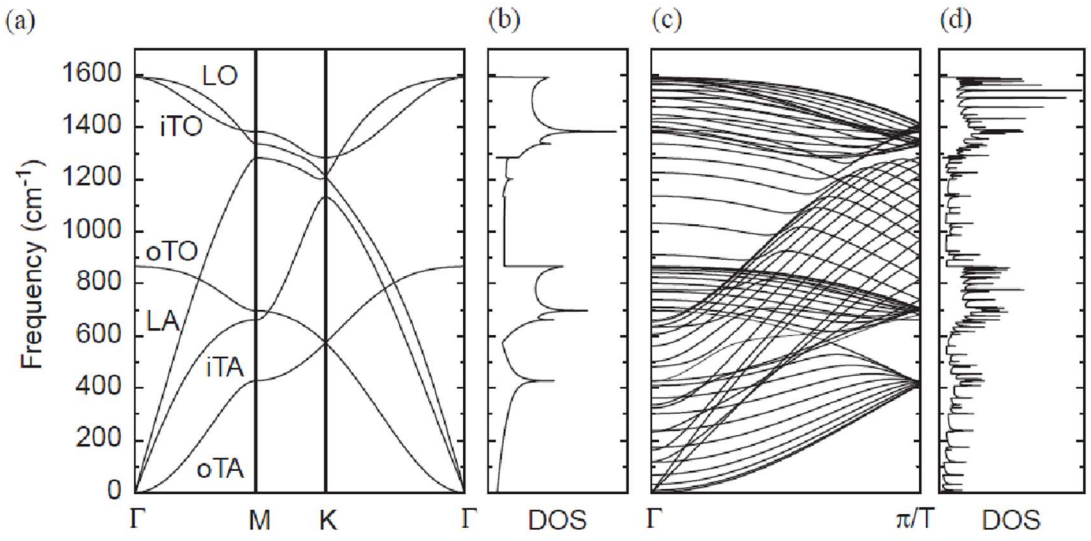

Figure 2.6. a) and c) are phonon dispersion of graphene and armchair carbon nanotube (10, 10) (SWCNTs) (respectively) and b) and d) are phonon density of state of graphene and carbon nanotube (10, 10), respectively. Adapted from reference [109][109].

2-2 Raman Spectroscopy

When a material (a molecule or a solid) is irradiated by a light source, a major part of it is transmitted, absorbed or reflected and only a small fraction is scattered. If the incident and scattered photons have the same energy, the scattering process is elastic, and this is called the Rayleigh scattering[93]. When incident and scattered photons have different energies, the process is inelastic and called Raman scattering. The incident photon of a Raman process can create (Stokes process) or absorb (anti-Stokes process) a phonon in the crystal [110-112]. Compared to the Rayleigh scattering, the Raman scattering event is much less probable and gives much weaker signals.

A Raman spectrum typically displays the scattered intensity, I_s , which is the total number of scattered photons as a function of $E_{laser} - E_{scattered\ pho}$ (called Raman shift commonly expressed in cm^{-1}). The scattered intensity shows peaks corresponding to the phonons involved in the Raman scattering process. The first-order Raman scattering process is the most common case in which an electron from the valence band is excited to the conduction band by absorbing a photon. The photon can generate an excitonic transition, which corresponds to an electron-hole

bounded state due to Coulombic interactions. While excitonic levels in bulk semiconductors have excitonic levels of a few meV below the band gap, this energy in carbon nanotubes is much larger, on the order of a few hundreds of meV. Then, the scattered exciton emits (or absorbs) a phonon before relaxing back to the ground state. The second, third, or higher order scattering processes involve two, three or more scattering events, respectively. The Raman process is sometimes called one-phonon, two-phonons or multi-phonons Raman process, depending on the number of phonons emitted or absorbed during the process [93, 109].

2-2-1 Raman Spectra of Graphene

The strongest peaks observed in the Raman spectrum of a monolayer of graphene (shown in Figure 2.7) are the D band at ~1345 cm^{-1}, the G-band at ~1582 cm^{-1} and 2D band at ~2700 cm^{-1}. The G band corresponds to in-plane vibrations of sp^2 hybridized carbon atoms related with the degenerate (TO and LO) phonon modes at the Γ point. It is the only signal associated with a first order Raman scattering process.

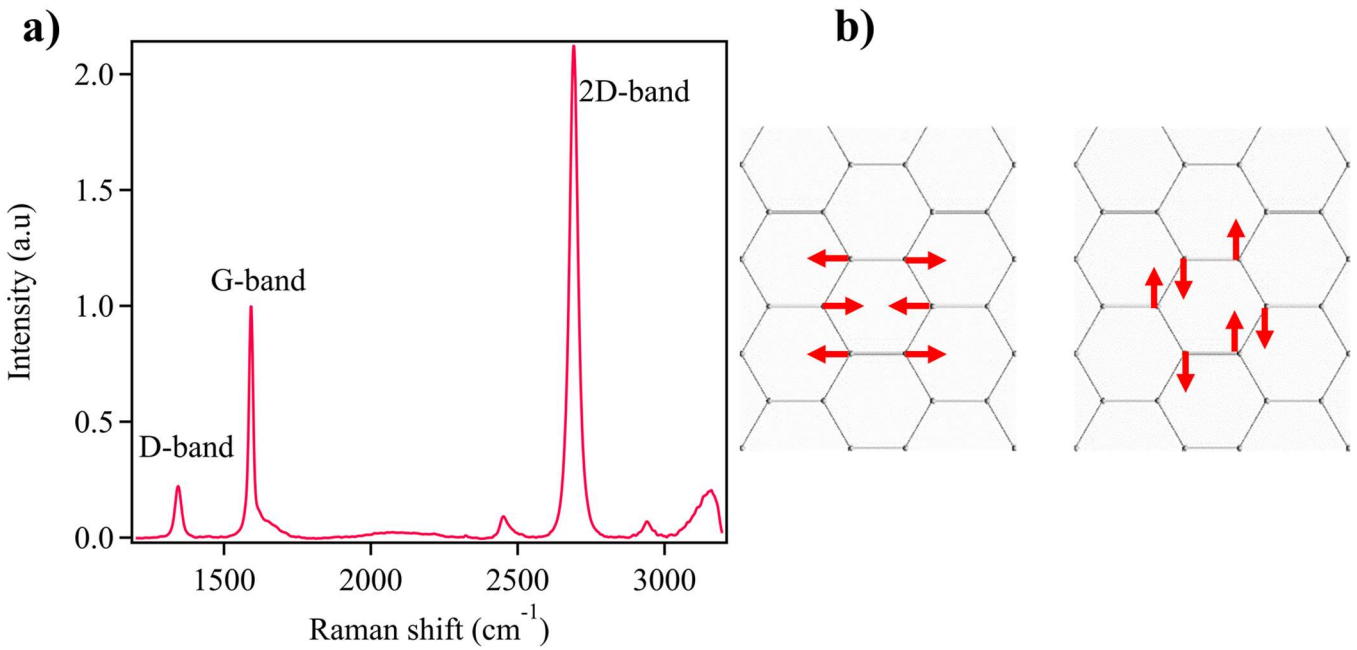

Figure 2.7. a) Raman spectra of graphene with laser excitation 514 nm. b) A scheme of the lattice vibration corresponding to the G band signal

Another peak called the D′ band is often detected ~1625 cm^{-1}. The D and D′ bands are signatures of disorder and related to the presence of defects in the lattice. These modes involve second-order scattering where one elastic scattering event is driven by a defect and the other inelastic scattering event is due to phonon scattering[113, 114]. Located at higher wavenumber, the 2D band is a two-phonons process (also a second-order process), involving two iTO phonons near the K point (Figure 2.8).

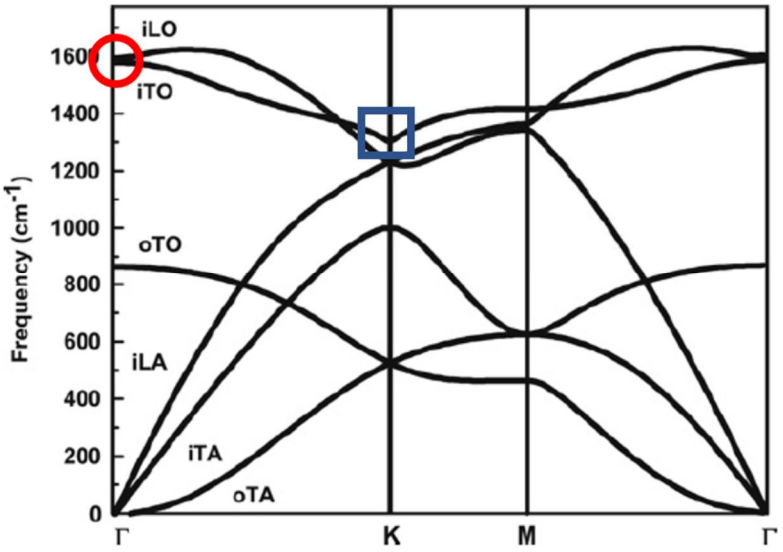

Figure 2.8. Calculated phonon dispersion relation of graphene showing the iLO, iTO, oTO, iLA, iTA and oTA phonon branches. Adapted from reference [115][115]. Copyright (2008) by the American Physical Society

2-2-2 Raman Spectra of Single Walled Carbon Nanotubes (SWCNTs)

Most of the Raman-active phonon modes of graphene are observed as well in carbon nanotubes, such as the D band, the G band and the 2D band (Figure 2.9). However, another peak is detected at low wavenumbers and is related to the radial breathing modes (RBMs), which is characteristic of carbon nanotubes.

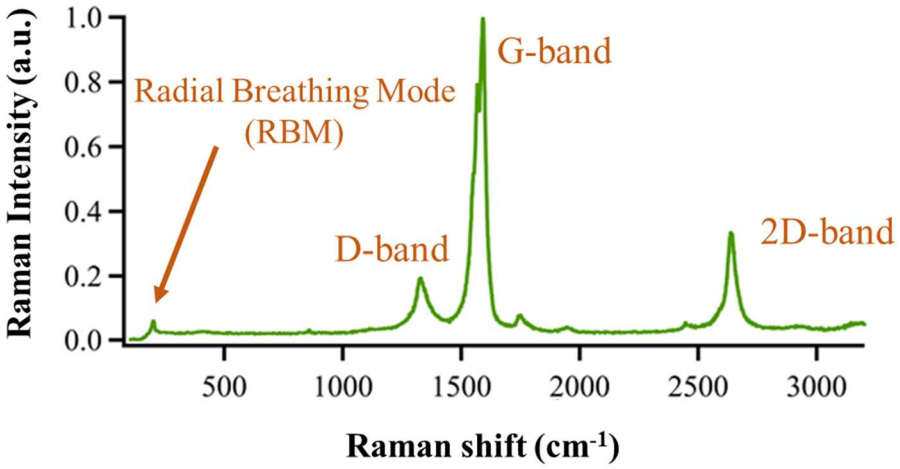

Figure 2.9. A typical Raman spectrum of single-walled carbon nanotubes with the main modes, as indicated.

Radial Breathing Mode (RBM): The RBM is a Raman signature of carbon nanotubes which corresponds to the expansion and contraction of the nanotube along the radial direction (Figure 2.10). It is related to out-of-plane stretching vibrations where carbon atoms move coherently in the radial direction. It is a first order Raman process detected between 100 cm^{-1} and 500 cm^{-1}. Its frequency is inversely proportional to the carbon nanotube diameter as:

$$\omega_{RBM} = A/d_t + B \qquad (2\text{-}2)$$

where the A and B parameters are determined experimentally [116-119].

The B parameter is associated with an environmental effect on ω_{RBM}, rather than an intrinsic property of SWNTs. The environmental effect can be linked to nanotube-nanotube interaction in the case of bundling, or nanotube-environment interaction, such as the surfactants used for the dispersion of SWNTs in water or the substrates on which the tubes are deposited [120]. For isolated carbon nanotubes deposited on an oxidized silicon substrate, C = 248 cm^{-1}·nm and $B = 0$ [121], while for bundles C = 234 cm^{-1}·nm and $B = 10$ cm^{-1} [119].

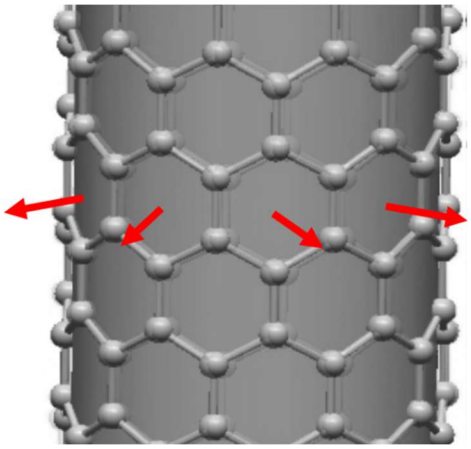

Figure 2.10. Schematic image showing the atomic vibrations for the RBM mode

High Energy Modes: In CNTs, the G band splits into two modes called G^+ (larger energy) and G^- (smaller energy) modes. The curvature of the carbon nanotubes causes a rehybridization of the carbon valence orbitals from sp^2 (planar graphene) to sp^3 -like. The softening in the Raman peaks occur because of the different strengths of this hybridization of the orbitals depending on the longitudinal and radial directions. This mode softening for semiconducting tubes is associated with atomic displacements perpendicular to the tube axis, which implies that the transverse optical (TO) phonon is soften more than the longitudinal optical (LO) phonon (displacements parallel to the tube axis). Longitudinal optical (LO) phonons become less weakened by the rehybridization and therefore yield a much smaller softening of the phonons [122,123].

In the metallic nanotubes, this dependency on curvature and rehybridization occurs for the same reason as semiconducting nanotube, but phonons are further affected by a Kohn anomaly in the band structure [124-126]. The Kohn anomalies effect is when the atomic displacements perturbs the energy of electrons at the Fermi surface, i.e. near the Fermi level. These electrons rearrange themselves during the process, which screens the potential due to atomic vibrations and softens further the vibrational frequency. This strange behavior of the phonon dispersions, called the Kohn anomaly, is a central feature for this thesis [127]. The Kohn anomaly softens only the LO mode and causes an inversion of the sequence between TO and LO for the lowest frequency peak. That is, for the metallic tube, the lowest frequency peak is a LO mode, whereas it is a TO mode for the semiconducting tube.

As seen in Figure 2.11, the lineshapes of G^- peaks are significantly different between metallic and semiconducting tubes. The latter exhibits a sharp Lorentzian shape for both G^+ and G^-, while for metallic tubes, the linewidth of the G^- peak presents an asymmetric Breit-Wigner-Fano (BWF) lineshape due to electron-phonon interaction [109].

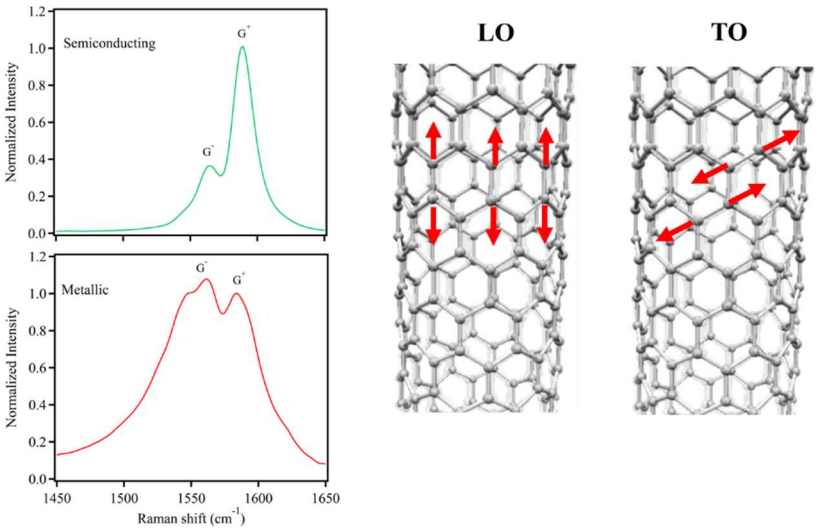

Figure 2.11. Raman G-band of semiconducting and metallic nanotubes. For semiconducting nanotubes, there are two sharp Lorentzian peaks while the G- peak of metallic species is broad and asymmetric, typical of a Breit-Wigner-Fano lineshape. Motions of LO and TO phonon modes of SWNTs are shown on the right panel.

Disorder Induced Mode. The Disorder induced mode, which is also called the D band, is observed in the range between 1300 $cm^{-1}$and 1400 cm^{-1}. As discussed already in the section on the Raman modes of graphene, the D band is common and seen in all sp^2-hybridized disordered carbon materials; the presence of this mode is attributed to disorder and is generally induced by the presence of heteroatoms, vacancies or other defects [128].

Like the D-band in graphene, this feature is a second-order Raman process, which involves high momentum iTO phonons near the K-point. Because the scattering photon has a low momentum at typical wavelengths for Raman, momentum conservation implies that only scattering at Γ point

(q=0) is allowed and therefore, the process most involved a high momentum (non-Γ point) phonon and a defect to compensate the extra momentum[129].

2D-Band. The 2D band (also referred to as G' band) is located around 2700 $cm^{-1}$and originates from a second order process with two phonons of opposite momentum, similar to the graphene case [130].

2-3 Charge Transfer in Graphene and Carbon Nanotubes

The kinetics of charge transfer processes at the electrochemical interface of graphene (or carbon nanotubes) and electron donor (or electron acceptor) species can be explained by the Marcus-Gerischer theory. During an electron transfer process, charge transfer is the fastest when the overlap of the occupied / unoccupied states of graphene (or carbon nanotube) matches that of the unoccupied / occupied states of the electron donor (or acceptor) species[131]. It is also known in electrochemistry that an oxidation-reduction (redox) reaction is a chemical reaction, which involves a transfer of electrons between two species. For this reaction, the Nernst equation provides a quantitative relationship between the potential and concentration of species. The relation is obtained from arguments based on thermodynamics. For the simplest reaction: $ox + ne^- \leftrightarrows red$, where *ox* and *red* are species in their oxidized and reduced style, respectively, the standard the Gibbs free energy, ΔG , can be calculated from following equation [24]:

$$\Delta G = \Delta G^0 + RT\ln Q \ . \qquad (2\text{-}3)$$

In this equation, ΔG^0 is the standard-state free Gibbs energy and Q is the reaction quotient. The potential E of this electrochemical reaction is defined by:

$$\Delta G = -nFE \quad \text{and} \quad \Delta G^0 = -nFE^0 \qquad (2\text{-}4)$$

, where F is Faraday constant, n is the number of transferred electrons and E^0 is the standard potential. From (2-3) and (2-4) equations the Nernst equation could be reached:

$$E = E^0 - \frac{RT}{nF}\ln Q = E^0 + \frac{RT}{nF}\ln\frac{a_{Ox}}{a_{Red}} \qquad (2\text{-}5)$$

For simplicity, the activity coefficients, an Ox and a Red are considered at low concentrations to be one. Therefore, Nernst equation could be written in new form, by converting the ln to logarithmic and the activity to concentration:

$$E = E^0 + \frac{2.303\,RT}{nF} \log \frac{[Ox]}{[Red]} \qquad (2\text{-}6)$$

To understand which species are electron donor or electron acceptor, the standard potential is used. The standard potential is defined relative to a standard hydrogen electrode (SHE) reference with a potential of 0 V. Any chemical species that accept electrons from H^+/H_2 redox couple is defined as having a positive standard potential; any system donating electrons to this redox couple is defined as having a negative standard potential. According to the International Union of Pure and Applied Chemistry (IUPAC) convention, all electrode potentials are considered as reduction potentials; therefore, the electrode reaction reads in the reduction direction [24].

In electrochemistry the potential of a species can be taken as absolute-electrode potential. The absolute electrode potential is the difference in electronic energy between a point inside the species system (Fermi level) and a point outside the system (such as the potential of a free electron in vacuum) and is expressed (in Volt units) as [132]:

$$E_{\text{abs}} = -(E_{\text{SHE}} + 4.44) \qquad (2\text{-}7)$$

Therefore, the Nernst equation in terms of absolute potential could be written:

$$E_{\text{redox(abs)}} = -(E_{\text{redox}} + 4.44) = \frac{\phi(\text{eV})}{e} \qquad (2\text{-}8)$$

where $\phi(\text{eV})$ is the work function (Figure 2.12).

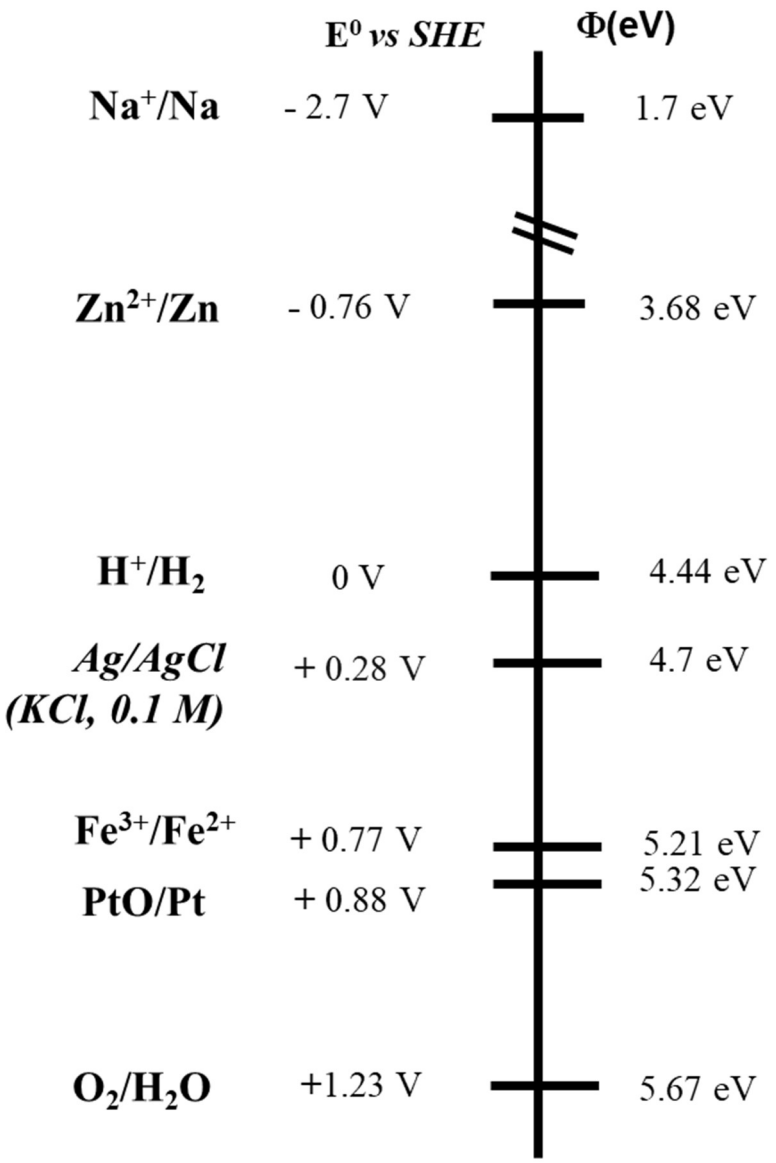

Figure 2.12. Relationship between SHE and absolute potential relative to the vacuum level.

In electrochemistry language, charge transfer is mainly driven by the difference between the electrochemical potentials, E_{redox}, of the redox couple and the internal potential, E_{f}, of graphene (or carbon nanotubes). In solution, the reaction proceeds until an equilibrium is reached between the two systems (i.e., $E_{\text{redox}} = E_{\text{f}}$), resulting in the electrochemical doping of those systems[24].

As mentioned above, the doping of graphene depends on the position of the electrochemical redox potential, E_{redox}, and the Fermi level of graphene. The E_{redox} is therefore the equivalent of the

Fermi level of the redox couple, which is the energy required to add or remove an electron in/from the redox couples and is usually referenced to as the standard hydrogen electrode (SHE)[133]. When the Fermi level of the redox couple (E_{redox}) is higher (lower) than the Fermi level of graphene (or carbon nanotubes), the electrons (holes) induced by a reaction will flow to graphene (or carbon nanotube) until the equilibrium is met, $E_{redox} = E_f$, and graphene (or carbon nanotubes) become n-type (p-type) doped.

2-4 Effects of Doping on the G Band

Raman spectroscopy is a powerful non-destructive technique that has been widely used to study and measure doping in graphene [134-136] as well as in carbon nanotubes [137-139]. The G-band of graphene and carbon nanotubes, which comes from a first-order (one-phonon) Raman-scattering process, has been used for characterizing and measuring the doping in graphene and carbon nanotubes. The Raman G-band phonon modes in a doping situation depends on the nature of electron-phonon coupling in these two systems. According to perturbation theory, the electron-phonon interaction is considered as a perturbation and causes a phonon energy renormalization that depends on the electronic structure and the Fermi level [140-143]. The deformation of the electronic structure and deformation of the phonon structure happen during the electron-phonon interaction, which are called renormalization of the electron energies by the phonon and of the phonon energies by the electron, respectively. This electron–phonon coupling causes a controllable modification to the G-band frequency as a function of the Fermi level.

The frequency of the Γ-point LO- and iTO-phonon modes in graphene (also in SWNTs) can be shifted due to the electron–phonon (e–ph) interaction and can be calculated via the perturbation theory. The phonon energy, including the e–ph interaction, can be written as:

$$\hbar\omega_\lambda = \hbar\omega_\lambda^0 + \hbar\omega_\lambda^2 \qquad (2\text{-}9)$$

where λ are for LO and iTO, $\hbar\omega_\lambda^0$ is the phonon frequency without considering the e–ph interaction and $\hbar\omega_\lambda^2$ is a perturbation term, which is given from perturbation theory to be:

$$\hbar\omega_\lambda^2 = 2\sum_k \frac{|\langle eh(k)|H_{int}|\omega_\lambda\rangle|^2}{\hbar\omega_\lambda^0 - (E_e(k) - E_h(k)) + i\Gamma_\lambda} \times [f(E_h(k) - E_F) - f(E_e(k) - E_F)]. \qquad (2\text{-}10)$$

In this equation, $\langle eh(k)|H_{int}|\omega_\lambda\rangle$ is the matrix element related to the creation of an electron– hole pair (exciton), $E_e(k)$, $E_h(k)$ are electron and hole energies, respectively and Γ_λ is the decay width. The energy of electron -hole pair is $E = E_e(k) - E_h(k)$ (Figure 2.13).

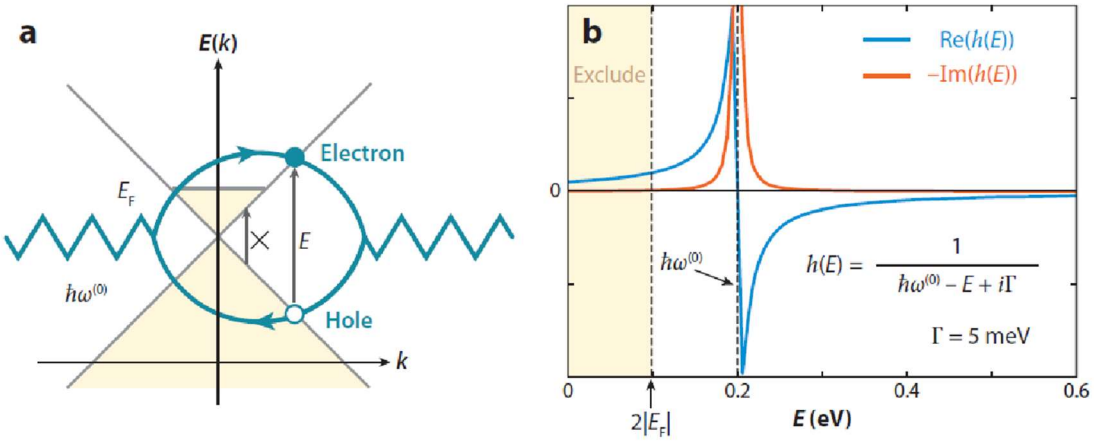

Figure 2.13. (a) An intermediate electron-hole pair state that contributes to the energy shift of the optical phonon modes is shown. A phonon mode is illustrated by a zig-zag line, and an electron-hole pair is represented by a loop. The low-energy electron-hole pair $0 \ll E \ll 2E_F$ is forbidden (b) The plot for the real and imaginary parts of $h(E)$ is made for $\Gamma = 5\,meV$. Adapted from reference [144] [144]. Copyright (2008) by the American Physical Society.

The matrix element for the creation of an electron-hole pair (exciton) is a smooth function of $E = E_e(k) - E_h(k)$, which appears in the denominator of the equation. Therefore, the $\hbar\omega_\lambda^2$ depends on its energy. The real and imaginary part of the energy of electron-hole pair, $h(E) = \frac{1}{(\hbar\omega^0 - E + i\Gamma)}$, which is in the denominator of the equation, can be plotted versus the excitation energy E (Figure 2.13b). The real part (Re$(h(E))$ has the negative and positive value in relation of $\hbar\omega^0$ and therefore, has positive and negative contributions to $\hbar\omega_\lambda^2$, where the e-ph interaction causes the upshift (downshift) in the phonon frequency.

If the energy of an electron–hole pair (exciton) is less than double of the amount of Fermi energy ($E < 2E_F$), it cannot contribute to the energy shift (yellow regions in figure 2.13 a,b) because of the Fermi distribution function $f(E)$ in Eq. (2-10) tends to zero. Therefore, the phonon energy

can be controlled by an intermediate electron–hole pair (exciton) and therefore, change with the Fermi energy, E_F. If the $E_F = \frac{\hbar\omega^0}{2}$, $\hbar\omega_\lambda^2$ has the minimum value and the maximum of downshift and phonon softening could be seen [93, 144].

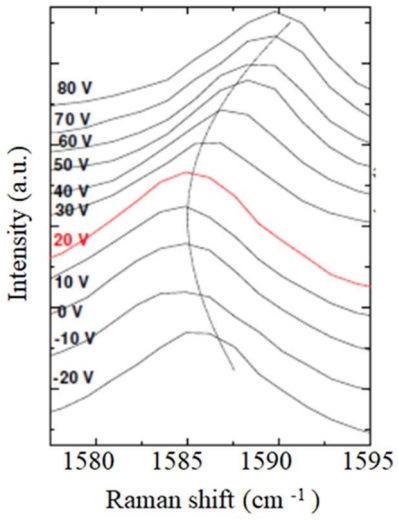

Figure 2.14. Shifting of the G band of graphene measured at room temperature as a function of gate Voltage. Adapted from reference [135][135]. Copyright © 2007, Nature Publishing Group

The experimental results on graphene and carbon nanotube show an upshift and downshift of the frequency of the G band with n doping and p doping. The shift in frequency of the G band with the Fermi level is predicted by the perturbation theory and the linear dependency as well (Figure 2.14). The hardening and softening of the G band can be also explained by a lattice distortion induced by doping. That is, p-type doping induces a hardening and upshifting of the G band frequency (ω_G) and n doping causes the softening and downshift of the frequency ω_G [93].

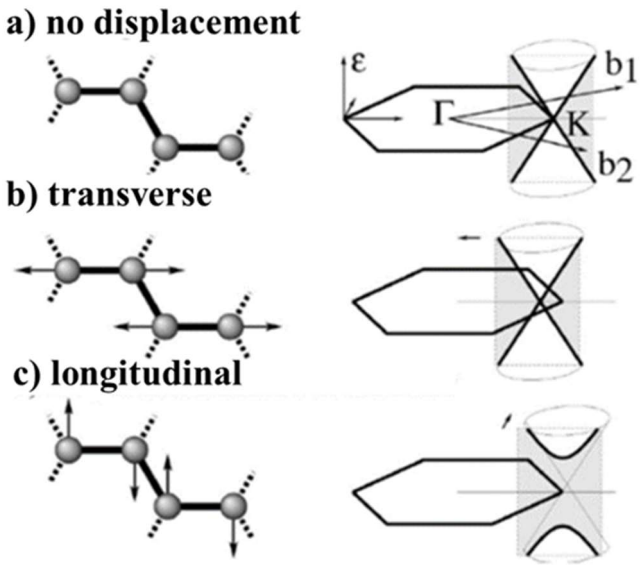

Figure 2.15. (a) Electronic band structure of graphene near the K point with the band structure of metallic carbon nanotube overlapped in the gray section with the cutting line. Schemes (b) and (c) show the changes in the electronic band structure caused by the activation of iTO (transverse) and LO (longitudinal) phonon modes. Adapted from reference [93][93]. Copyright © 2011, John Wiley and Sons

In carbon nanotubes e-ph interaction is different for LO than for iTO phonons and the presence of cutting lines in the Brillouin zone also has a significant influence. For metallic carbon nanotubes, the quantized line crosses the K point and the valence and conduction bands are degenerate (crosses) at this point (Figure 2.15a). The displacement of the G-band iTO phonon causes the changing in the position of the crossing point along the cutting line direction, and no major change in the electronic structure can be seen (Figure 2.15b). Meanwhile, the displacement of the G-band of the LO phonon (Figure 2.15c) moves the crossing point perpendicular to the cutting line direction, thus opening a band gap. This effect has a high impact on the electron-phonon coupling, which is stronger than in graphene due to a significant change of the total electronic energy of the carbon nanotube. According to equation (2-10), the strong e-ph coupling involving LO phonons causes the strong dependency of this coupling to the Fermi level and a softening of this mode as a function of E_F[145, 146] (Figure 2.16).

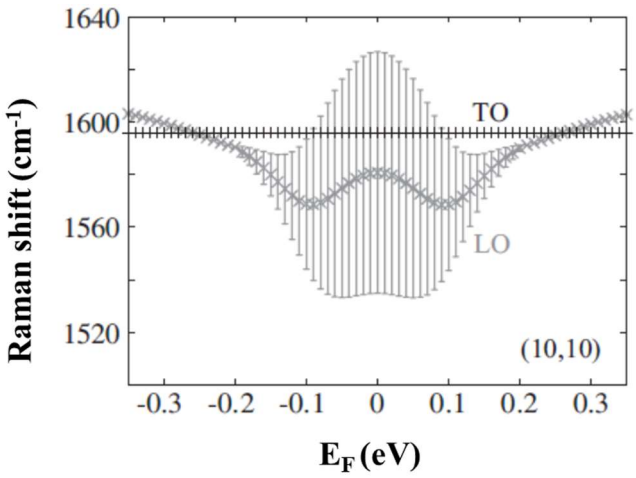

Figure 2.16. The EF dependency of the LO (gray curve) and iTO (black curve) phonon energy in the case of the (10, 10) armchair nanotube. Adapted from reference [144] [144]. Copyright (2008) by the American Physical Societ

There also is a renormalization of the phonon energy for semiconducting carbon nanotubes due to phonon-electron coupling, but the coupling is much weaker than in metallic tubes due to the large electronic band gap compared to the phonon energy [147].

2-5 Effects of Doping on the D-Band and RBM (Radial Breathing Mode)

The Raman D-band is assigned to a double resonance process involving defects and iTO phonons located in the vicinity of the K point of the Brillion zone. The Raman D-band is enabled by iTO phonons and defects simultaneously. The frequency of the SWCNT D-band shows a dependency on eventual shifts of the Fermi level and this is also true for the G-band. Changing the Fermi level causes in effect a modification in the equilibrium lattice parameters, which is a consequence of the strengthening/weakening of the phonon modes.

Changing the Fermi level by an increase in carrier concentration (e.g. electron doping) could cause further shielding of ions in the lattice, which weakens the interactions among neighboring lattice ions and induces a red shifting of the phonon frequency. Conversely, reducing the number of carriers (e.g. hole doping), strengthens the lattice ion interactions and blue shifts the phonon

frequency. Another explanation of the frequency shifting by doping (by electrons or holes) is the effect on the strength of the electron-phonon interaction, which leads to the phonon self-energy renormalization, which modifies the frequency and lifetime of the phonons[144].

As mentioned before, the RBM is a landmark of carbon nanotubes and it is related to breading vibrations of carbon atoms in radial direction. The RBM frequency is dependent to the diameter and chirality of the carbon nanotube. For metallic SWNTs, a shifting of the RBM frequency as a function of Fermi level is expected. This phonon frequency shift is similar to that discussed for the G band but it is much smaller. [144] The RBM peak intensity is a function of energy of the laser. The RBM is intense when the incident light or the scattered light is in resonance with the SWNT optical transition energies E_{ii}. The doping of carbon nanotubes could change the E_{ii} and this induces changes of the resonance conditions and hence the RBM intensity. Therefore, the doping of carbon nanotubes could have the effect on the intensity of the peak, but only a weak dependency on the RBM frequency.

Chapter 3: Methodology

This chapter intends to give a brief description of fabrication process and preparation of graphene and carbon nanotube samples that are used thought this thesis. This chapter includes seven sections. The first section presents the growth of graphene and its transfer on a patterned substrate and describes the final preparation of graphene samples for Raman measurements. Second section is devoted to the purification, functionalization and preparation of thin layers of carbon nanotube on a patterned and describes as well the functionalization procedures of the silicon substrates. The following two sections present the details on the preparation of the buffer solutions and show how the electrical sheet resistance measurements were performed. The last three sections are devoted to the preparation of samples for Transmission Electron Microscopy, Atomic Force Microscopy and Raman measurements. These sections also provide the characteristics of the instruments.

3-1 Preparation of Graphene Electrodes

3-1-1 Growth of graphene

A monolayer of large area graphene was grown on copper foil by chemical vapor deposition (CVD). The growth makes use of a protocol modified in our laboratories by S. Choubak et al. and the procedure is the following[156]:

1- The copper foils were cut into pieces of 2 x 2 cm (Alfa Aesar, 99.8% purity, 0.025 mm thick) and chemically cleaned in 1 M acetic acid (Fisher chemical, Reagent Plus > 99.7%) at 60 ºC, followed by acetone (Fisher chemical, Reagent grade) and then 2-propanol (Fisher chemical, Reagent grade) rinses for 10 min in each step. At the end the pieces were blown-dried with nitrogen.

2- The foils were placed without delay on a quartz slide in the CVD furnace.

3- The system was pumped down to a vacuum of 5 $x10^{-6}$ Torr using a turbo molecular pump. The copper foils were then heated to 1000 ºC and annealed at this temperature for 30 min under the flow of H_2 (Praxair, UHP Grade: 5, O_2 <1 ppm, partial pressure: 50 mTorr). Then, the chamber was purged with carbon dioxide (CO_2, Praxair, Anaerobic, Grade: 4; 99.99% purity) for 20 seconds to burn residual carbon from the copper surface

4- Finally, methane (CH_4, Air Liquid, RES Grade: 5N, O_2 <15ppm, partial pressure: 450 mTorr) was introduced into the chamber and growth is carried out at temperatures 1000 °C for 10 min.
5- The chamber was cooled down under a flow of hydrogen to room temperature.

The graphene thus grown by this method is of high-quality and grows on both sides of the copper substrate. The preferred layer used in our studies is the one directly exposed to the gas feedstocks.

3-1-2 Preparation of the Patterned Substrates

Patterned surfaces were prepared using standard photolithography followed by a deposition of the metal by e-beam evaporation on the silicon substrate coated with a 300 nm oxide (SiO_2), according to several steps:

1- Spin coating a photoresist onto the substrate and bake out at 90 °C for 15 min.
2- Exposure of photoresist on the substrate to the UV light through a patterned mask, which contains small crosses and numbers (using Karl Suss MA-6 mask aligner).
3- Development of the resist in PG-remover solution at room temperature to remove the irradiated part of the resist.
4- Evaporation with an e-beam evaporator of titanium (5 nm) and platinum (20 nm) on the patterned sections.
5- Removing the resist in hot acetone for few minutes.

The pattern simplifies the identification of the sample regions to be probed by Raman spectroscopy and allows repeated experiments in the same spot. The patterned substrates were cleaned by sonicating 15 min each in acetone (reagent grade) and isopropanol (reagent grade).

3-1-3 Graphene Transfer

The use of the graphene, which is formed on copper, requires transfer onto an oxidized substrate. The transfer method was adapted from the method by Ji Suk *et al.*[157] and modified in our group. The transfer procedure consists of the following steps:

1- Spin coating one side of graphene/copper foils with poly methyl methacrylate solution (PMMA, M.W. 15000 GPC, Acros organics, 4% in chlorobenzene) at 4000 rpm for 30 s and drying in the air for 1 hour.

2- As said before, graphene is grown on both sides of the copper foils. To extract a monolayer of graphene, the layer on the bottom side of the copper foil is etched by Reactive Ion Etching (RIE) technique using oxygen at 125 mTorr for 1 min at 50W power (Technic Serie 800 RIE)

3- Etching of copper is performed in a solution of ammonium persulfate (0.1M, ACS 98+%, Acros Organics) at room temperature. The following reaction shows the mechanism of etching the copper: $Cu + (NH_4)_2S_2O_8 \rightarrow CuSO_4 + (NH_4)_2SO_4$.

4- Transferring and rinsing of graphene in contact with PMMA (PMMA/graphene) into the Milli-Q water to remove the residue of ammonium persulfate.

5- Transferring the PMMA/graphene onto the target substrate (as illustrated in the Figure 3.1)

6- After drying, heating of the PMMA/graphene/substrate in a low vacuum at 150°C for 2 hours. This step removes the adsorbed water between the graphene and the substrate and helps creating a better adhesion.

7- Putting PMMA/graphene/substrate in the acetone bath to remove the PMMA and drying in air.

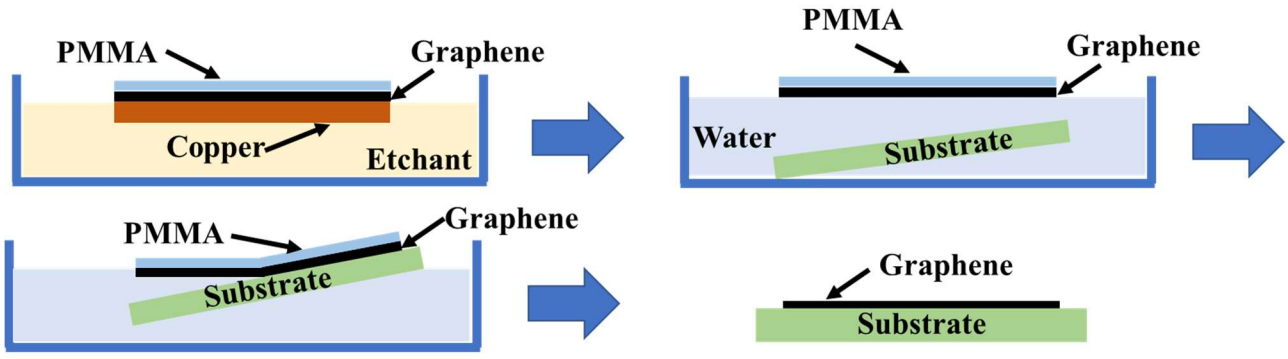

Figure 3.1. Schematic of transferring graphene to the flat substrate

3-1-4 Platinum Coating onto Graphene

After transferring the PMMA/graphene/substrate, the PMMA was removed by dissolving in acetone 20 min following by isopropyl alcohol (IPA) for 5 minutes. Then, a deposition of a thin layer of platinum (6 nm) was performed by e-beam evaporation at base pressure of 1×10^{-6} torr (Edwards FL-400).

3-2 Preparation of Carbon Nanotube Electrodes

3-2-1 Carbon Nanotube Sources

In this thesis, different sources of single walled carbon nanotubes (SWCNTs) were used to prepare the samples:

1- Plasma torch SWCNTs provided by Raymor company. This product is unpurified and contains 27% of metal (catalyst) residues. The diameters of the nanotubes are in the range 0.9-1.5 nm and the lengths are between 0.3 and 4 μm.

2- Laser ablation SWCNTs received from the National Research Council of Canada[158]. The metal content is less ~5.8% and the nanotube walls are highly crystalline, which make them resistant to defects. The laser-ablation SWCNTs have a narrow diameter distribution, between 1.1 and 1.5 nm, and the lengths are around a few hundreds of nm to several micrometers.

3- Arc discharge metallic SWCNTs provided by Raymor NanoIntegris and containing metallic nanotubes at 99% purity. The SWCNTs are wrapped using a mixture of sodium cholate (SC) and sodium dodecyl sulfate (SDS). The diameter range of this kind of SWCNTs is around 1.2-1.7 nm and the lengths are in the 300 nm to 5 μm range. The metal content is less than 1%.

3-2-2 Purification of SWCNTs

The plasma torch SWNTs were purified by the producer (Raymor) using a method in Martel group described previously[159]. The SWCNTs were purified by refluxing in 3 M nitric acid (reagent grade) at 130°C for overnight and filtered on a Polytetrafluoroethylene (PTFE) filter (1.2 μm pore size, Sartorius), followed by washing in sodium hydroxide (3 M, reagent grade) and hydrochloric acid

(3 M, reagent grade) to remove amorphous carbon and neutralize the SWCNTs respectively. The final step consists of washing in Milli-Q water and filtrating on the PTFE membrane.
The SWCNTs produced by laser ablation were purified by refluxing in concentered nitric acid (reagent grade) 130°C for overnight followed by washing in Milli-Q water and filtering on PTFE membrane. For deposition of metal nanoparticles on the SWCNTs, the good number of defects on the side wall of SWCNTs is needed. Therefore, refluxing in concentered acid overnight is necessary to create defects on the rigid walls of this kind of carbon nanotubes.

To remove the wrapping polymer around the metallic SWCNTs, 2 mL of wrapped SWCNTs (10 µg/ml) was sonicated for 15 min. The mixture was refluxed for six hours at 70ºC. The solution was centrifuged at 12000 rpm for 10 min, followed by thorough washing with distilled water several times (10 times). Finally, the SWCNTs were dried at 50ºC.

3-2-3 Platinum Deposition on Plasma Torch and Laser Ablation SWCNTs

Two methods of deposition were used to prepare Pt-coated SWCNTs for the Raman experiments. The first method employed an electron beam (e-beam) evaporator (a basic vacuum of 1×10^{-6} torr, Edwards FL-400) to deposit about 10 nm of platinum on a mat of entangled SWCNTs supported on the oxidized silicon wafer.

The second method involves a one pot preparation from platinum nanoparticles grown in solution using Chloroplatinic acid hydrate ($H_2PtCl_6\cdot xH_2O$, ≥99.9%) and sodium borohydride ($NaBH_4$, 98%) as the reducing agent. First, SWCNTs were ultrasonically dispersed in deionized water mixed with 2-propanol (reagent grade). The metal precursor ($H_2PtCl_6\cdot xH_2O$) was then added to the solution to reach a total metal content of 40 wt. % *vs.* the SWCNTs. The platinum salt was reacted with $NaBH_4$ (molar ratio of $PtCl_6^-$: $NaBH_4$ of 1 to 50) at 80 °C for 3 h under vigorous agitation to ensure its complete reduction. Finally, the final mixture was filtered, washed and dried under vacuum at 120 °C for 4 h[160].

3-2-4 Platinum Deposition on Arc-Discharge Metallic SWCNTs

The one pot procedure consist of sonication of 2 ml of sodium dodecyl sulfate (SDS) and sodium cholate (SC) wrapped metallic carbon nanotubes (10 µg/mL, 99%) for 15 minutes and adding the respective metallic salt (Chloroplatinic acid hydrate ($H_2PtCl_6\cdot xH_2O$, ≥99.9%), palladium

dichloride ($PdCl_2$, ≥99.9%) and Ruthenium trichloride ($RuCl_3$, ≥98%) in a proportion of 1:50 (nanotubes: metal precursor). The resulting mixture was refluxed for six hours at 70 °C. The solution was centrifuged at 12000 rpm for 10 min to obtain the pellet at bottom followed by thorough washing with distilled water several times (10 times) to remove any un-reacted salt from the solution. Finally, the pellet was dried at 50 °C.

3-2-5 Preparation of Patterned Silicon Substrate

The patterned substrate (which is described in the previous section) was cleaned by sonication steps for 15 min each in acetone and isopropanol (IPA) followed by 15min in a piranha solution (using 3 parts of sulfuric acid (H_2SO_4 concentrated, reagent grade) and 1 part of hydrogen peroxide (H_2O_2 , 30% reagent grade) to oxidize the surface of substrate and prepare the surface to the attachement of the aminosilane to the surface. Then, the substrate is washed with Milli-Q water.

In order to functionalize the surface with aminosilane, the vapor-phase silanization method was used[161, 162]. The procedure consists of placing the substrate on a glass slide suspended above a small crystallization dish containing 1 mL of (3-Aminopropyl)triethoxysilane (APTES). The desiccator was vacuum pumped for one minute and the chamber was sealed for an additional thirty seconds. Finally, the APTES layer was annealed in air for 1 h at about 100ºC in a conventional oven. The reaction is schematized in Figure 3.2. The Coulombic attraction between the positively charged –NH2 groups on the surface and the negatively charged SWNTs makes the SWCNTs stick well on the surface of substrate.

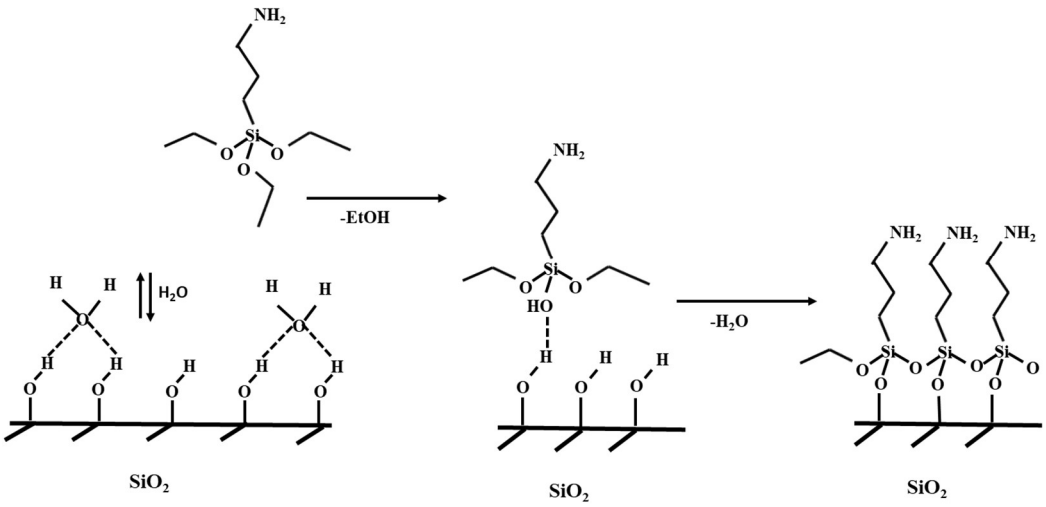

Figure 3.2. Schematic representation of functionalization of oxidized silicon substrate.

3-2-6 Deposition of Parylene-C on Silicon Substrates

In some experiments, the parylene-C polymer, which is chemically inert, was deposited on silicon substrate to remove or reduce the effect of the functional groups at the oxide surface of the silicon substrate. Parylene-C polymer was deposited on the oxidized silicon substrate (300 nm oxide) using the SCS 2060PC Parylene deposition system from Kisco company. The thickness of the polymer on silicon was around 1 μm.

3-2-7 Deposition of SWCNTs on Silicon Substrates

Two methods were used to deposit the functionalized or non-functionalized SWCNTs. The first was by drop casting the dispersed SWCNTs in a IPA solution onto the patterned and silanized silicon substrate. The second method was inspired from Rinzler and coworkers[163], which is schematically shown in Figure (3.3). Thin films of SWCNTs were prepared by vacuum filtration of an aqueous dispersion of SWCNTs (7.5×10^{-9} g/L) through a nitrocellulose membrane and dried in air. The harsh sonication of SWCNTs for 1 hour and the vacuum filtration play important role in this procedure. At the beginning, the vacuum level is controlled by a relief valve to reach a slow flow for the filtration (one drop of water in 30 second). This ensures a better contact between SWCNTs and the filtration membrane. At the end of filtration, the vacuum level is increased to reach fast filtration (one drop in 1 second). Then we transferred the membrane / SWCNTs to a patterned substrate consisting of an oxidized silicon wafer (Si/SiO_2, thickness = 300 nm) by

placing the membrane side that contains SWCNTs directly to the surface of silicon substrate. Before transferring, it is important to soak the membrane in dichlorobenzene for 1 min, which ensures a complete removal of the water from the porous membrane; this is critical to gain a good adhesion between SWCNTs of the membrane and the substrate. Then, the membrane was placed in the silicon holder and immersed in the petri dish with the funnel inside (upside down). Then acetone was added to the petri dish. The end of the funnel is connected to the vacuum and by increasing the vacuum the level of acetone is raised to cover the whole silicon wafer. The sample was kept in the acetone for 45 min to dissolve the membrane. The final step consisted of soaking in IPA for 5 min and drying the sample. The thickness of the films, as measured by AFM, were around 3 to 6 nm. In Figure 3.4, we present a typical AFM image of one of these samples having a thickness between 3 to 5 nm.

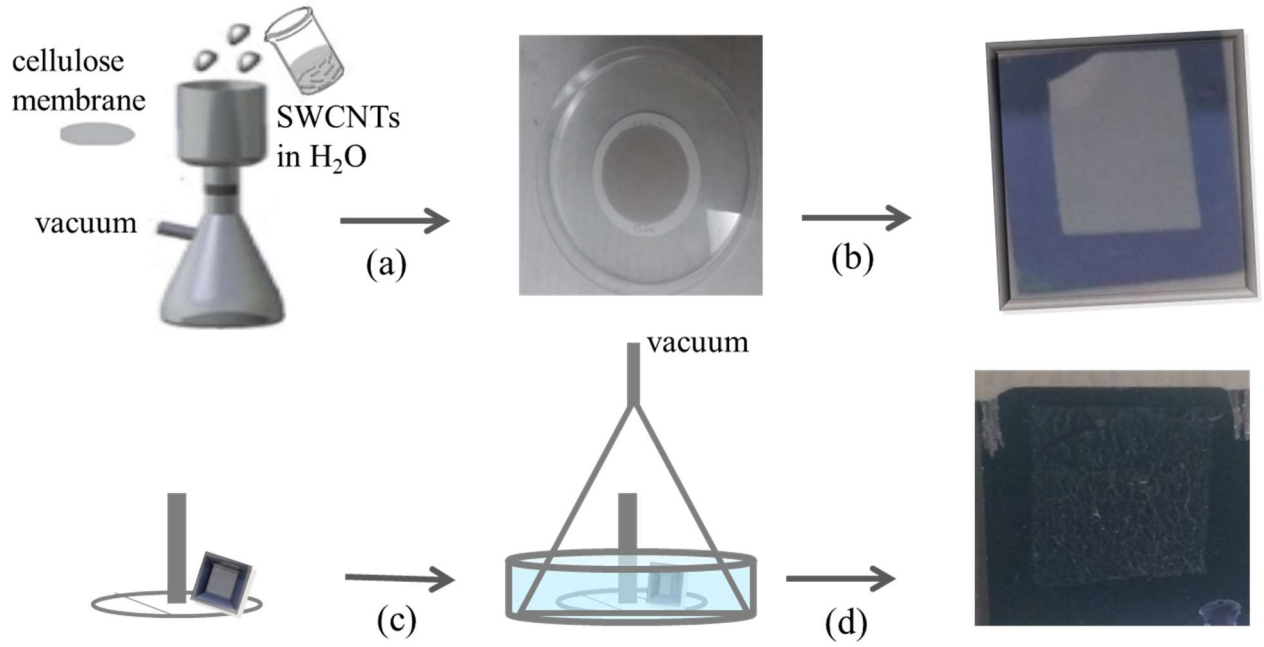

Figure 3.3. Schematic representation of a SWCNTs film on a silicon substrate: (a) A SWCNT film prepared by filtration of dispersed SWCNTs in water using a nitrocellulose membrane. (b) Film transfer step on silicon substrate with the silicon holder. (c) The silicon holder placed inside the upside-down funnel. Increasing the vacuum raises the level of acetone to cover the substrate. (d) A picture of SWCNTs on silicon substrate by dissolving membrane.

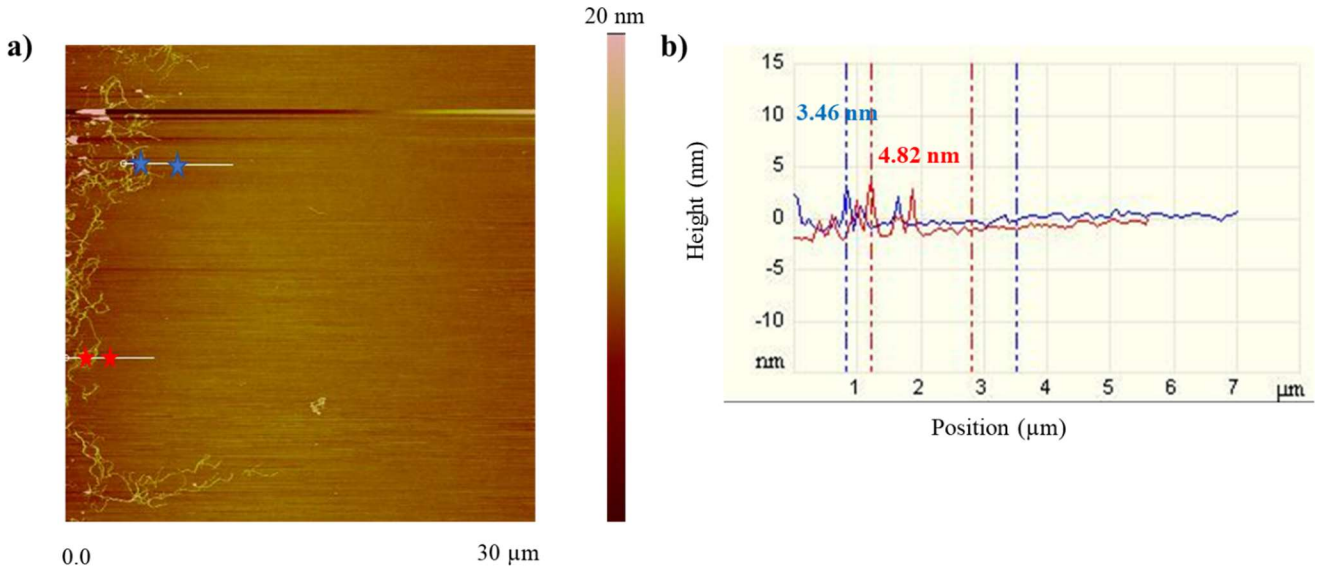

Figure 3.4. AFM height image of the border of a single walled carbon nanotube film to estimate the thickness of the film (thickness between blue and red markers are 3.46 nm and 4.82 nm respectively) (a) and height cross-section (b). The dash lines in the cross-section graph shows the border of two different markers in the AFM image.

3-3 Preparation of Buffer Solutions

Two kinds of buffer solutions were used for the pH sensing experiments: 1) constant and 2) non-constant ionic strength buffer.

1) Macllavanie buffer[164] usually used as a constant ionic strength buffer, which covers the range of pH from 2 to 8. To cover all the range of pH up to 12, the Britton–Robinson buffer is usually used[165]. To prepare this buffer solution, acetic acid, phosphoric acid, boric acid, sodium hydroxide and potassium chloride (all reagent grade) were used. Buffer solutions of different pH were prepared using various quantities of acetic acid, phosphoric acid, boric acid and sodium hydroxide to reach a specific pH value. For each solution, a quantity of potassium chloride was added to increase the ionic strength of the buffer solution to 1 M.
2) The ionic strength, I, of a solution as a function of the concentration of all ions present in that solution, could be calculated by:

$$I = \frac{1}{2} \sum C_i Z_i^2 \qquad (3\text{-}1)$$

where C_i is the concentration of ion i, Z_i is the charge of the ion and the sum is taken over all ions in the solution. Therefore, the amount of acid and base and salt in each pH to reach constant ionic

strength ($I = 1$ M) could be calculated. For example, for a buffer solution of pH=2.09, we used 0.558 g/L of sodium hydroxide, 2.234 g/L acetic acid, 3.647 g/L of phosphoric acid and 2.301 g/L of boric acid and added 73.064 g/L of potassium chloride to reach1 M ionic strength.

3-4 Conductivity Measurement of SWCNTs

As said before, the single-walled carbon nanotube is an interesting nanomaterial because of its unique electrical, mechanical, and optical properties. SWCNTs have been studied with all types of characterization tools[148, 149]. In this section, we focused on the film conductivity of SWCNTs, which arises from the carrier transport along the cylindrical sidewall and hopping from one tube to another [150]. Since the conductivity of SWCNTs is dependent on charge carriers, the conductivity of SWCNTs is expected to change by reaction with redox dopants, which can induce hole doping or electron doping into the SWCNTs network, which shifts the Fermi level to a lower or upper energy position, respectively. For example, a treatment of SWCNTs with nitric acid[151, 152], thionyl chloride[151, 152] or sulfuric acid[153] was shown to increase the electrical conductivity, a change ascribed to a hole doping of the SWCNTs network (i.e. a lowering of the nanotube Fermi level) [154].

In this thesis, a four-probe setup was used to measure the conductivity of thin films of platinum decorated SWCNTs. This test was to confirm the doping of SWCNTs via the redox action of the Pt/PtO couple at different pH. The reason of using a four-probe measurement instead of two- probe measurement is explained next.

3-4-1 Sheet Resistance Measurements via the Four-Probe Method

In two probe setup, the Voltage (V) is applied across a device containing SWCNTs and the devices responses (current, I) include contributions from contact resistances. The contact resistance is attributed to the contacting interfaces between the SWCNTs and the metal probe (Figure 3.5). According to the ohm's law, $V = I\,R_{(total)}$, the resistance could be calculated from the applied Voltage and measured current. The total resistance in a two-probe measurement (Figure 3.5 (a)) includes the contact resistances, which are measured along with the exact sample resistance ($\Delta V = I\,R_{(total)} = I\,(R_{c\,1} + R_{sample} + R_{c\,2})$, when the sample resistance is low.

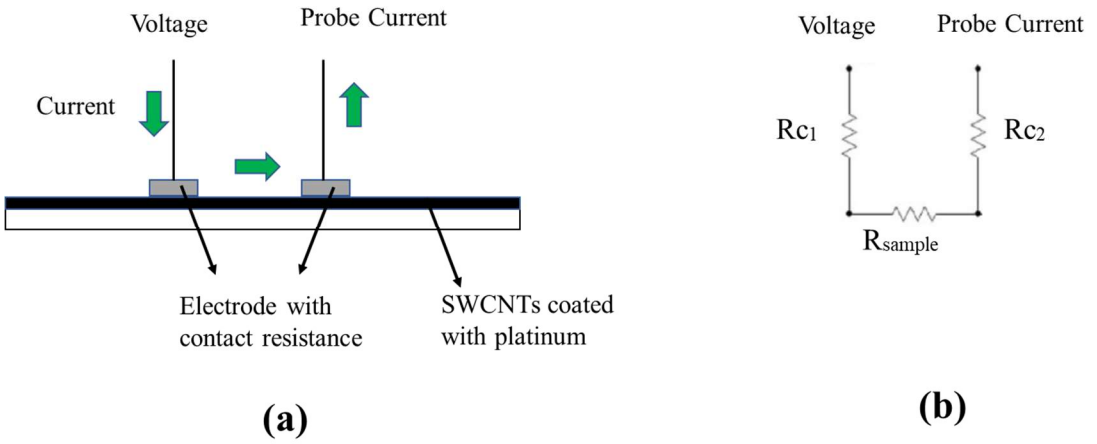

Figure 3.5. (a) Two-probe electrode configuration with platinum electrodes on a platinum coated SWCNTs film. (b) A typical two configuration represented by a simplified resistor network.

To avoid the issue with the contact resistances, we employ a four-probe method to interrogate electrical properties of a Platinum coated SWCNTs system, while allowed us to probe the doping of SWCNTs without the effect of the contact resistance. Figure 3.6 (a) shows a schematic of the four-probe setup and Figure 3.6 (b) shows a simplified resistor network of the equivalent circuit. R_{12}, R_{23}, and R_{34} are the film resistances between probes 1 and 2, 2 and 3, and 3 and 4, respectively. $R_{c\,1}$, $R_{c\,2}$, $R_{c\,3}$ and $R_{c\,4}$ are the contact resistances between film and probes 1, 2, 3 and 4, respectively. The buffer that is used in 4–probe setup consists of Voltage buffers, as shown in Figure 3.7. There are two important rules in these buffers: 1) No current into the input and 2) the input Voltage equals the output Voltage.

According to these rules of known current, I, flows from probe 1 to 4 through the outer contacts and the film. The total Voltage, V_{14}, required to drive this current, depends on both the outer contact resistances and the film resistance.

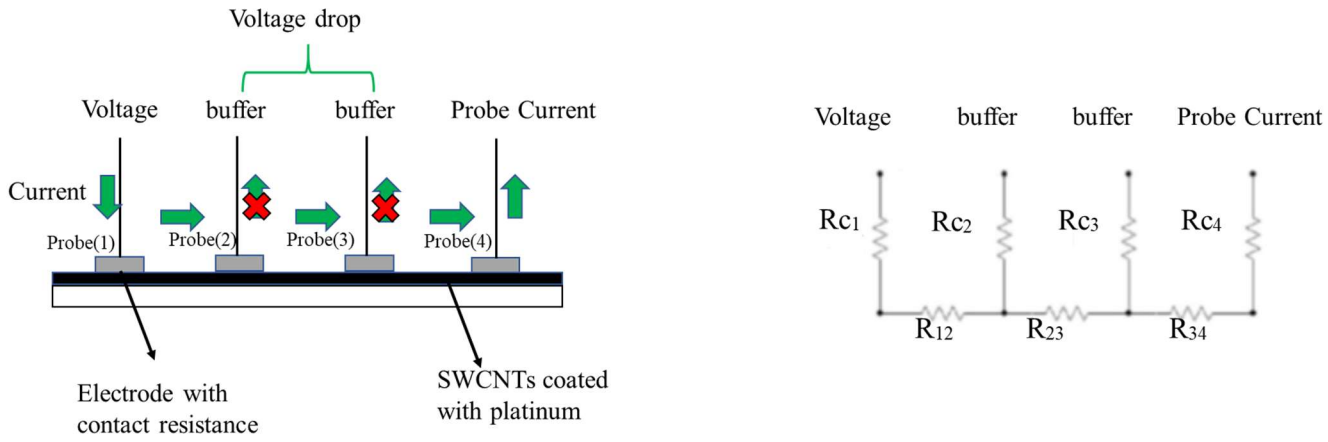

Figure 3.6. (a) Four-probe electrode configuration with Platinum electrodes and a Platinum coated SWCNTs film. (b) A typical four configuration represented by a simplified resistor network.

According to the Ohm's law, ($V_{14} = I\,R_{(total)}$), where $R_{(total)}$ is the total resistance of the film plus two contact barriers, $R_{(total)} = R_{c\,1} + R_{12} + R_{23} + R_{34} + R_{c\,4}$. In the four-probe method, the Voltage difference between probes 2 and 3, V_{23}, is measured using the buffers, which do not allow current to flow across $R_{c\,2}$ nor $R_{c\,3}$ and force all of the current to pass through the film. Therefore, the Voltage drops across these contact resistances is zero and V_{23} is directly related to the Voltage drop across R_{23}. Because the current passing through R_{23} is I (according to the Ohm's law), the film resistance could be measured in terms of $R_{23} = IV_{23}$, which avoids the presence of contact resistance[155].

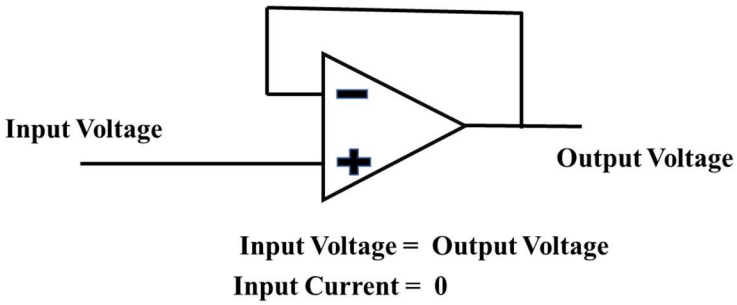

Figure 3.7. Schematic of Voltage buffer

3-4-2 Sheet Resistance Measurement

The film SWCNTs decorated with nanoparticles of platinum (12x3 mm piece) was deposited onto an aminosilanized quartz substrate via the method mentioned above. Six electrodes composed of Titanium(Ti) /gold(Au) (30/20 nm) were deposited using e-beam evaporation and a shadow mask. Kapton tape was used to cover the electrodes and the film, with only a section of the film between two inner electrodes exposed. The sample was submerged in an ionic constant buffer solution of a particular pH value for 20 minutes and film resistance was measured. The sample was then washed by rinsing and submerging in deionized water for 10 minutes.

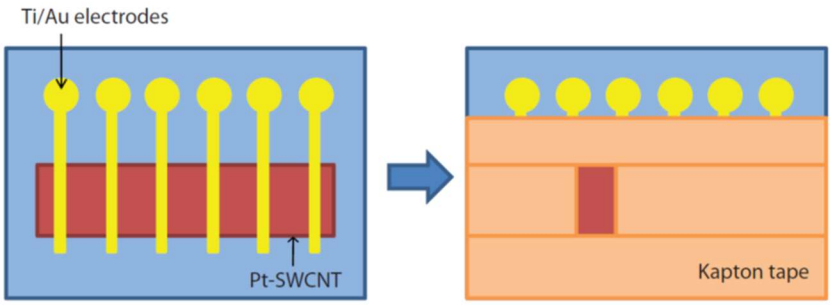

Figure 3.8. Schematic of electrical measurement sample of Pt_N-SWCNT before (left) and after (right) covering electrodes and selected films with Kapton tape.

3-4-3 Characteristics of 4-Probe Setup

The resistance of the films was measured using a four probe electrical set up: A DC Voltage (± 0.25 V) was applied between the outer electrodes and the current and the Voltage drop between the inner electrodes were measured using a homemade electronics and a National Instruments DAQ (USB-6211). The film resistance was obtained by taking a linear fit of the current vs. inner Voltage drop.

3- 5 Characterization of SWCNTs by Transmission Electron Microscopy (TEM)

TEM is widely used to visualize nanomaterials, especially carbon nanotube and nanoparticles, and it is also used to determine the diameter of carbon nanotubes. By directly measuring the distance in a TEM image, the parameters can be extracted. There are many factors like the defocus value and the size of the objective aperture that could change the appearance of the TEM images. The important part of visualization of carbon nanotube with TEM is the ability to see the material deposited on the surface, which provides information about the size and shape of that material[166, 167]. In this thesis, the size of the metal nanoparticles were measured by TEM technique and an example is shown in Figure 3.9.

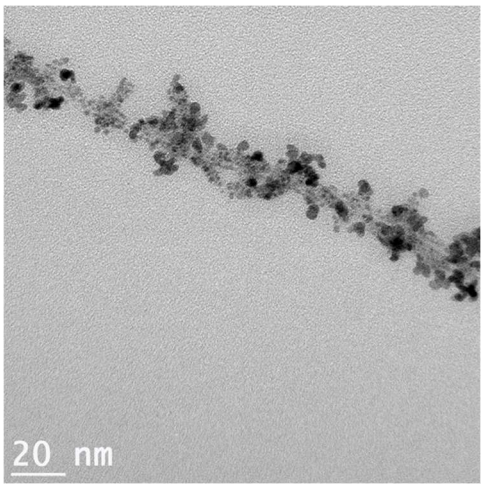

Figure 3.9. TEM image of an SWNT decorated with nanoparticles of platinum.

3-5-1 Characteristics of TEM instrument

The TEM images were taken by JEOL 2100-F FEG-TEM which operated at 200 kV in the bright field mode. TEM samples were prepared by ultrasonication of aqueous solutions of the metal decorated SWCNTs for 30 min. A drop of the suspension was deposited on a standard TEM grid covered with a lacey carbon film and dried in air. These characterizations were performed at Centre de Caractérisation Microscopique des Matériaux $(CM)^2$ from École Polytechnique de Montréal.

3-6 Characterization by Atomic Force Microscopy (AFM)

AFM is the most widely used instrument among scanning probe microscopy (SPM) techniques because of the accurate three-dimensional imaging of samples with quasi-atomic resolution, low cost, short time acquisition and nondestructive technique. Among the many possible characterizations of carbon nanotube with the AFM, we have determined the diameter distribution and evaluated if the nanotubes are isolated and measured their length. We have also used the AFM technique to define the thickness of SWCNTs films and the distribution of SWCNTs on the silicon substrate (Figure 3.4).

3-6-1 Characteristics of AFM instrument

The AFM images were produced using a Dimension 3100 scanning probe microscope equipped with a Nanoscope IV controller and the system was operated in the non-contact mode.

3-7 Characteristics of Raman Spectrometer

Raman spectra were acquired using a Raman spectrometer (Renishaw, InVia) with two excitation wavelengths (λ_{ex} = 514 nm and 633 nm) and a maximum power of 150 μW μm^{-2}. Although the main region of interest is around the G-band (1450–1650 cm^{-1}), spectra were recorded from 100–3000 cm^{-1}. Acquisition times of 10–30 s was used to achieve a good signal to noise ratio. Raman measurements in a pH-controlled aqueous solution were performed using the liquid cell shown in Figure (3.10).

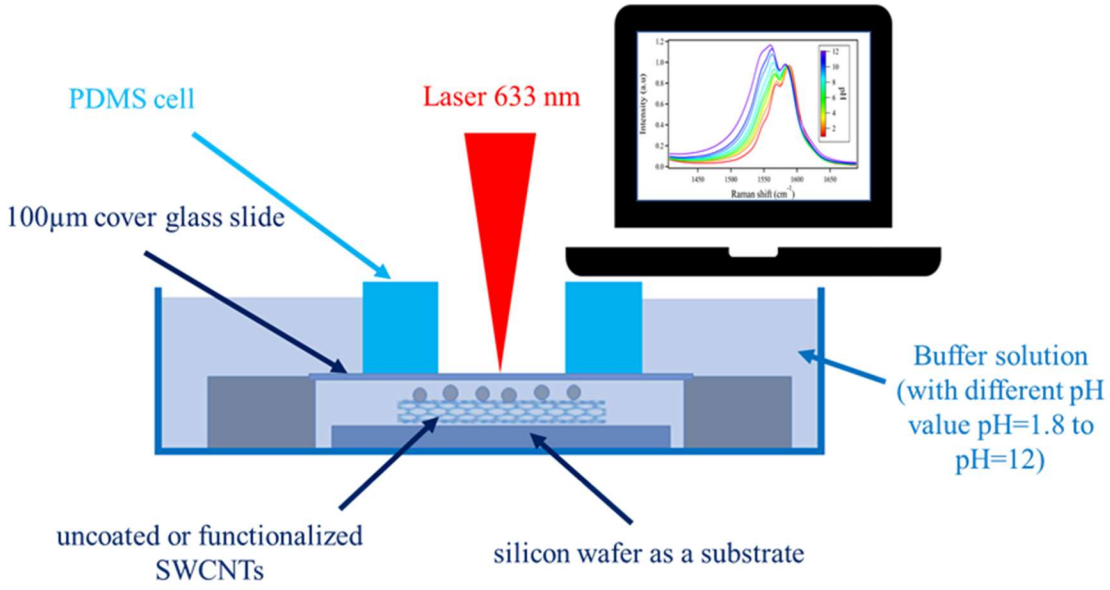

Figure 3.10. Schematic of the liquid cell for Raman spectroscopy. Raman spectra are collected at room temperature using a laser at a wavelength of 633 nm.

All three components of the main peak of Raman measurements (G-bands) in Chapter 4 (Single walled carbon nanotubes-based Raman pH sensor) were fitted with a Voigt function. As an example, the mathematical of a deconvolution of the G-bands in pH=2.45 for the platinum evaporated SWCNTs is reported In the Figure 3.11, and the result of this deconvolution is presented in Table 3.1.

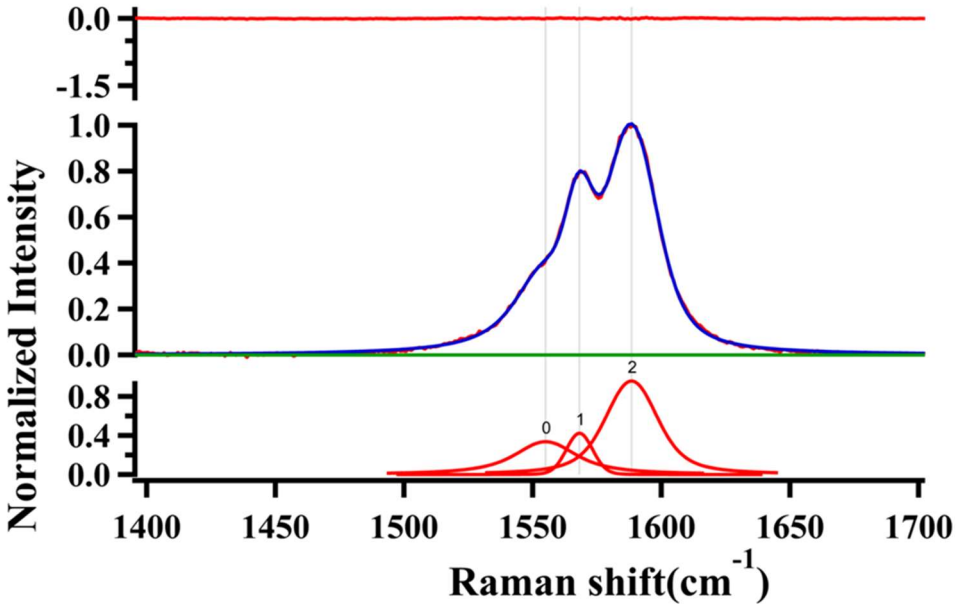

Figure 3.11. Example of the mathematical deconvolution of the Raman spectrum of a thin film of Pt-coated SWCNT at pH=2.45 (blue line). The red curves are the Voigt functions used to fit the three peak components.

Table 3.1. Example of peak deconvolution (Voigt function) data of the Raman spectrum of Pt-coated SWCNTs at pH=2.45

Voigt function	Location(cm^{-1})	Height	Width	Area	FWHM* (cm^{-1})
Peak0**	1555	1.113	0.138	14.281	28.58
Peak1***	1568.2	0.4524	0.144	5.5774	12.01
Peak2****	1588.4	1.687	0.099	30.185	23.91

* Full width at half maximum; ** G_f mode; *** G^- mode; **** G^+ mode

In chapter 5 (pH dependency of graphene in contact with Pt), the Raman spectra were acquired using the Renishaw, InVia and also on a custom built spectrometer equipped with different laser excitation lines (488, 514, 532, and 633 nm) and a nitrogen-cooled silicon detector array ((JY Symphony) mounted on a Jobin-Yvon Triax iHR550 spectrometer (grating 1,800 g·mm blazed at 630 nm) with a precision of 0.2 cm^{-1}. The laser power was kept near 1000 μW on the sample and

the signal was collected near-diffraction limited resolution using a 50× objective with a numerical aperture of 0.5. Spectra in solutions are acquired *in-situ* using the setup described above.

In chapter 5, the two main peaks of Raman measurements (G-bands and D-band) were fitted with a Lorentzian function.

pH Responsive Platinum-Coated Single-Walled Carbon Nanotube Optical Sensor with Internal Reference

Fatemeh Shoghi, Suraj Mal, Monique Tie, Antonella Badia and Richard Martel*

Département de chimie, Université de Montréal, Montréal, Québec H3C 3J7, Canada

Authors' Contribution: F. Shoghi has performed the synthesis and the preparation of the samples and she has characterized, analyzed, and interpreted the data. F. Shoghi drafted the manuscript and revised it accordingly. S. Mal carried out the synthesis of the metallic SWCNTs decorated with nanoparticles of platinum, palladium and ruthenium. M. Tie did the electrical resistance measurements. A. Badia provided advice during the course of these experiments and revised the manuscript. R. Martel designed the experiments, revised the manuscript critically and approved the final version.

Chapter 4: pH Responsive Platinum-Coated Single-Walled Carbon Nanotube Optical Sensor with Internal Reference

Measuring proton [H^+] concentrations in chemical or biological environments is central to a wide range of applications, such as medical diagnostics[19, 20, 168], environmental analysis[169-171] and industrial processing[172, 173]. pH sensing methods have evolved over the years around potentiometric techniques in which the sensing electrode is made of either a glass electrode or an Ion-Sensitive Field-Effect Transistor (ISFET) for potential measurements in solution. Modern pH sensors are robust, accurate and low cost, but they are limited by the macroscopic sizes of the electrodes and by errors associated with the contamination of the small electrode liquid junctions[27, 174]. As a result of these limitations, electrodeless measurements based on optical techniques such as photoluminescence spectroscopy[175-177] and UV-Vis absorption[178-180]have raised interest following clear demonstrations of high precision pH measurements on the micrometer scale. The optical responses are, however, prone to oxidation or photobleaching and generally provide non-specific signals that can be mixed with other signals (contaminants, biomaterials, support, etc.). Furthermore, optical pH sensors are generally poorly referenced and their performance depends on the concentration of the analyte, which is typically unknown in complex media. By relying on the relative Raman intensity of pH sensitive molecules in the protonated and deprotonated states, Surface Enhanced Raman Spectroscopy (SERS) has been applied to pH sensing to gain unambiguous signals from active molecules, thanks to the vibrational fingerprints of these pH reporters. The pH measurements remain, however, semi-quantitative due to the local nature of the hotspots, which induces large distributions of the electric field depending on the interparticle distance and geometrical configuration of the plasmonic response near the reporting molecules[181]. These hurdles have so far challenged the development of remote optical pH sensors that are properly referenced. Therefore, finding the specific materials and proper optical technique are important to design the remote optical pH sensors.

In this work, we present an optical pH sensor based on the Raman response of metallic Single-Walled Carbon Nanotubes (SWCNTs) functionalized with a transition metal nanoparticles.

SWCNTs have been chosen because of their huge surface-to-volume ratio and their strong Raman activity[182], making them well suited to the development of sensors for biology and medicine[183-186]. The Raman G-band of SWCNTs is of particular interest for sensor applications as it provides significant softening (red-shift) or stiffening (blue shift) of the G-band with nanotube doping[138, 147, 187-189].

Here, we report that the Raman signal of nanoparticles of Pt on SWCNTs (Pt_N-SWCNTs) is best adapted for pH sensing and that it can be used for making referenced measurements of the local pH over a wide range (pH = 0–12) with a best accuracy of ±500 mpH units. The signal of Pt_N-SWCNTs supported on an oxide surface in solution consists of a reversible and reproducible transformation of the Raman G-band upon changes in the solution pH. The Raman spectral shifts and intensities are linear with pH, which is ascribed to charge transfer doping of the SWCNTs via the Pt/PtO redox pair according to the equilibrium reaction: $PtO + 2H^+ + 2e^-(SWCNT) \rightleftharpoons Pt + H_2O$. This study explores the influence of different transition metals (Pt, Ru and Pd), of semiconducting *vs.* metallic SWCNTs and of the supporting substrate on such pH sensing scheme. The results demonstrate that the Raman signal of metallic nanotubes can be used to reference the electrochemical potential of the solution. This optical nanotube-based pH sensor consisting of a referenced nanotube redox reporter is discussed as the nanoscale optical analogue of a conventional pH sensor.

4-1 Materials and Methods

4-1-1 Materials and Instruments.

SWCNTs with a diameter distribution of 1.1–1.5 nm were produced by laser ablation [158]. Chloroplatinic acid hydrate ($H_2PtCl_6 \cdot xH_2O$, ≥99.9%) and sodium borohydride ($NaBH_4$, 98%) were from Sigma-Aldrich. Reagent grade nitric acid (HNO_3), sulfuric acid (H_2SO_4), acetic acid, phosphoric acid, boric acid, sodium hydroxide (NaOH), hydrochloric acid (HCl), potassium chloride (KCl), acetone, and isopropyl alcohol were used as received from Fisher Scientific. Raman spectra were acquired using a Raman spectrometer (Renishaw, InVia) with two excitation wavelengths (λ_{ex} = 514 nm and 633 nm). Raman measurements in a pH-controlled aqueous

solution were performed using the liquid cell shown in Figure 3.6 (more details about Raman measurement and instrument in chapter 3). The size of the platinum nanoparticles was estimated using a Transmission Electron Microscope (TEM). The preparation of TEM samples, characteristic of TEM instrument and also buffer solution were explained in chapter 3.

The pH meter (Education Series EL20 Benchtop METTLER TOLEDO) was calibrated with three standard buffer solutions (pH=4.01, pH=7.00, and pH=10.00).

4-1-2 Preparation of Solid-Supported SWCNTs

The SWCNTs were purified and thin films of SWCNTs were prepared by vacuum filtration of an aqueous dispersion of SWCNTs through a nitrocellulose membrane and then transferred to a patterned substrate consisting of an oxidized silicon wafer (Si/SiO_2, thickness = 300 nm). More details about purification, the substrate patterning and functionalization are given in chapter 3.

4-1-3 Synthesis of Pt-SWCNTs

Direct metal deposition to form metal-coated SWCNTs was performed by an electron beam (e-beam) evaporator (more details in chapter 3). The method allows to deposit about 10 nm of platinum on a mat of entangled SWCNTs supported on the oxidized silicon wafer. The resulting sample is referred to in the main text as Pt-SWCNT.

4-1-4 Synthesis of Pt_N-SWCNTs.

The second method involves a one pot preparation from platinum nanoparticles grown in solution using $H_2PtCl_6 \cdot xH_2O$ and sodium borohydride as the reducing agent, giving a sample labeled as Pt_N-SWCNTs (more details about synthesis of Pt_N-SWCNTs in chapter 3)

4-1-5 Synthesis of Pt_N-m-SWCNTs, Pd_N-m-SWCNTs and Ru_N-m-SWCNTs

A third method was devised to prepare nanoparticles of various metals (Platinum(Pt), Palladium (Pd) and Ruthenium(Ru)) attached to metallic (sorted) SWCNTs (Isonanotube-M 95%) in an aqueous solution with sodium-dodecyl sulfate (SDS) and giving samples labeled as Pt_N-SWCNTs, Pd_N-SWCNTs and Ru_N-SWCNTs (more detailed about synthesis in chapter 3) . TEM images of the products of the synthesis of Pt_N-SWCNTs, Pd_N-SWCNTs and Ru_N-SWCNTs are shown in

Figure 4.12 (Supporting Information section 4-4). The image shows extensive and uniform coverage of nanoparticle distributed along the SWCNTs.

4-1-6 Electrical Measurements of Pt_N-SWCNTs.

A 12x3 mm piece of Pt_N-SWCNTs was deposited onto an amino-silanized quartz substrate via the method mentioned above. Six electrodes composed of Ti/Au (30/20 nm) were deposited using e-beam evaporation and a shadow mask (Figure 3.5 in chapter 3). Resistance was measured using a four probe electrical set up: dc Voltages (± 0.25 V) was applied between the outer electrodes and the current and the Voltage drop between the inner electrodes were measured (more details in chapter 3). Film resistance was obtained by taking a linear fit of the current vs. inner Voltage drop.

4-2 Results and Discussion

4-2-1 The Raman Response of Pt-SWCNTs with pH.

The Raman response of Pt-SWCNTs prepared by e-beam deposition of Pt on a thin film of laser ablated SWCNTs (diameter range 1.1-1.5 nm)[158] was first benchmark with the response of films similarly treated without Pt. Figure 1 presents the G-band region (1450–1650 cm^{-1}) of the Raman spectra of both samples in buffer solutions of pH ranging from 1.80 to 11.80. For these sets of experiments, an excitation wavelength of λ_{ex} = 632 nm was selected to specifically target the Raman resonance of the metallic nanotubes in our sample. While semiconducting SWCNTs are present, these species are not in resonance at 632 nm due to the diameter distribution, and hence their Raman signal does not appear in the spectra[104]. The Raman spectra of both samples undergo changes as a function of the solution pH, but the overall spectral response of the Pt-SWCNT sample (Figure 4.1(a)) is significantly more pronounced than that of the SWCNTs. As explained below, this result is central to our study.

More details about the spectral transformations with pH are garnered from each of the three components of the G-band region. The first peak at the highest Raman shift, labeled G+ mode, is clearly the least affected by pH. This mode is associated with the TO phonon branch with displacements of atoms perpendicular to the nanotube axis. Because its position and intensity vary little with pH, the G+ mode can serve as a spectral reference point for normalization. By contrast,

the second and third peaks located below the G+ mode evolve with pH. These components of the Raman signal are the most interesting for sensing and discussed next using the responses shown in Figure 4.1(a). The peak labeled G- mode, which is right below the G+ mode, is ascribed to LO phonons which is related to the vibrations of carbon atoms along the axis of the nanotube. This mode has been reported to undergo a blue shift upon doping, a behavior ascribed to strong electron–phonon coupling in SWCNTs, which affects the lattice parameters (i.e., C-C bond length) and renormalizes the phonon energy [190]Because of its peculiar lineshape (broad and asymmetrical), the low energy peak at around 1548 cm^{-1} is called the Fano mode (labeled here as G_f). Due to a Kohn anomaly in the nanotube band structure, the position and shape of the G_f mode depend strongly on charge density; mode broadening and softening are maximal when the doping state of the SWCNT is near charge neutrality [125, 136, 142, 147, 190-192]As discussed below, these important characteristics of the G_f mode can be used to reference the potential of the solution.

In Figure 1a, both the shift of the G_- mode and the asymmetric broadening of the G_f mode of Pt-SWCNTs are clear signatures of a doping process in which the pH of the solution consistently shifts the Fermi level of the metallic SWCNTs. On the basis of the trends observed, i.e., red shifting of the G_- mode across the entire pH range of 1.80 to 11.80 investigated and maximal broadening of the G_f mode at pH 12, we deduce that the SWCNTs are p-doped at pH = ~1 and quasi undoped at pH = ~12. In comparison with previous work, the Raman shifts observed here are higher than those reported in doping studies of SWCNT devices using gate Voltages [147]and the behavior in Figure 4.1(a) is comparable to that measured for Raman spectroelectrochemistry of metallic SWCNTs.

A qualitative comparison of the pH response of metallic SWCNTs prepared with and without Pt shows that the local environment surrounding the SWCNTs is a key parameter controlling the doping process. That is, the gradual and uniform transformation of the G-band of Pt-SWCNTs (Figure 4.1(a)) over the full pH range contrasts with the almost unperturbed Raman spectrum of the uncoated SWCNTs in the pH range of 1–8 (Figure 4.1(b)). To quantify the different responses of each sample, Figure 4.2 reports the results of a deconvolution of the G-bands at each pH value (peak fitting details are provided in the chapter 3). There are several significant observations. First, the Raman shifts of the G- and G_f modes and the normalized integrated intensity of the G- mode relative to the G+ mode, hereafter labeled I(G-/G+), shows nearly linear dependencies with pH.

Compared to the SWCNTs, the slopes of the G-–pH and G_f–pH plots are steeper for the Pt-coated SWCNTs (i.e., G_f mode gives -0.89 ± 0.02 cm^{-1} /pH unit vs. -0.33 ± 0.03 cm^{-1}/pH unit); there is a three-fold larger change for every incremental increase of the pH unit. For both samples, the G- and G_f modes red shift with pH and the I(G-/G+) also increases with pH. Surprisingly, both samples give similar fitting parameters at pH = ~12, meaning that SWCNTs are roughly at the same doping state, i.e., near the charge neutrality. Last, pH-induced doping takes place in both cases, but the doping is much stronger for metallic SWCNTs in contact with Pt.

The different pH dependencies of the G-band between the two samples are rationalized by the reduction-oxidation (redox) reactions occurring in the environment around the SWCNT film. According to the Marcus-Gerischer theory[193, 194], charge transfer on solid electrodes can be estimated using the overlap integral between the occupied/unoccupied states at the valence and conduction band edges of the electrodes and the unoccupied/occupied states of the redox system at the origin of hole (p-type) or electron (n-type) doping. In electrochemistry language, charge transfer is mainly driven by the difference between the electrochemical potentials, E_{redox}, of the redox couple and internal potential, E_f, of the SWCNTs. In solution, the reaction proceeds until equilibrium is reached between the two systems (i.e., $E_{redox} = E_f$), effectively resulting in the electrochemical doping of the SWCNTs. As previously proposed by our team to explain the unintentional doping of SWCNT transistor devices, air doping can be ascribed to the O_2/H_2O redox pair according to the well-known reaction: $O_{2(aq)} + 4H^+_{(aq)} + 4e^-(SWCNT) \rightleftharpoons 2H_2O_{(l)}$. [195, 196.]

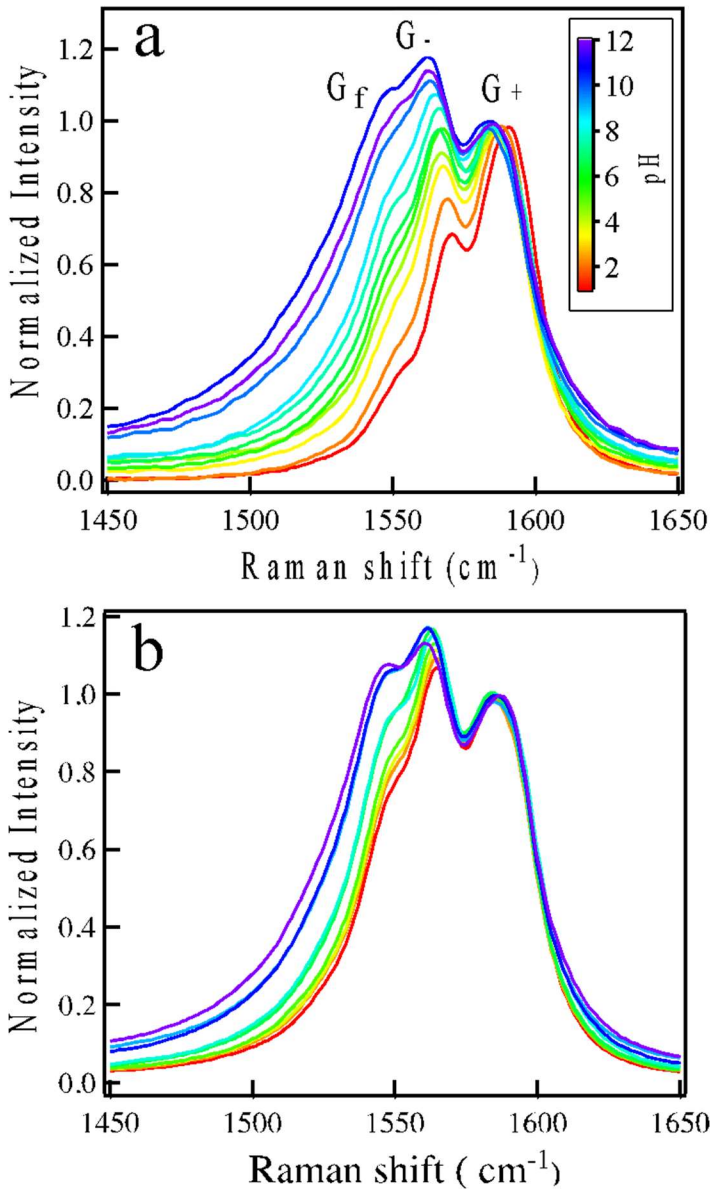

Figure 4.1. Comparison of the Raman spectra of Si/SiO2-supported films of (a) Pt-SWCNTs and (b) purified SWCNTs without Pt. The spectra were recorded in buffer solutions of constant ionic strength (1 M) at unitary pH increments between 1.80 (red) and 11.80 (blue) (from red to blue, pH = 1.80, 2.50, 3.60, 4.30, 5.40, 6.10, 7.10, 8.50, 9.20, 10.40, and 11.80). The intensity is normalized relative to the G+ mode maximum intensity.

For this redox couple, a fundamental expression of the potential under equilibrium conditions is given by the Nernst equation:

$$E_{O_2/H_2O} = 1.229 + \frac{0.0592}{4}(pO_2) - 0.059 \cdot \text{pH}$$

$$E_{O_2/H_2O} = 1.229 + \frac{0.0592}{4}(PO_2) - 0.0592\,\text{pH} \quad \text{or} \quad E_{O_2/H_2O} = 1.226 - 0.059 \cdot \text{pH} \quad (4\text{-}1)$$

where pO$_2$ = 0.65 bar is the oxygen pressure, which is equivalent to an oxygen concentration of 8.26 mg/L, under the experimental conditions used here. E_{O_2/H_2O} is expressed in Volt in eq 4-1. In the context of solids, the potential is more conveniently defined in terms of energy levels (in eV) with respect to the vacuum level using the expression:

$$E_{abs,O_2/H_2O} = -4.44 - 1.229 + E_{O_2/H_2O} \text{ or } E_{abs,O_2/H_2O} = -5.669 + 0.059 \cdot \text{pH} \quad (4\text{-}2)$$

Hence, depending on the pH of the solution, the energy level or Fermi energy lies between -5.61 eV (pH=1) and -4.95 eV (pH=12) (See Figure 4.3).

Because the valence band of small diameter semiconducting SWCNTs is roughly located between -5.3 eV and -5.7 eV, which is close to the redox potential of O$_2$/H$_2$O in acidic solutions (Figure 4.3), electrons can transfer from the SWCNTs to the solution, yielding p-doping in air[196]. The presence of finite energy states of metallic SWCNTs provides significant charging for ensuring energy level alignments with the absolute O$_2$/H$_2$O redox system at every pH value between 1 and 12. However, our experiments with uncoated SWCNTs (Figure 4.1(b)) show only small shifts of the G- and G$_f$ modes, indicating little or no charge transfer with pH. This sluggish pH dependency is ascribed to exceedingly slow kinetics at the surface of the SWCNTs for oxygen oxidation/reduction, i.e., non-Nernstian behavior. Namely, charge transfer to aqueous oxygen produces unstable intermediates on the surface of the SWCNTs, which cannot be easily anchored to the surface of the SWCNT, and hence, they can move back to the solution after transfer, yielding only partial reaction (4 electrons in total are required for the equilibrium). In other words, the SWCNTs have self-passivated surfaces and the oxidized form is poorly stable, which is bad chemically for ensuring the equilibrium of the O$_2$/H$_2$O redox system. As discussed below, a Pt coating provides different kinetics in this respect because the Pt/PtO redox pair can produce stable reduction/oxidation states while direct contact enables free charge transfer to the metallic

SWCNTs. In effect, the platinum nanoparticles provide sites for the strong chemisorption of oxygen, thereby making the splitting of aqueous O_2 more efficient than on uncoated SWCNTs.

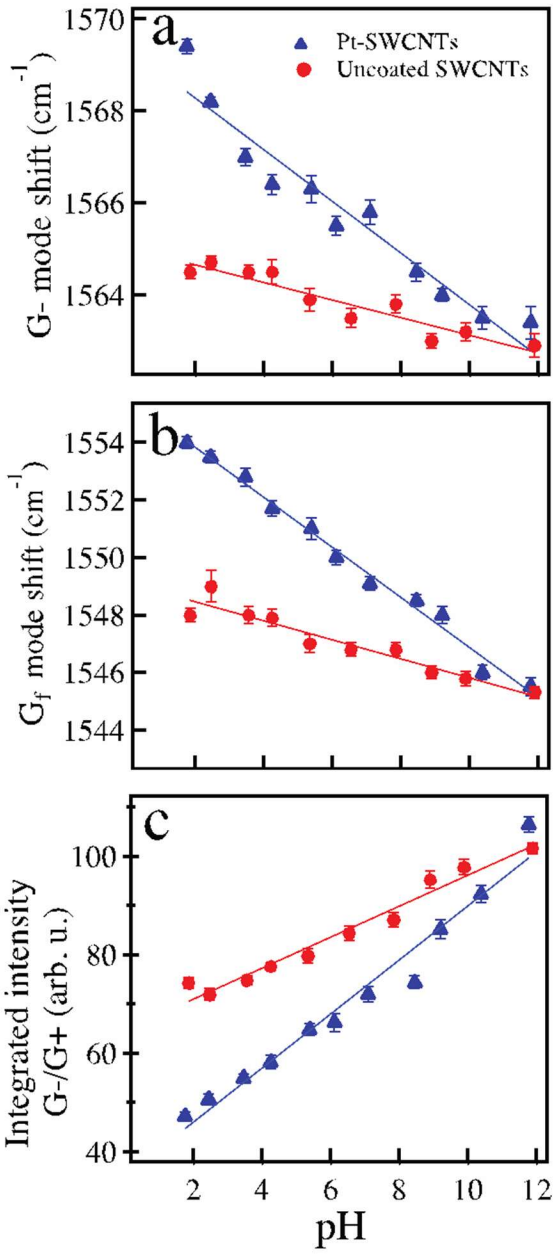

Figure 4.2. Spectral changes for thin films of SWCNTs (red, ●) and Pt-coated SWCNTs (blue, ▲) as a function of pH obtained using constant ionic strength buffers (1 M). Energy shifts of the G- mode (a) and G_f mode (b) and normalized integrated intensity of the G- mode relative to G+ mode (c). Correlation coefficients are: -0.97 (blue) and -0.94 (red) in (a), -0.99 (blue) and -0.95 (red) in (b), and 0.98 (blue and red) in (c).

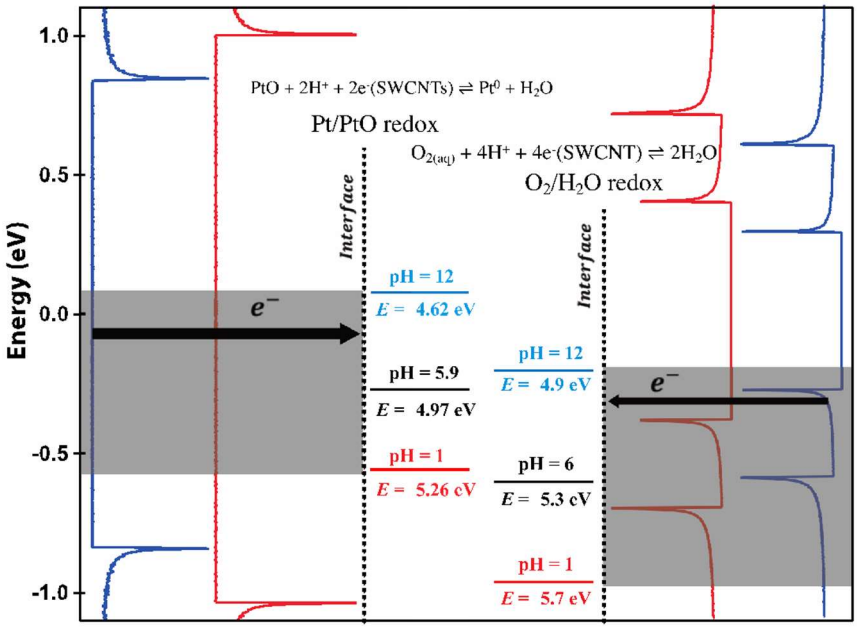

Figure 4.3. Energy level diagrams of the Pt/PtO (left) and O_2/H_2O (right) redox couples compared to the density of states (DOS) of metallic (left) and semiconducting (right) carbon nanotubes of small (blue) and large (red) diameters in our sample (between 1.1 nm and 1.5 nm). The arrow indicates the direction of the charge transfer reaction. The energy scale is based on a work function of 4.7 eV for the SWCNTs.

Many studies have demonstrated that the platinum surface in air contains a mixture of Pt and PtO[197, 198]. The Pt/PtO redox couple could therefore compete with the O_2/H_2O reduction reaction discussed above according to: $PtO + 2H^+ + 2e^-(SWCNTs) \rightleftharpoons Pt^0 + H_2O$. The redox potential of the Pt-SWCNT system is therefore given by: $E_{Pt/PtO} = 0.88 - 0.059 \cdot pH$, where $E_{Pt/PtO}$ is in Volt . The energy level (in eV) with respect to the vacuum level is[199]:

$$E_{abs,Pt/PtO} = -4.44 - 0.88 + 0.059 \cdot pH \qquad (4\text{-}3)$$

In Figure 4.3, the energies of both redox systems, O_2/H_2O and Pt/PtO, at different pH values are presented with respect to the vacuum level and serve as a theoretical standpoint for the discussion of the pH dependencies. Using a work function of 4.7 eV for the SWCNTs[200], the model can be used to predict the equilibrium position of the potential with the pH of the solution. In an acidic solution of pH 1, the diagram predicts, for example, that the energy level of the Pt/PtO redox pair

lies between the first and second valence band edges of semiconducting SWCNTs, while it is deeper below the second band edge for the O_2/H_2O redox pair. In a basic solution of pH 12, the energy level of Pt/PtO redox pair is near midgap, whereas it is next to the valence band for the O_2/H_2O redox pair.

This model provides an interesting comparison with the pH-induced spectral changes presented in Figures 4.1 and 4.2. The model predicts that the Pt-SWCNT system should drive at pH = 12 the nanotube Fermi level towards the midgap, which is consistent with the broad and red shifted spectrum in Figure 4.1(a). Unexpectedly, the model predicts a potential difference of about 0.3 eV with uncoated SWCNTs, but the results (Figure 4.1(b)) show instead an undoped situation at pH = 12 for the latter, i.e., the equilibrium should favor p-doping whereas the Raman spectrum indicates midgap alignment. We hypothesize that the inconsistency between the model and the experimental findings on uncoated SWCNTs is probably due to slow kinetics, giving out-of-equilibrium conditions, which implies that the SWCNT is a poor redox system. That is, uncoated SWCNTs are self-passivated, hence, their surfaces cannot stabilize intermediate species of the O_2/H_2O equilibrium reaction, whose presence is required to stabilize the positive charges (p-dopant) on the nanotubes.

4-2-2 Effect of the Ionic Strength of the Buffer Solution.

In the experiments presented in Figure 1, the ionic strength (*I*) of the buffer solutions was kept constant at 1 M [45]. To address the aforementioned discrepancy between the observed Raman shifts (Figure 4.2) and the model presented in Figure 4.3, we explored the effect of the ionic strength of the buffer solution on the resulting doping states of uncoated SWCNTs and Pt-SWCNT samples. Buffer solutions of different ionic strengths were prepared with the same ionic species for the different pH and the results are presented in Figure 4.4. The ionic strength does not impact significantly the pH response of the Pt-SWCNTs, as evidenced by the parallel slopes of the G- and G_f modes. However, when measured in buffer solutions where *I* is not constant, the Raman modes show shifts that are generally downshifted relative to that of the buffer solutions of constant *I*. As discussed above, the Raman shift of the G- mode indicates that charge transfer doping drives the Pt-SWCNTs response. Hence, this downshifting for a given pH is a clear indication of a significant doping change associated to charge screening from the ions in solution. The effect is more clearly illustrated using three solutions of fixed pH (3.54) but different ionic strength (I = 1, 0.5, and 0.1

M) (see insets of Figure 4.4). For a given pH, decreasing the ionic strength generally reduces the doping level, which is evidenced by a blue shift of the G- and G_f modes (insets of Figure 4.4(a,b)) with increasing *I*. The effect is also noted in the inset of Figure 4c by a general decrease of the integrated intensity with *I*.

Surprisingly, the effect of the ionic strength on the Raman shift of the G-band of the uncoated SWCNTs is very weak. Additionally, it is interesting to point out that a reduction of the ionic strength, i.e., lower screening, does shift the doping state towards the energy position predicted by the model. That is, the model in Figure 3 indicates that charge neutrality should be observed at pH of >12 and ~ 4.9 eV, ~ 4.6 eV for the uncoated SWCNTs and Pt-SWCNTs, respectively. The results in Figure 4 indicate that this is indeed the case but for a solution with I = 0.1 M. This surprising result demonstrates that the pH response is mostly driven by the Pt/PtO reaction and that the reaction at the SWCNT surface in the bare section has no or little effect on the final potential of the Pt-SWCNT system. Overall, all of the experiments on uncoated SWCNTs show a reduced pH response and no noticeable screening effects from the ions, which reinforces our conclusion that an uncoated SWCNT is a poor redox couple. Our investigation of the effects of additional parameters on pH sensing was therefore pursued with the Pt-coated SWCNT samples.

4-2-3 Raman Response from Semiconducting SWCNTs.

So far, all the experiments were carried out on metallic SWCNTs, thanks to strong resonance effects of the laser at a wavelength excitation of 633 nm, which selectively targets the metallic species in this laser ablation source (diameters of 1.1-1.5 nm)[158]. The Raman of semiconducting SWCNTs can be highlighted at different wavelength excitation, but the model prediction a poor overlap at basic pH between their DOS and the electrochemical window of the Pt/PtO system (Figure 4.3, right panel). As shown in the examples of the Raman spectra in Figure 4.11 (Supporting Information in section 4-4), the Pt-SWCNT film measured at 514 nm wavelength excitation, which resonantly excites the semiconducting species, show a consistent Raman response with no or little effect on changing pH. These results further support the model in which the overlap of the DOS with the electrochemical potential of the Pt/PtO system is key to explain the sensing behavior reported here.

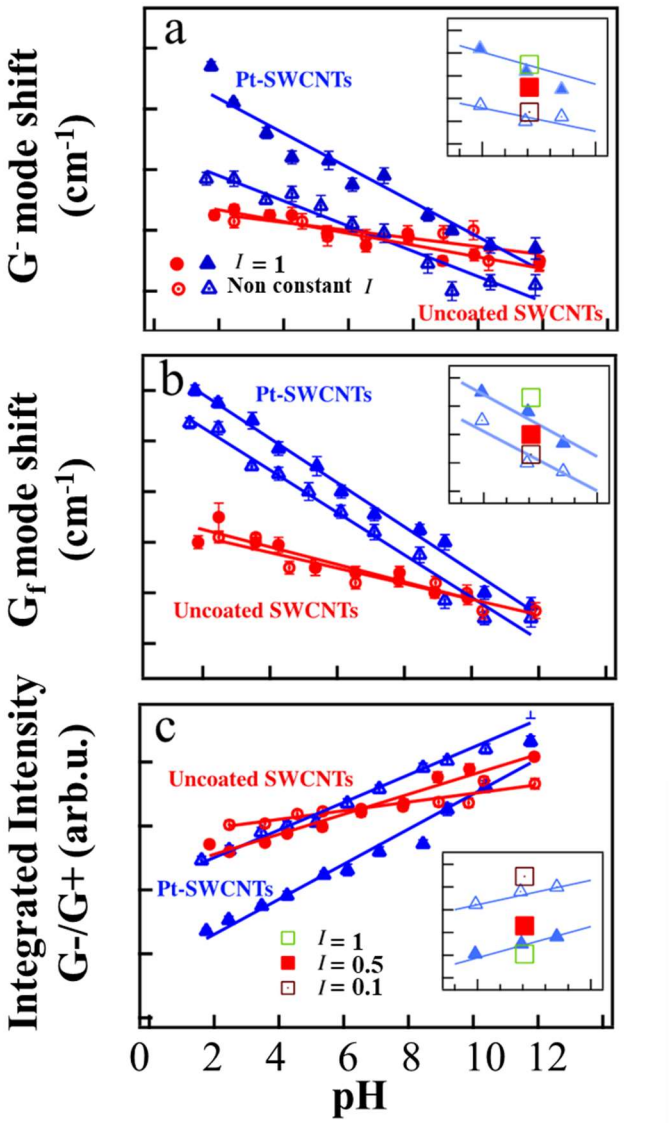

Figure 4.4. Raman shifts of the G- mode (a) and G_f (b) mode and the normalized integrated intensity of the G- mode relative to the G+ mode, I(G-/G+) (c) for uncoated SWCNTs (red) and Pt-SWCNTs (blue) in buffer solutions of different ionic strength. Insets show zooms of the results on Pt-SWCNT (blue) along with additional data at pH = 3.54 ± 0.01 and different ionic strengths (I = 1 M (green), 0.5 M (red) and 0.1 M (brown).

The presence of the SWCNT bandgap appears as an obstacle for sensing and the remaining of the study was therefore performed on metallic SWCNTs.

4-2-4 Sorted Metallic SWCNTs

With the understanding that pH sensing is due to the doping of metallic SWCNTs, we prepared nanoparticles of various metals on metallic SWCNT samples, which were previously sorted from a mixture of individualized SWCNTs in surfactant in water. A commercial source of SWCNTs from Raymor NanoIntegris was used for pure (>95%) metallic species, which is hereafter referred to as m-SWCNTs. For these experiments, syntheses of Pt_N-m-SWCNTs, Pd_N-m-SWCNTs and Ru_N-m-SWCNTs were carried out in one pot (see chapter3). Surprisingly, we found that the SWCNTs themselves can act as reducing agent in the conditions used, which makes the synthesis easy and versatile. As shown in the TEM images in Figure 4.12 (Supporting Information in section 4-4), the attached nanoparticles are uniformly distributed along the SWCNTs. The m-SWCNTs in that source have diameters in range between 1.2 nm to 1.7nm and the size of the nanoparticles ranges between 3-5 nm for Pt and Pd and 10-500 nm for Ru.

The Raman responses of each SWCNT-nanoparticle film in buffer solutions of constant ionic strength (1 M) at unitary pH increments between 1 and 12 are presented in Figure 4.5. The Pt_N-m-SWCNTs (Figure 4.5(a)) and uncoated m-SWCNTs (Figure 4.5(d)) are first used to draw a comparison with the results of Pt-SWCNTs and uncoated SWCNTs in Figure 1. The new results on sorted m-SWCNTs are fully consistent with the previous results: the shift of the G- mode is 10 cm^{-1} compared to 6 cm^{-1} for the Pt-SWCNTs and the slope is also steeper. The larger shift is probably related to the complete elimination of semiconducting SWCNTs in the sample. The uncoated m-SWCNTs do not show any changes with pH and this is also true for the radial breathing mode (RBM) region (Figure 4.14, Supporting Information in section4-4). Surprisingly, the RBM spectra of the Pt_N-m-SWCNTs in Figure 4.14(a) show a general loss of mode intensity between 160 cm^{-1} and 180 cm^{-1}, which is again consistent with doping[201] Because the Raman shift of the RBM is inversely proportional to the diameter, this trend indicates that larger diameter m-SWCNTs are more doped at given acidic pH compared to the smallest diameter nanotubes. This evidence of doping distribution across m-SWCNTs of different diameters suggests that a better sensitivity of the pH response is expected with m-SWCNTs sorted by diameter.

4-2-5 Comparison with Different Metals

While the response of the Pt_N-m-SWCNTs at pH = 12 shows undoped m-SWCNTs, the Pd_N-m-SWCNTs and Ru_N-m-SWCNTs are similar at basic pH, but their general behaviors vs. reducing pH are different. Fits to the pH responses are reported in Figure 4.13 (Supporting Information in section 4-4). The slopes of the G- mode shift vs. pH is negative for all metals, but the shifts are much smaller than for the Pt_N-m-SWCNTs. In addition, the G- mode intensity decreases with pH for both Pd and Ru, while it increases for the Pt_N-m-SWCNT. These results indicate that the Fermi level alignments of both Pd/PdO and Ru/RuO redox couples are less favorable for maximum Raman response in pH solutions, which is somewhat consistent with up-shifted potential-pH diagrams compared to what is shown in Figure 4.3 for Pt/PtO. We speculate that the work function of Pt, which is high (i.e. ϕ (Pt) > ϕ (Pd) ~ ϕ (Ru)), helps to drive a strong shift of E_F relative to the midgap state of the m-SWCNTs, an initial condition that is required for getting a maximal Raman response to pH. While a pH dependency is still visible for both Pd and Ru, the signature is more broad and complex and this is probably due to the overlap of the potential-pH diagram with the n-type doping region of the m-SWCNTs.

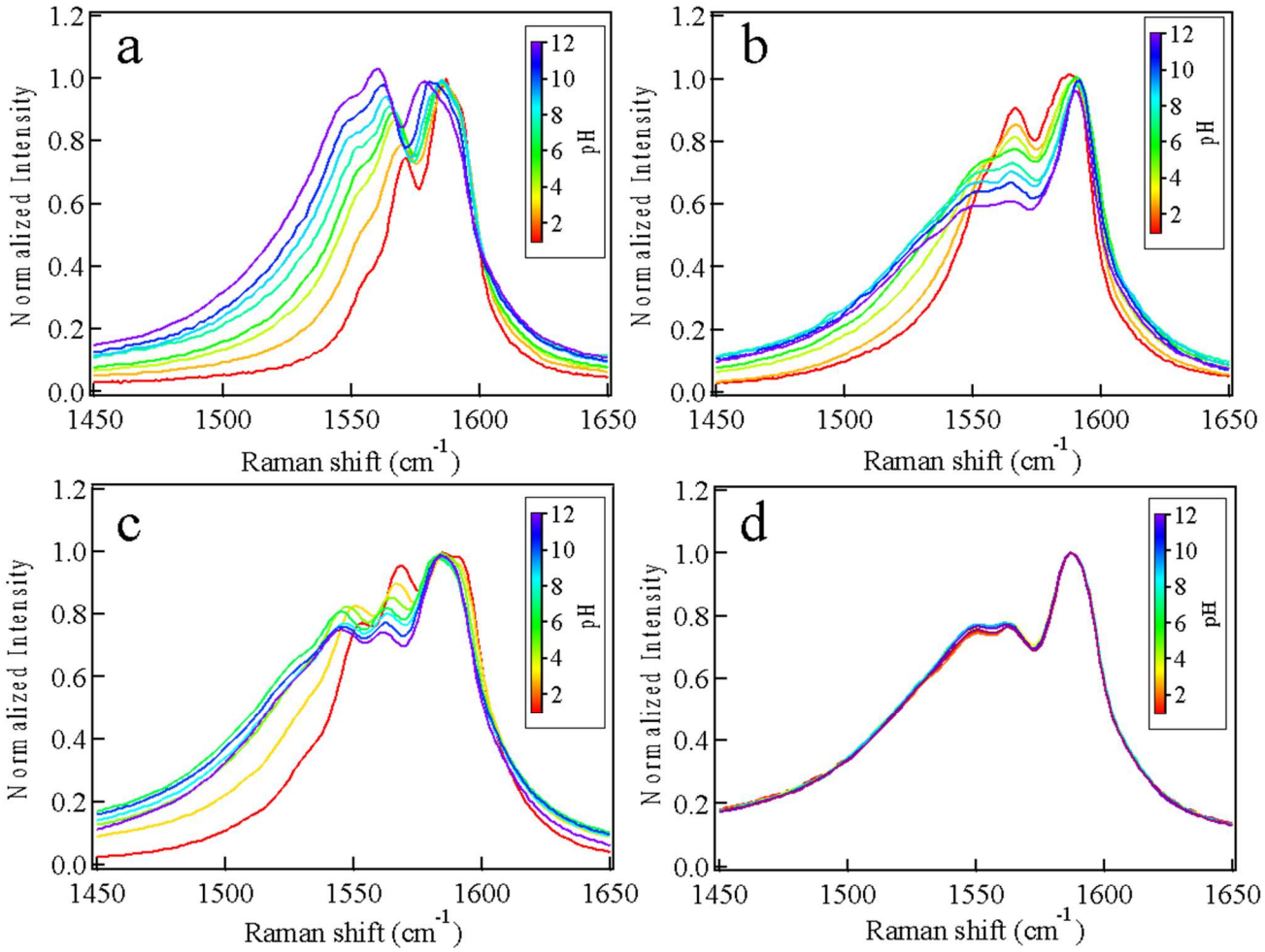

Figure 4.5. Raman spectra at 633 nm wavelength excitation versus pH of buffer solutions in contact with films of sorted metallic SWCNTs (m-SWCNTs) decorated with selected metals and deposited on a Si/SiO2 substrate: (a) Pt_N-m-SWCNTs, (b) Pd_N-m-SWCNTs, (c) Ru_N-m-SWCNTs and (d) uncoated m-SWCNTs. The spectra were recorded in buffer solutions of constant ionic strength (1 M) at unitary pH increments between 1 to 12.

4-2-6 Environmental Effects on pH Sensitivity

Our previous results demonstrate the high sensitivity of Pt-coated SWCNTs to the local pH. To develop a practical pH sensor, we specifically investigate the potential errors introduced by the local environment to the pH measurement. To highlight possible interferences from the substrate, two kinds of surfaces were prepared: i) parlyene-C deposited on an oxidized silicon wafer and ii) an aminoalkyl-silanized oxidized silicon wafer, for which the results are compared with those of an oxidized silicon substrate (i.e., without surface modification). On the one hand, we note that an organosilane surface significantly improves the adhesion of the SWCNT film, which is easily peeled off from the untreated Si/SiO_2. On the other hand, parlyene-C renders the adhesion more problematic while it should eliminate altogether the effect of the oxide surface on pH sensing as it has no acid/base functional groups capable of local charging. The shift of the G- mode of the Pt-SWCNTs with pH on these substrates is presented in Figure 4.6 (see Supporting Information for G_f mode shift and I(G-/G+)). The Raman shifts on all three surfaces are similar at low pH, but deviations are clearly observed at higher pH, which results in different slopes. Depending on the preparation and cleaning steps, the surface of the Si/SiO_2 wafer (without functionalization) can be chemically complex as it exhibits different densities of functional groups (silanols, protonated and deprotonated silanols), each with their own pKa. At a given pH, these groups influence the local surface charge next to the deposited SWCNTs. For example, the pKa of silanols (Si-OH) is approximately 5.6 or 8.5, depending if they are out-of-plane or in-plane, respectively, and protonated silanols ($Si\text{-}OH_2^+$) have a $pKa \sim 5$[202]. For clarity, the above pKa's are indicated by blue arrows in Figure 4.6. The silanization reaction converts the terminal silanols into amino groups ($pKa \sim 10$, black arrow), which adds further complexity to the surface depending on the density of all of the functional groups. As mentioned before, we probe the charge state of the SWCNTs for pH sensing and the results show that the different surface functional groups complicate the response and influence locally the charge density on the SWCNTs. The theoretical pKa values indicate that the silanized and untreated Si/SiO_2 surfaces have mostly basic groups, which is consistent with the deviations of the G- mode shifts from those of the parlyene-C at higher pH. Again, the effect of the supporting substrates demonstrates that the Pt-SWCNTs are highly sensitive to the local environment. The measurement of the pH is therefore influenced by the local potential, which induces an error compared to the electrochemical potential in the bulk of the solution.

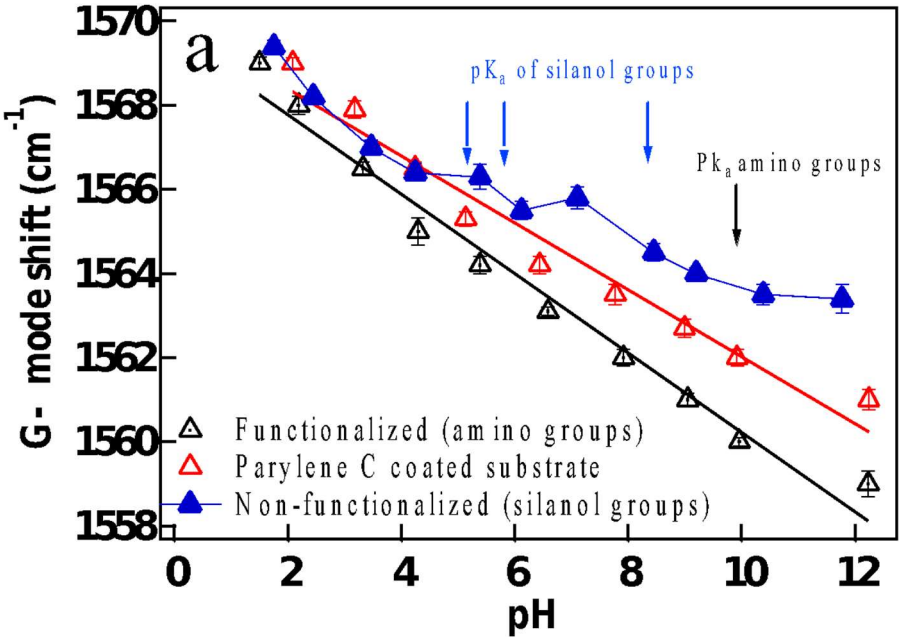

Figure 4.6. Raman shift of the G- mode of Pt-SWCNTs supported on three different substrates (aminopropyl-silanized, non-silanized, and parylene-C coated silicon/silicon oxide wafer) with pH in constant ionic strength (1 M) buffer solutions.

4-2-7 Performance of the pH Nanoprobe

To address the potential problem of uniformity in the preparation of the Pt-SWCNTs, we developed a synthesis procedure (see chapter 3) to prepare unsorted SWCNTs (laser ablation source) uniformly coated with Pt nanoparticles (Pt_N-SWCNTs) and used films of the synthesized Pt_N-SWCNTs as a proof of concept of a pH sensor. Figure 4.7(a) shows a TEM image of the morphology of the sample from which the size distribution of the Pt nanoparticles is obtained (Figure 4.7(b)). The Pt_N-SWCNTs deposited as a thin film on an aminoalkyl-silanized silicon/silicon oxide wafer were used to test the pH response of the sensor. Compared to the Parylene-C surface, which was found to induce residual stress after deposition (more information in the Supporting Information), the silanized surface, although more complex chemically, presents better adhesion and good stability. As shown in Figure 4.7(c), the Pt_N-SWCNTs provide the expected strong Raman response to pH, namely a shift of the G- mode by more than 7 cm^{-1} across the pH values between 2 and 12. The results for the G_f mode and the I(G-/G+) are shown in the Supporting Information. To examine the accuracy of a pH measurement, two different calibration

curves were constructed: a calibration based on solutions of 12 buffers of pH values between 1 and 12 (12-point curve) and another based on 3 buffers (3-point curve, pH = 1.93, 6.87, and 12.22). This procedure is analogous to the calibration of a standard pH meter with, for example, three buffer solutions.

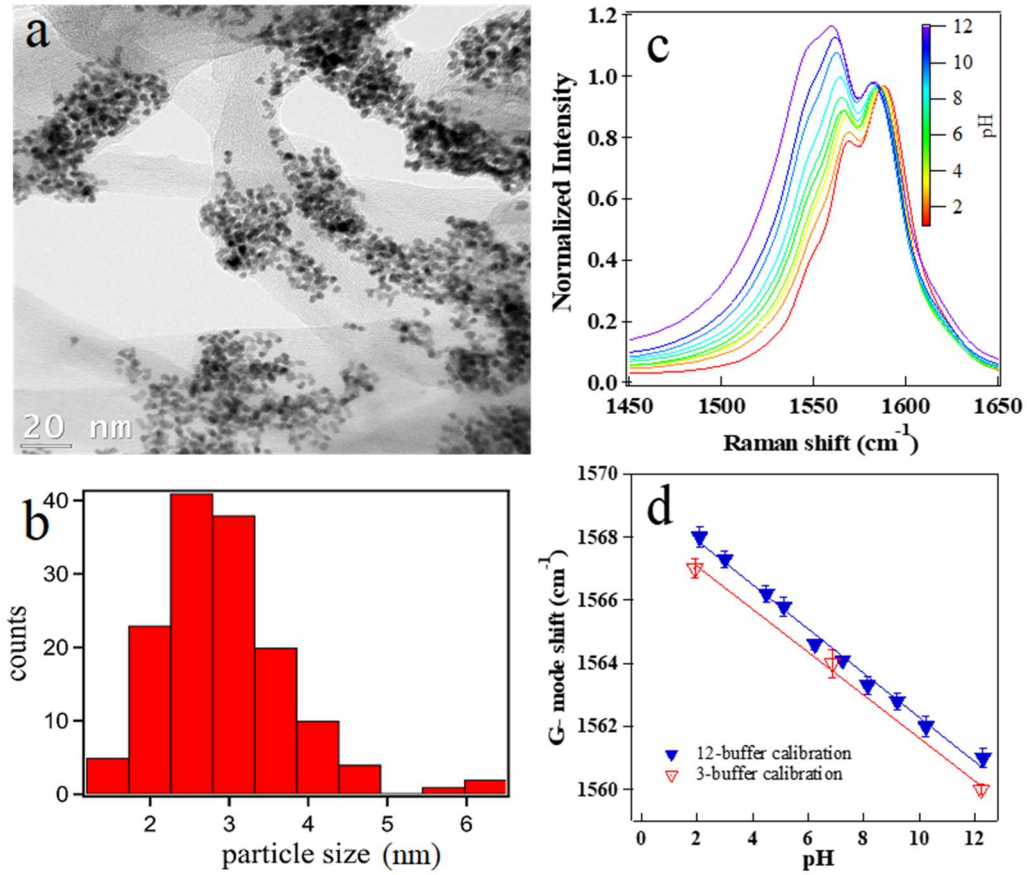

Figure 4.7. (a) TEM image of the platinum nanoparticles attached to the SWCNTs of the synthesized Pt_N-SWCNT pH sensor and (b) a histogram of the particle size distribution. (c) Raman spectra recorded in buffer solutions of a constant ionic strength of 1 M for unitary increments of pH. (d) Calibration curves based on the Raman shifts of the G- mode of Pt_N-SWCNTs supported on aminopropyl-silanized Si/SiO_2 versus the solution pH using 12 buffers (blue) or 3 buffers (red) solutions. Blue and red lines are linear regression of the 12 and 3 buffer data sets, respectively. The ionic strength of 1 M is used.

As seen in Figure 4.7(d), the calibration curves for the G- modes (see Supporting Information for G_f mode and I(G-/G+)) show similar slopes (-0.71 and -0.68 for 12- and 3-buffers, respectively). While the 12-point calibration is statistically more accurate, the 3-point calibration is much quicker to perform and shows a similarly good precision.

As a final proof of concept of the Pt_N-SWCNT pH sensor for analytical measurements, we prepared three different Pt_N-SWCNT samples and exposed them to solutions of different pH. For comparison, the pH of the test solutions was measured using a conventional pH meter equipped with a combined glass electrode. Using the standard calibrations in Figure 4.7(d), the solution pH was determined using the Raman shifts with the relation y(Raman-shift)=$b\oplus$(pH)+a, where $y(Raman\ shift) = bx(pH) + aa$ and b are fitting parameters (the uncertainty is obtained from the linear regression). Raman measurements were carried out on 5 different spots of the samples, each repeated 3 times. The data and fitting parameters are summarized in Table 4.1. The pH values determined from the 12-point calibration curve are very close to those measured using a commercial pH meter calibrated with three buffer solutions (pH = 4.01, 7.00, and 10.00). While the precision remains high across the full range, the accuracy of the Raman-based measurements is about ±700 mpH in basic solutions and ±500 mpH in acidic solutions. This slight difference is ascribed to the response of the silanized surface. The precision appears lower for acidic solutions with non-constant ionic strength, which is expected considering the importance of the ion concentration for screening the local electrochemical potentials. Using the 12-point calibration, both the precision and accuracy is generally improved, but the procedure requires additional effort to gain better statistics.

The remote platinum-coated SWCNT optical sensor presents improved flexibility and accuracy compared to other electrodeless optical sensors[203-205], which have issues such as a limited pH range and lack of accuracy. One recent non-conventional pH sensor based on a graphene transistor, that includes working and reference electrodes, provides for instance a much higher accuracy of ~0.1 mpH, but it is electrically biased relative to a reference electrode[40]. Compared to conventional (electrode-based) pH meters, which provide accuracies ranging from ±0.1 pH to ±0.001 pH (e.g., Mettler Toledo and Fisher Scientific instruments), the Pt_N-SWCNT-based Raman sensor in its current version shows a lower accuracy. It has, however, the advantages of being optically addressed, electrodeless, and of nanoscale dimensions. Hence, the Pt_N-SWCNT pH sensor is

uniquely flexible and appears complementary and useful for remote investigations of the local pH at the nanometer scale or in living cells.

Table 4.1. pH values of unknown solutions (at constant and non-constant ionic strengths) obtained from 3-point and 12-point calibration curves using the Raman shift of the G- mode. For comparison, the pH from a conventional pH meter is also given.

pH* Conventional pH meter	pH (3 buffers)** Pt_N-SWCNTs	pH (12 buffers)*** Pt_N-SWCNTs
4.80 ± 0.01 (I = 1 M)	3.4 ± 0.9	4.5 ± 0.7
11.80 ± 0.01 (I = 1 M)	11 ± 1	11.5 ± 0.7
4.50 ± 0.01	3.3 ± 0.8	4.5 ± 0.5
11.00 ± 0.01	10 ± 1	10.8 ± 0.7

* Note: error is the instrumental error
** Note: error of 3 buffers is obtained using the parameters: $a = 1568.4 \pm 0.3$; $b = -0.68 \pm 0.04$
*** Note: error of 12 buffers is obtained using the parameters : $a = 1569.3 \pm 0.2$; $b = -0.71 \pm 0.02$

Finally, a definitive proof of the doping model of the Pt_N-SWCNT films with pH was obtained using electrical resistance measurements performed buffer solution of different pH and constant ionic strength (Supporting Information in section 4-4, Figure 4.17). We found that the film resistance increased by 39% going from pH 1.89 to pH 11.98. This is consistent with our Raman study that shows the films go from a heavily p-doped state to an undoping state at higher pH, depleting the film of hole charge carriers and thus increasing the film resistance. Compared to films of uncoated SWCNT films, the change in film resistance is significantly less, down to 6%.

4-3 Conclusion

We characterized the spectral response of single-walled carbon nanotubes coated with platinum to pH across a broad range of pH from 1 to 12 and compared it to that of uncoated SWCNTs. Two preparation methods giving SWCNTs coated with a thin film of Pt and SWCNTs functionalized with Pt nanoparticles (Pt_N-SWCNTs) were compared and both exhibited a significant transformation of the Raman spectra with pH in the region of the G-band of the nanotubes. This

effect is ascribed to charge transfer doping between the Pt/PtO redox pair and the SWCNT electrode. While uncoated SWCNTs appear to be a bad redox couple for pH measurements, the pH responsive Pt_N-SWCNTs provide precise and referenced measurements of the solution electrochemical potential through the reaction with the Pt/PtO redox system, giving an accuracy as low as ±500 mpH unit in acidic (pH = 1-7) solutions of constant ionic strength (1 M). The nanotube-based optical pH sensor exhibits slight differences in acidic and alkaline solutions, which is ascribed to the surface functional groups of the supporting substrate and is sensitive to the ionic strength of the solutions. Our findings pave the way to the design of electrode-less nanoprobes for optical measurements of the local pH across the full pH range for potential applications such as in-situ cancer cell detection, metabolism studies, etc.

4-4 Supporting Information

4-4-1 Effect of the Internal Stress of Parylene-C Coated Silicon Wafer on the Raman Spectra.

Poor adhesion of films of SWCNTs to parylene-C coated substrates using the transfer technique can be a source of internal stress[206]. The presence of stress is shown in Figure 4.8. The Raman spectra acquired at two different spots of uncoated SWCNTs in the dry state (Figure 4.8(a,b)) give bands with different positions. Many reports suggest that annealing the substrate can reduce stress as it recrystallizes the parylene interfaces[207, 208]. Hence, the sample was annealed at 300°C under vacuum to remove this internal stress and the results are shown in Figure 4.8(c,d). The Raman spectra of uncoated SWCNTs in the dry state are overlaid on those of the sample in the buffer solution at two different pH values (pH = 2.01 and pH = 12.00).

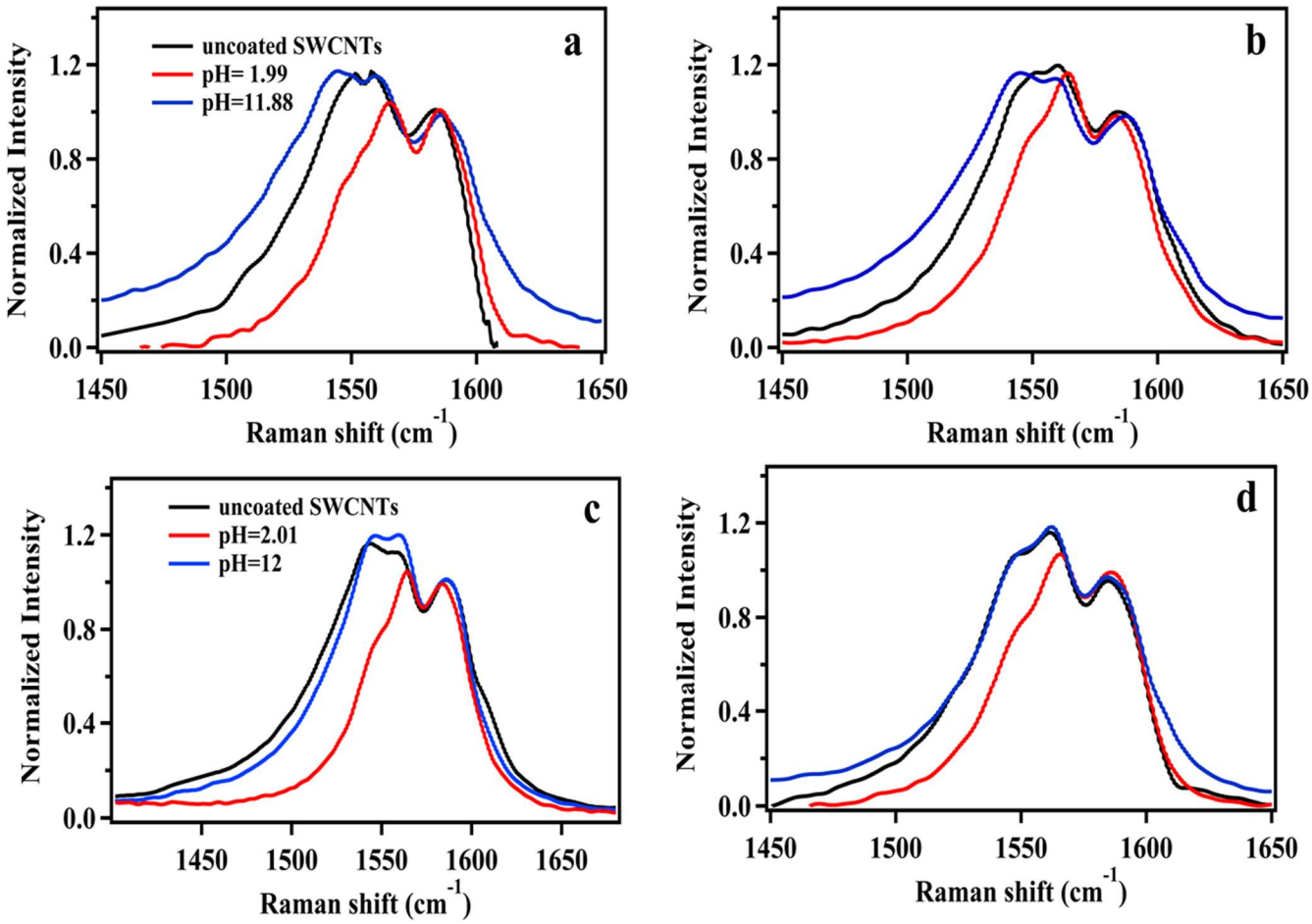

Figure 4.8. Raman spectra at 633 nm wavelength excitation of SWCNTs on parylene-C coated substrates taken before and after annealing at two different spots (a and b) and (c and d), respectively. Spectra recorded in the dry state are in black; acidic buffer solution in red, and basic buffer solution in blue.

4-4-2 Additional Results

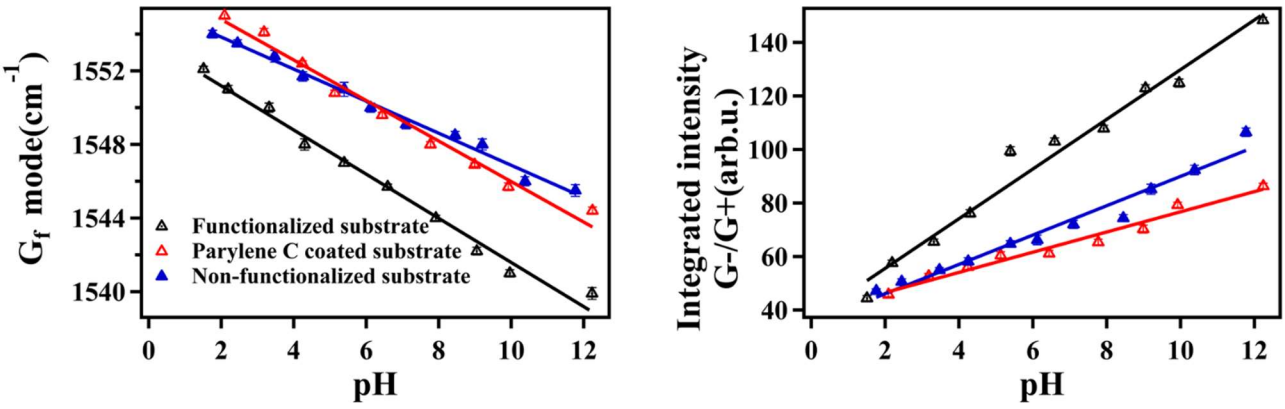

Figure 4.9. Raman shift of the G_f mode and the I(G-/G+) ratio, i.e. the normalized integrated intensity of the G- mode relative to the G+ mode of Pt-SWCNTs in buffer solutions of constant ionic strength (1 M) with three different substrates (aminopropyl-silanized, non-silanized, and parylene-C coated silicon/silicon oxide wafer).

4-4-3 Effect of the Laser Excitation Wavelength on the Raman Response

The two main sources of SWCNT used in our study, the laser ablation SWCNTs and the sorted metallic SWCNTs from Raymor-NanoIntegris, exhibit different diameter distributions. The laser ablation source has diameters between 1.1 and 1.5 nm whereas the sorted metallic SWCNTs from Raymor NanoIntegris have diameters in range between 1.2 nm to 1.7nm. They have as a result different response in Raman. Figure 4.10 resume the response of the Pt-SWCNT system observed from these sources at three different excitation wavelengths (633nm (red line), 514nm (green line) and 488 nm (blue line). The spectra show the radial breathing mode, the G-band and the 2D band regions for each source.

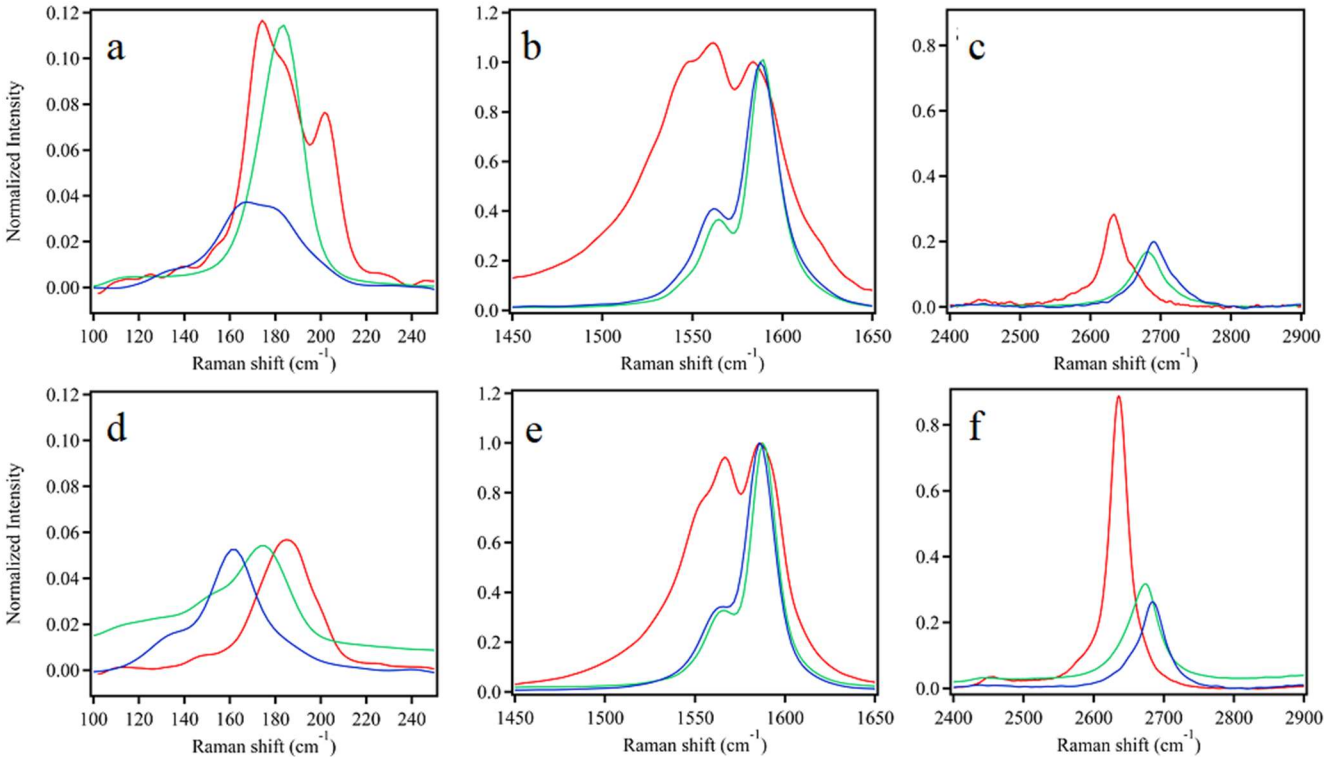

Figure 4.10. Comparison of Raman spectra under three different excitation wavelength 633nm (red line), 514nm (green line) and 488 nm (blue line) of Pt-SWCNT supported on Si/SiO_2-supported made using unsorted laser ablation nanotubes (a: radial breathing mode; b) G-band and c: 2D band regions) and using sorted metallic SWCNTs (Raymor NanoIntegris) ((d: RBM, e: G-band and f: 2D band)

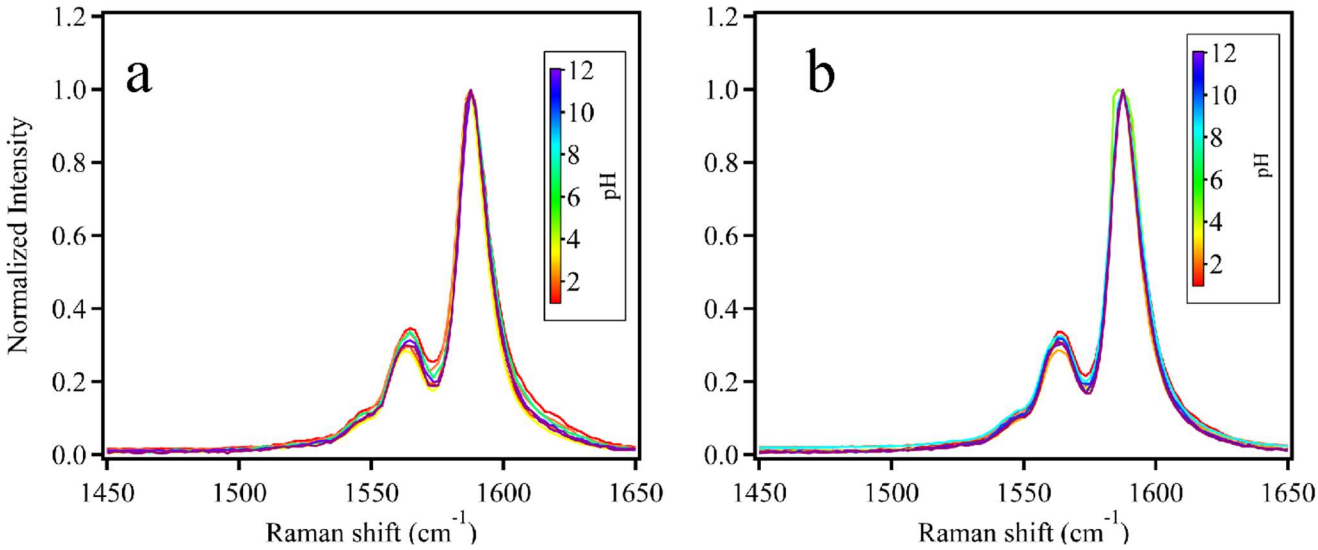

Figure 4.11. pH response of resonantly excited semiconducting Pt-SWCNTs (laser ablation source) at 514 nm wavelength excitation. The spectra show a zoom in G-band of Raman spectra of Si/SiO_2-supported films of Pt-SWCNTs in two different spots (a and b) in constant ionic strength buffer (1M) at different pH value between 1 and 12.

4-4-4 Comparison Between Different Transition Metals

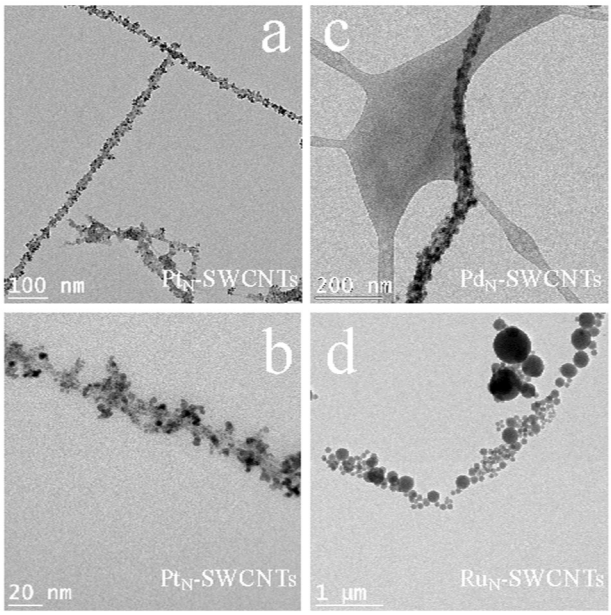

Figure 4.12. TEM images of metal nanoparticles deposited on metallic m-SWCNTs (Raymor NanoIntegris). Left Pt_N-m-SWCNTs, Middle: Pd_N-m-SWCNTs and Right: Ru_N-m-SWCNTs.

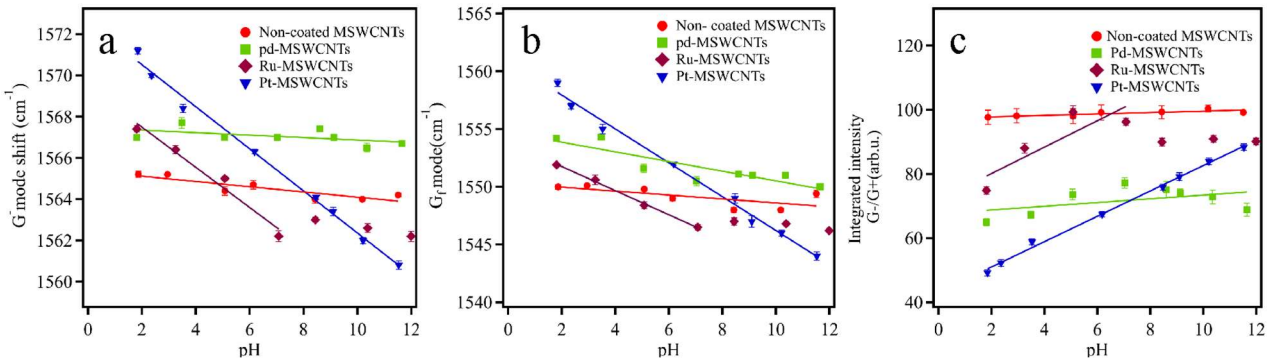

Figure 4.13. Spectral changes for thin films of Non-coated m-SWCNTs, Pt_N-m-SWCNTs, Pd_N-m-SWCNTs and Ru_N-m-SWCNTs as a function of pH obtained using constant ionic strength buffers (1 M). (a) Energy shifts of the G- mode and (b) G_f mode and (c) normalized integrated intensity of the G- mode relative to G+ mode. Note the line fits for Ru samples are limited to the acidic buffer solutions.

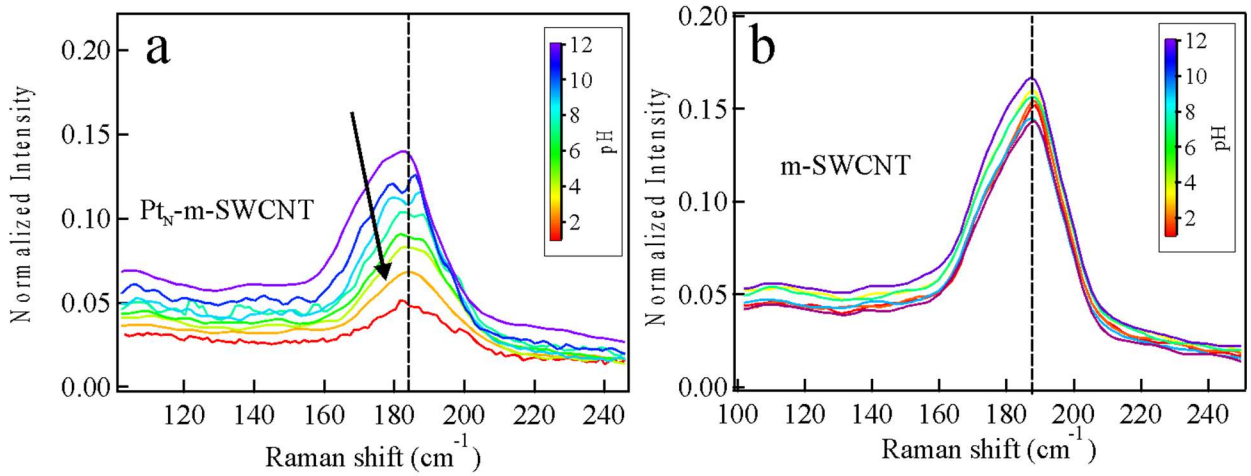

Figure 4.14. Raman radial breathing mode region vs. solution pH of (a) resonantly excited Pt_N-m-SWCNTs (b) and uncoated m-SWCNT at 633 nm wavelength excitation.

4-4-5 Additional Results and Proof of Concept of the Pt_N-SWCNT Nanoprobe

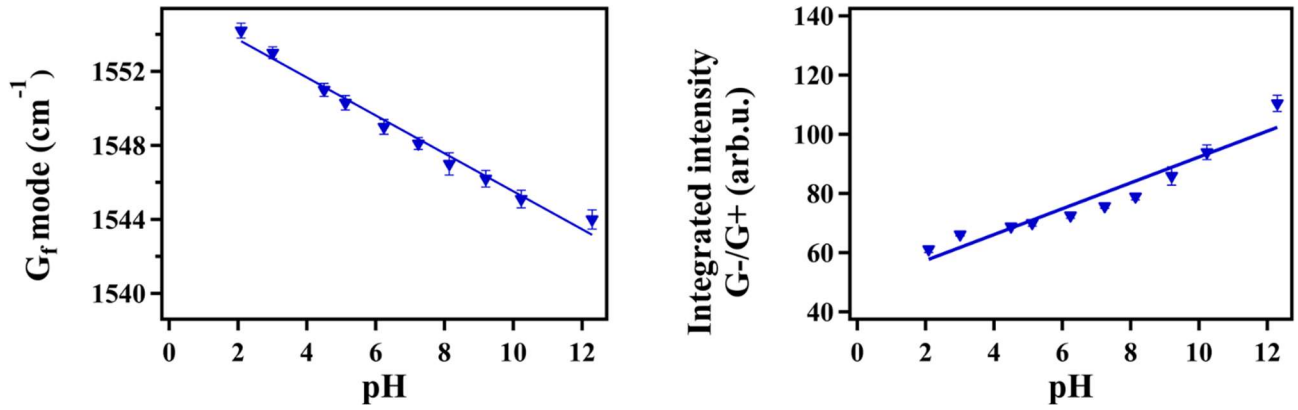

Figure 4.15. Variations of the Raman shift of the G_f mode and the I(G-/G+) ratio, i.e. the normalized integrated intensity of the G- mode relative to the G+ mode of Pt_N-SWCNTs vs pH at constant ionic strength (1 M).

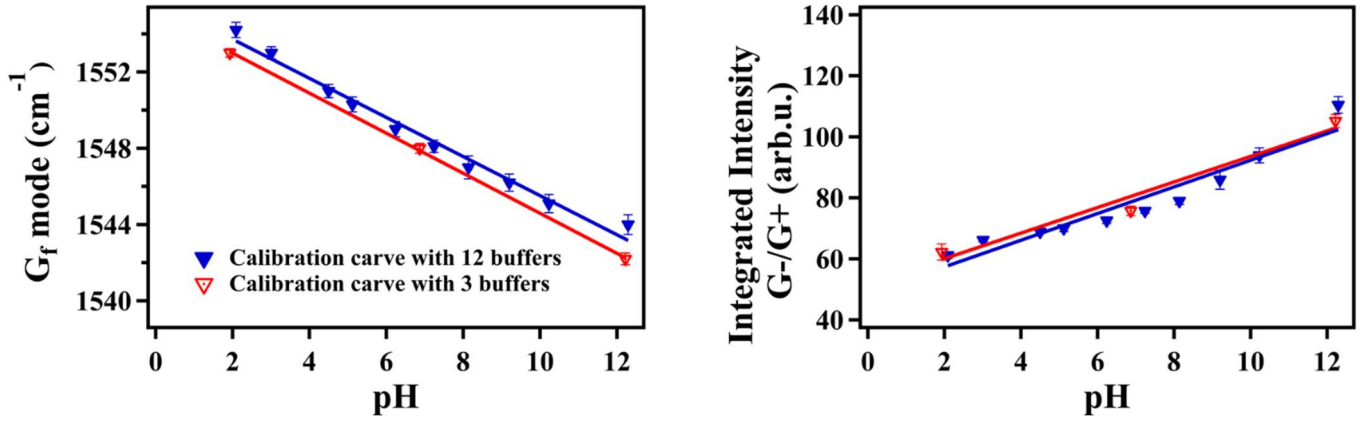

Figure 4.16. Calibration curves based on the Raman shifts of the G_f mode and the I(G-/G+) ratio, i.e. the normalized integrated intensity of the G- mode relative to the G+ mode of Pt_N-SWCNTs versus pH using solutions of 12 buffers (blue) and 3 buffers (red).

4-4-6 Calculations of the Uncertainty in the pH Values Determined from the Raman Shifts and Intensities

A linear regression using y(Raman-shift)=b·(pH)+a, where $y(Raman\ shift) = bx(pH) + aa$ and b are fitting parameters, was performed using the standard curves with different buffers (Figure 4.7(d)). One can determine from the Raman shift the pH value using: pH=[y(Raman-shift)–a]/b.

The fitting parameters a and b are given for each calibration curve under the Tables for each parameter extracted, G- (Table 4.2), G_f (Table 4.4) or I(G-/G+) (Table 4.6). The Raman parameters G_f and I(G-/G+), for each unknown solution with the associated standard deviation are given in Tables 4.3, 4.5, respectively. The uncertainty on the pH is therefore obtained using $\frac{\Delta pH}{pH} = \frac{(\Delta y + \Delta a)}{|y-a|} + \frac{\Delta b}{|b|}$.

Table 4.2. Raman shift of the G- mode repeated at different spots for each unknown sample; standard deviation and mean of the Raman shifts as well as pH measured using a conventional pH meter.

pH Conventional pH meter	Raman shift G- mode (cm^{-1}) in different spots	Standard Deviation (SD) Mean of data (Mean)
4.80 ± 0.01 (I = 1 M)	1566.2 1566.2 1565.8 1565.9 1566.3	Mean = 1566.1 SD = 0.2
11.80 ± 0.01 (I = 1 M)	1561.1 1561.1 1561 1560.9 1561.2	Mean = 1561.1 SD = 0.1
4.50 ± 0.01	1566.1 1566.3 1566.2 1566.1 1566	Mean = 1566.1 SD = 0.1
11.00 ± 0.01	1561.8 1561.7 1561.6 1561.5 1561.6	Mean =1561.6 SD = 0.1

Table 4.3. pH value of unknown samples (at constant and non-constant ionic strength) with different calibration curves using the Raman shift of the G_f mode.

pH Conventional pH meter	pH* Pt_N-SWCNTs (3 buffers)	pH** Pt_N-SWCNTs (12 buffers)
4.80 ± 0.01 (I = 1 M)	4.0 ± 0.5	4.8 ± 0.5
11.80 ± 0.01 (I = 1 M)	11.1 ± 0.6	12.0 ± 0.8
4.50 ± 0.01	3.3 ± 0.4	4.1 ± 0.5
11.00 ± 0.01	10.2 ± 0.6	11.1 ± 0.8

* Error obtained using the calibration curve with 3 buffers: $a = 1555.1 \pm 0.2$; $b = -1.05 \pm 0.02$

** Error obtained using the calibration curve with 12 buffers: $a = 1555.8 \pm 0.3$; $b = -1.03 \pm 0.05$

Table 4.4. Raman shift of the G_f mode repeated at different locations of each test sample. Mean and standard deviation of the Raman shifts as well as the pH measured using a conventional pH meter.

pH Conventional pH meter	Raman shift of G_f band (cm^{-1})	Standard Deviation and Mean of data
4.80 ± 0.01 (I = 1 M)	1550.7 1551.2 1551 1550.8 1551	Mean = 1550.9 SD = 0.2
11.80 ± 0.01 (I = 1 M)	1543.5 1543.4 1543.3 1543.2 1543.5	Mean = 1543.4 SD = 0.1
4.50 ± 0.01	1551.8 1551.7 1551.5 1551.6 1551.5	Mean = 1551.6 SD = 0.1
11.00 ± 0.01	1544.4 1544.3 1544.5 1544.3 1544.6	Mean = 1544.4 SD = 0.1

Table 4.5. pH value of unknown samples at constant (1 M) and non-constant ionic strength using different calibration curves and the variation of I(G-/G+), i.e. the integrated intensity of the G- mode normalized with the G+ mode.

pH Conventional pH meter	pH* Pt_N-SWCNTs (3 buffers)	pH ** Pt_N-SWCNTs (12 buffers)
4.8 ± 0.01 (I = 1 M)	4 ± 2	5 ± 2
11.8 ± 0.01 (I = 1 M)	12 ± 4	12 ± 3
4.5 ± 0.01	4 ± 2	4 ± 2
11.0 ± 0.01	11 ± 3	11 ± 3

* Error obtained using the calibration curve with 3 buffers: $a = 52 \pm 7$; $b = 4.2 \pm 0.8$
** Error obtained using the calibration curve with 12 buffers: $a = 49 \pm 4$; $b = 4.4 \pm 0.5$

Table 4.6. The I(G-/G+) ratio, i.e. the integrated intensity of the normalized G- mode relative to G+ mode, mean and standard deviation of the data for solutions of different pH as well as the pH measured using a conventional pH meter

pH Conventional pH meter	Normalized I(G-/G+) (different spots)	Mean of data (Mean) Standard Deviation (SD)
4.80 ± 0.01 (I = 1 M)	69.2 68.8 68.3 70.4 68.9	Mean = 69.1 SD = 0.8
11.80 ± 0.01 (I = 1 M)	101.7 97.3 102.4 103.9 99.2	Mean = 101 SD = 3
4.50 ± 0.01	69.4 68.6 69.1 68.1 67.2	Mean = 68.5 SD = 0.9
11.00 ± 0.01	95.1 99.3 94.6 96.7 100.1	Mean = 97 SD = 3

4-4-7 Electrical Measurements

Figure 4.17 shows the film resistance in ionic constant buffer solution of pH 1.89 to 11.98 normalized to pH 7. Due to a large hysteresis (shaded blue), multiple sweeping of the full range of pH were measured to determine stability and reproducibility of the results. Doing a linear fit, there is a 39% change of film resistance from the whole pH range. The hysteresis observed was up to 16% after going a full sweep cycle. We compared this to films of uncoated SWCNT and observed a smaller change in film resistance of 6%.

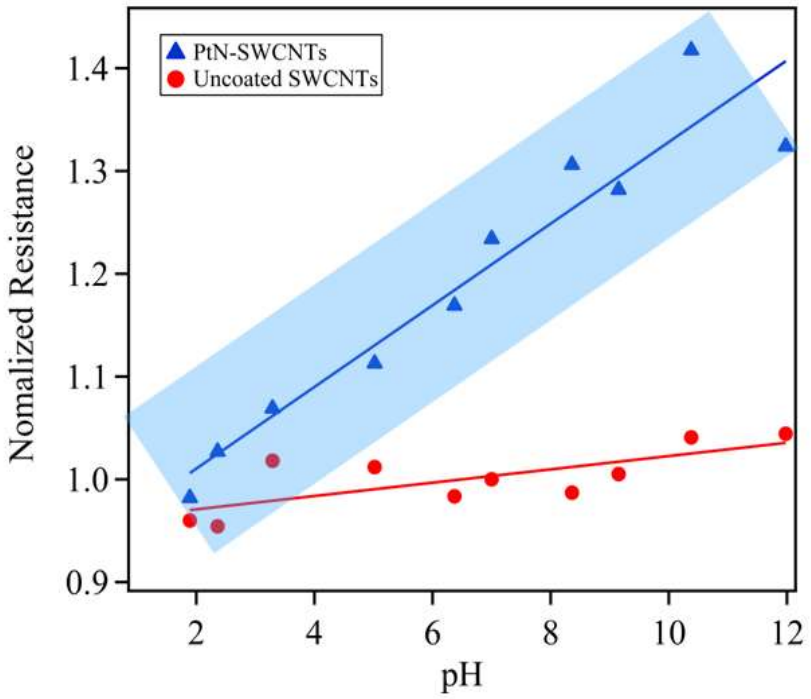

Figure 4.17. Normalized resistance of PtN-SWCNT (▲) and uncoated SWCNT (●) films in ionic constant buffer solution from pH 1.89 to 11.98. Shaded blue area represents the maximum hysteresis observed in PtN-SWCNT.

Chapter 5: pH Dependency of Graphene in Contact with Platinum

Graphene is a one atom thick material in which all the carbon atoms are at the surface and exposed to the local environment [209-211]. A graphene layer can therefore interact with ions in solution. It is therefore expected, and observed experimentally, that the properties of graphene are significantly affected by analytes in solution[212, 213]. Similar to the case of carbon nanotubes, this conjuncture along with advances on surface functionalization has stimulated a plethora of studies on the use of graphene for high performance chemical sensors[214, 215].

At the core of the sensing principle behind this thesis, early work on graphene devices have shown that graphene can be doped in solution in two distinct ways: using an applied electric field or by a direct exposure to an adsorbate, which can be either a reductant or an oxidant. On one hand, the electric field doping is generally performed using graphene-field effect transistors (FET), in which charge carriers are induced by establishing an electric potential between the graphene layer and a gate electrode. In air, the concentration of charge carriers can be freely tuned by changing the gate Voltage and measured by the current, but the doping levels obtained are rather low because of the small capacitance of the gate stack, which is generally limited by the oxide thickness and its dielectric constant [87, 216]. Using the FET configuration, it was shown, after many conflicting reports, that graphene transistors are unintentionally p-doped in ambient conditions and additional care must be made to control the initial doping of the graphene[217]. In relation with pH sensing, it was also shown that the graphene itself (*i.e.* when unfunctionalized) is not sensitive to the pH of the solution[218]. Significantly higher doping levels can be achieved with graphene FET using electrolyte gating, which led to demonstrations of sensing devices in solution operating near the quantum-capacitance limits, with pH detection approaching the Nernstian limit of 55 mV/pH[219]. Through surface functionalization, graphene ion sensing FET (ISFET) arrays have shown significant improvement and can provide now selectivity to ion detection near the sensitivity limits of such device of 60 mV per decade at room temperature[220].

The other form of doping involves charge transfer at the graphene surface, which occurs via a direct interaction between graphene and the adsorbed molecules [221]. When the absorbates participate in an electrochemical redox reaction, higher doping levels than field-effect doping is possible due to significant difference of the chemical potentials of the graphene and molecules, such as hydrazine or 2,3-dichloro-5,6-dicyano-p-benzoquinone (DDQ), in solution [222].

As a good example of the latter, past studies in our group have highlighted the ubiquitous role of the molecules in the environment in graphene p-type doping, which is ascribed to the water/oxygen redox couple [217]. Ambient doping of graphene by the changing the redox potential involves the following equilibrium reaction: $O_2(aq) + 4\,H^+ + 4\,e^-(graphene) \rightleftharpoons 2\,H_2O$, which predicts a shift in equilibrium with pH, an apparent contradiction with the work in reference 195. An example of the Fermi level position of graphene in contact with the O_2/H_2O redox couple in equilibrium conditions at pH = 1 is illustrated in Figure 5.1 (right). Provided that an oxidized species can be stabilized at the surface of the graphene, this model predicts a strong p-doping of the layer at acidic pH.

In this last chapter, we explore more specifically the use of graphene instead of carbon nanotubes as a pH sensitive electrode. This study can serve as a basis to generalize the principles presented earlier in this thesis using SWCNT materials. This work targets better accuracy and aims to deepen further our understanding of the Nernstian behavior of the graphene electrode system. Here, we postulate that a graphene layer when in contact with a Pt/PtO redox couple should exhibit strong pH dependency in aqueous solutions as illustrated in Figure 5.1 (left). In this chapter, we make use of Raman measurements to probe the doping of the graphene reference electrode in solution.

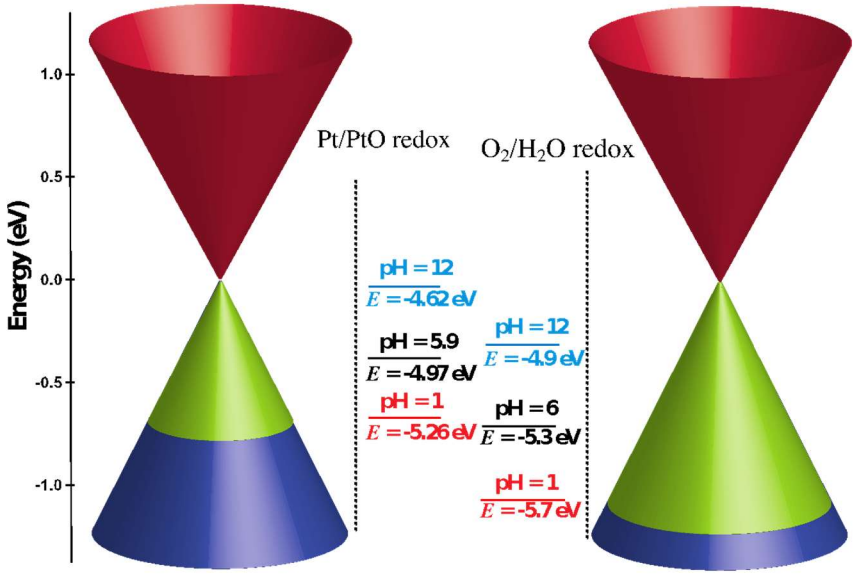

Figure 5.1. Doping mechanism of graphene via two different redox couples in solutions of pH=1. Schematic of the electronic state of graphene near a K-point of the Brillouin zone and the electrochemical potential of the Pt/PtO (left) and O_2/H_2O (right) redox couple at different pH. The equilibrium position at pH = 1 is shown for both of these redox systems in contact with graphene. The energy scale is based on a graphene work function of 4.6 eV. Blue and red regions of the Dirac cone indicate occupied and unoccupied states in graphene and a p-doing for both cases is shown.

5-1 Preparation of the Samples

In these experiments, two samples were investigated: uncoated graphene (u-graphene) and platinum coated graphene (Pt-graphene). The latter defines a direct (physical) contact with the Pt/PtO redox couple. The graphene was grown on a copper foil by chemical vapor deposition at 1000 °C using methane as a carbon source and the layer was transferred using PMMA to a silicon wafer covered with a 300 nm thick oxide layer. The uncoated graphene sample was prepared by removing the PMMA in an acetone bath, followed with drying by IPA. The platinum coated graphene sample was prepared the same way as uncoated graphene with an extra step that consists of coating the surface with a thin layer (~ 6 nm) of platinum using e-beam deposition. The Britton – Robinson buffer solutions of constant ionic strength (1M) were prepared using the same procedure as detailed in chapter 3. Raman spectra were acquired using a custom built spectrometer equipped with different laser excitation lines (488, 514, 532, and 633 nm) and a nitrogen-cooled silicon detector array ((JY Symphony) mounted on a Jobin-Yvon Triax iHR550 spectrometer (grating 1,800 g·mm blazed at 630 nm) with a precision of 0.2 cm^{-1}. The laser power was kept near 1000 μW on the sample and the signal was collected at near-diffraction limited resolution using a 50× objective with a numerical aperture of 0.5. Spectra in solution were acquired *in-situ* using the setup described in section 3-7 of Chapter 3.

5-2 Results and discussion

Figure 5.2 presents the Raman spectra at λ_{ex} = 488 nm in the G-band (1525–1660 cm^{-1}) and D-band (1300–1425 cm^{-1}) regions for both samples, u-graphene and Pt-graphene, in buffer solutions of pH ranging from 1.60 to 11.89. The top and bottom panels present the results for u-graphene and Pt-graphene, respectively. At first sight, the results show strong shifts of the bands with pH for the Pt-graphene sample. Further experiments performed at λ_{ex} = 514 nm (not shown here) gave the same results except that the signal to noise (S/N) ratio are much lower due to a Raman cross section one thousand times lower than that of carbon nanotubes[184].

As discussed already in Chapter 2, the G-band is a first-order scattering process associated with degenerated phonon modes (iTO and LO) at the Γ point (i.e. at the center of the Brillouin zone). These phonons consist of in-plane vibrations of the sp^2-hybridized carbon lattice. In contrast, the D-mode is a second-order process involving light scattering with two iTO phonons near the K point of opposite, yet high, momenta so that the scattering process takes place across the Brillouin zone. Both of these modes undergo a blue shift with increasing doping and this surprising behavior has been extensively discussed in the literature[135, 136]. As seen in Figure 5.2 for Pt-graphene, a change in pH from 1 to 12 induces a gradual red shift of the D-band and G-band of about 12 cm^{-1} and 25 cm^{-1}, respectively, whereas the shift of both is generally less than 1 cm^{-1} for u-graphene. As per the results with the metallic nanotubes in Chapter 4, the shifting trend observed here is consistent with a charge transfer reaction at the surface of the graphene with the protons in the buffer solution. Considering that doping induces a blue shift of the Raman bands, it is possible to deduce that the Pt-graphene appears strongly p-doped at pH = ~1 and its doping level decreases significantly with increasing pH across the whole range. At pH 12, the Raman shift of the G-band is at ~1583 cm^{-1}, which indicates that graphene is nearly undoped at this point [135, 136].The G-band spectra for u-graphene show a slightly blue shifted position at pH=1 near to ~1580 cm^{-1}, i.e. weak p-doping, but the graphene remains nearly undoped across the full pH range investigated. The absence of a pH dependency of the Raman bands of u-graphene is not surprising and consistent with earlier results by Schöenberg's group using graphene transistors[218]. The direct comparison between u-graphene and Pt-graphene illustrates well the important role of the surface functionalization with Pt in this doping process.

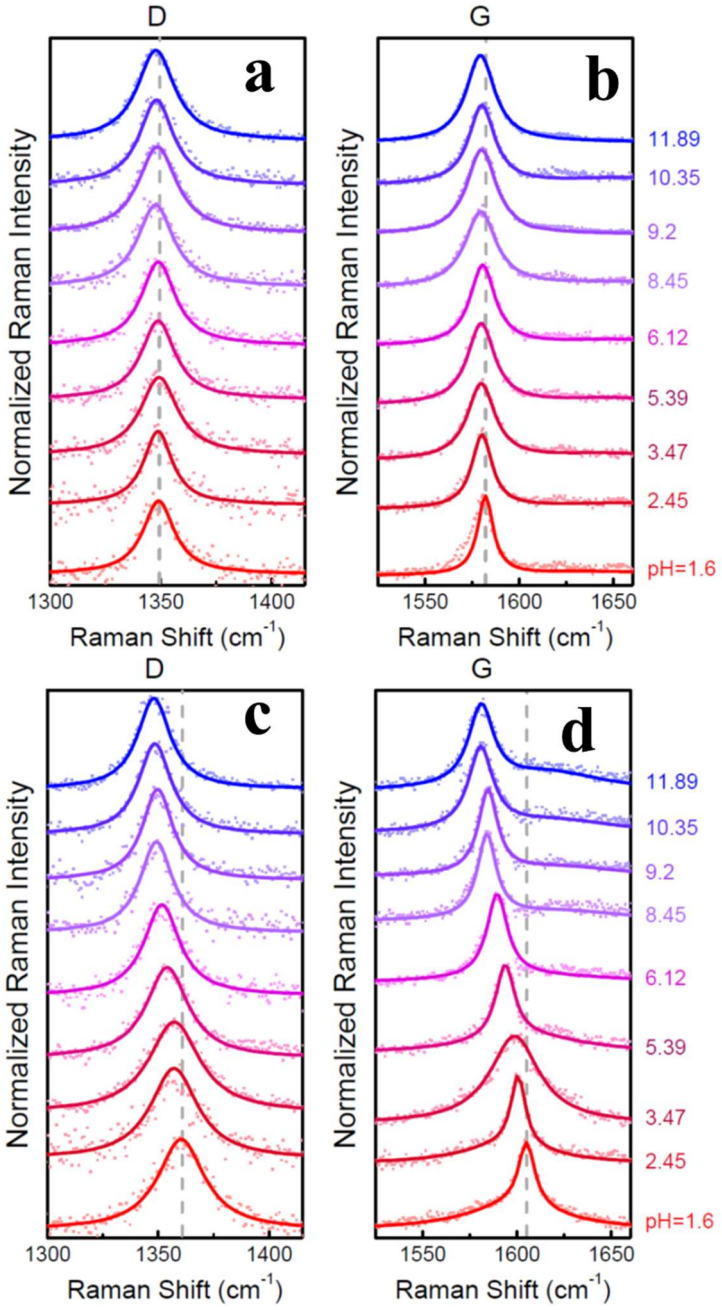

Figure 5.2. Comparison of the Raman spectra of Si/SiO_2-supported films of (a,b) uncoated graphene (u-graphene) and (c,d) platinum coated graphene(Pt-graphene). (b,d) and (a,c) show the G-band and D-band regions, respectively. The spectra were recorded in buffer solutions of constant ionic strength (1 M) at unitary pH increments between 1.60 and 11.89. Lorentzian fits to the spectra are shown.

As shown in the schematic of Figure 5.1, this electrochemical doping is consistent with a charge transfer between the redox couple in interaction with the graphene electrode. That is, the equilibrium requires that the electrochemical potential of a redox couple, E_{redox}, is aligned with the electrochemical potential of the graphene electrons, which sets the graphene Fermi level, E_f. A difference between E_{redox} and E_f should drive a charge transfer process between the graphene and the redox couple until the equilibrium is reached between the two systems (i.e., $E_{redox} = E_f$). The case of pH=1 is illustrated in Figure 5.1, which predicts a strong p-doping of graphene at this equilibrium position with the redox couples present at the surface (i.e. Pt/PtO and O_2/H_2O redox pairs shown on the left and right panels, respectively). At pH = 1, the Pt/PtO system acts as a charge acceptor, which drives the E_f of graphene well below the neutrality (or so-called Dirac) point, which is the reference point in the diagram located at zero relative energy. This is in effect a charge transfer from the graphene to the Pt.

As mentioned above, a shift in E_f of the graphene causes a blue shift of the Raman G-band and this signal can therefore be used to determine experimentally the doping state of graphene. Assuming that an equilibrium is reached in the solution, one can use the Raman response to probe the potential of the graphene to assess the potential of the solution in the vicinity of the graphene surface. To test the hypothesis of the equilibrium behind the use of the Raman signal as a reference, we have reported in Figure 5.3 the fitting results for the D-band (panel a,c) and G-band (panel b,d) at each pH value for both samples, respectively. The spectra were fit using a Lorentzian function and Figure 5.3 reports the peak maxima for each buffer. For Pt-graphene, the Raman shift of the G-band vs. pH is nearly linear and the slope is -2.4 ± 0.2 cm^{-1} per pH unit (the correlation coefficient is -0.98). This is much steeper than for u-graphene (-0.13± 0.06 cm^{-1} /pH unit), giving about 2 cm^{-1} shift in total across the range of pH compared to 24 cm^{-1} for Pt-graphene. The Raman shift with pH of the D-band appears also nearly linear and the slopes are -1.2 ± 0.1 cm^{-1}/pH and -0.12± 0.03 cm^{-1} /pH for Pt-graphene and u-graphene, respectively. Overall, the results demonstrate strong doping of the graphene in contact with platinum and that the doping is inversely proportional to the pH of the solution. The u-graphene sample undergoes only a weak p-doping with decreasing pH and it is clear that the graphene itself does not follow the expected equilibrium with the O_2/H_2O redox couple.

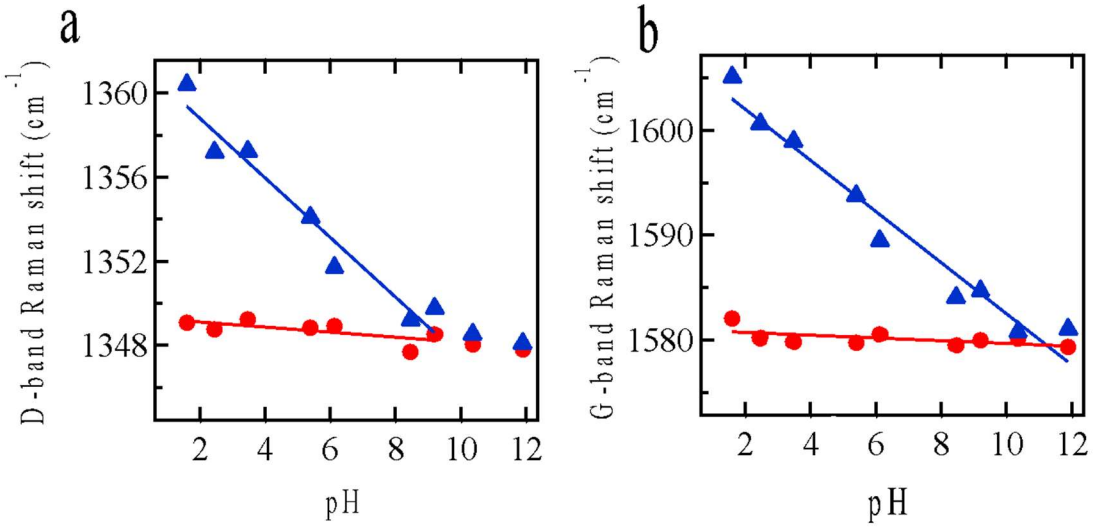

Figure 5.3. Energy shifts of the D- (a) and G-bands (b) for uncoated graphene (red, ●) and Pt-coated graphene (blue, ▲) as a function of pH obtained in buffer solutions of constant ionic strength (1 M) and an excitation wavelength of λ_{ex} = 488 nm. The positions are determined using Lorentzian fits on each spectrum.

The different pH dependencies of the G-band are rationalized by a redox reaction occurring in the environment near the graphene film. As mentioned in Chapter 4, an electrochemical charge transfer process at this interface can be used to describe the doping of graphene in a buffer solution. Considering, for instance, a reaction with the O_2/H_2O redox couple using $O_{2(aq)} + 4H^+_{(aq)} + 4e^-$ (graphene) $\rightleftharpoons 2H_2O_{(l)}$, one can infer the energy level (in eV) at equilibrium using the following relationship: $E_{abs,O_2/H_2O} = -5.669 + 0.059 \cdot \text{pH}$ (in eV). This gives at equilibrium a Fermi energy position relative to the vacuum level between -5.61 eV and -4.95 eV for pH between 1 and 12, respectively. Considering a work function of roughly 4.6 eV for graphene[223], the model predicts therefore a strong p-doping of graphene in oxygenated water across the whole range of pH (Figure 5.1 right panel). While this model highlights the presence of a driving force for doping with the proton concentration, the results with u-graphene indicate no or little doping dependency with pH, which is inconsistent with the model. The results suggest that the graphene itself does not react with the O_2/H_2O redox couple, at least during the course of the experiment. That is, the u-graphene in solution appears to stay in an out-of-equilibrium state. In fact, previous work from our group has already shown that the charge transfer kinetics takes months before reaching equilibrium[217]. In our experiments, only few minutes elapse between each Raman measurement, which seems far from being enough for achieving equilibrium. Because graphene bares no

functional groups and considering that a total of four electrons are needed for this reaction, the surface inertness appears to provide no anchoring for the intermediate species of the reaction. As evidenced by the relatively low intensity of D band, the u-graphene used in these experiments is relatively clean and free of surface groups, which explains why it is a poor redox system for pH sensing.

Pt/PtO redox pair solves the surface problem of u-graphene because it can catalyze the redox reaction at its surface and the surface produces stable reduction/oxidation intermediates. When in direct contact with the graphene surface, the Pt/PtO also allows free charge transfer to the graphene until equilibrium is reached between the graphene, the Pt/PtO system and the buffer solution. As discussed in Chapter 4, the Pt coating enables the following redox reaction[224]: $\mathrm{PtO} + 2\mathrm{H}^+ + 2\mathrm{e}^-(\mathrm{Pt}-\mathrm{graphene}) \rightleftharpoons \mathrm{PtO} + \mathrm{H_2O}$, which can provide a potential energy shift with pH as: $E_{\mathrm{abs,Pt/PtO}} = -5.32 + 0.059\,\mathrm{pH}$ (in eV). The energy level or Fermi energy of the Pt/PtO at different pH values is between -5.26 eV (pH=1) and -4.62 eV (pH=12), which lies below the graphene work function of 4.6 eV. That is, an acidic solution makes graphene strongly p-doped, whereas a basic solution favors intrinsic graphene, these predictions are quite consistent with the results in Figure 5.3.

Because the shift of the Raman G-band can probe the carrier concentration, $n(E_F)$, in monolayer graphene, one can use calibrated experiments to estimate the carrier concentration in Pt-graphene for each pH experiment. Based on experiments with graphene FETs, Das et al. estimated using the device capacitance a relationship between the G-band position and $n(E_F)$ for monolayer graphene[141]. assuming a linear correlation between the Das results and the pH results in Figure 5.3, we can superpose the two experiments together on the same graph as shown in Figure 5.4. Interestingly, this comparison shows a fair agreement, suggesting that there is a linear relation between the pH and dopant concentration. Hence, one can use this comparison to determine the Fermi energy in graphene for each $n(E_F)$ using $n(E_F) = sgn(E_F)\ \frac{{E_F}^2}{\pi(\hbar \upsilon_F)^2}$, where υ_F is the Fermi velocity (10^6 m/s) and $sgn(E_F)$ is the sign of the Fermi level (negative for hole doping). The resulting values (black curve) are reported in Figure 5.3b, which compares again the Das results with the experimental results of the Raman G-band shifts vs. pH (blue) for Pt-graphene. Because of the fortuitous linear relationship, one can directly compare these results to estimate the Fermi level position for each pH value of our Pt-graphene experiments. Interestingly, the model, which

predicts a slope of 59 mV/pH for the Nernstian limit (red dotted line), is in a very good agreement with the Raman results obtained here (blue points). It is therefore reasonable to conclude from this simple model that the Pt-graphene surface is at or near equilibrium with the solution. The Raman sensing behavior of Pt-graphene with pH indicates a Nernstian behavior.

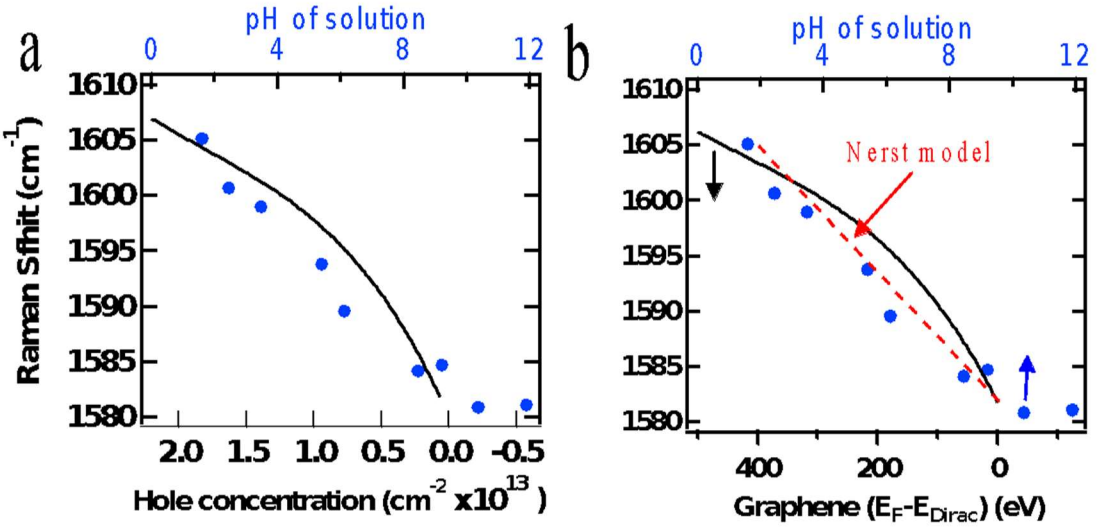

Figure 5.4. Comparison of the Pt-graphene Raman results with pH with the Nernstian model presented. (a) Raman shift of the G-band with pH (blue data points) compared with the carrier concentration according to a fit of the results from Das and al. (black line)[141]. (b) Calculation of the Fermi level position for each Raman shift taken in panel (a) superimposed with the G-band position results from this study with the pH of buffer solutions.

5.3 Conclusion

We characterized the Raman response of graphene coated with platinum in the regions of the G- and D-bands in buffer solutions over a broad range of pH values between 1 to 12. The Raman results are compared to that of uncoated graphene in the same conditions. The uncoated graphene shows small perturbation vs. pH, whereas the Raman spectrum of Platinum decorated graphene undergoes a significant transformation with pH. Increasing the pH induces a linear red shift of both the G- and D-band positions, a phenomenon ascribed to a charge transfer doping. The results are consistent with a redox reaction involving the Pt/PtO redox pair and the proton in the solution. The results indicate that the Pt-graphene electrode is p-doped in acidic pH. Increasing the pH of the solution gradually reduces this hole doping and the graphene becomes intrinsic at pH=12. The linear response observed here in Raman is compared with literature data on graphene FETs. The model shows that the Pt-graphene system follows a Nernstian behavior.

While uncoated graphene is to be a bad redox couple for pH measurements, the platinum coated graphene electrode provides a direct measure of the pH of the solution. This work presents Pt coated graphene as a convenient reference electrode to sense optically the pH of solutions across a broad range between 1 and 12. These results pave the way for development of graphene based optical pH sensors requiring no electrical contact.

Chapter 6: General Conclusions

By making use of carbon nanomaterials and a non-destructive optical technique, we designed and developed an optical pH sensor capable of referenced pH measurements on a surface. We have explored the concept of the use of carbon nanomaterials for referencing the potential and made a proof of concept that aimed to address important limitations of conventional pH meters and other optical techniques, such as a miniaturization of the sensor, referenced pH measurements across the full pH range, albeit slightly dependent on the concentration of the analytes. This thesis has examined two different carbon nanomaterials: single walled carbon nanotubes and graphene as reporters of the solution pH. We prepared platinum decorated SWCNTs and graphene samples and integrated the hybrids into a Raman pH setup. The Raman measurements were done on these hybrids in different buffer solutions of pH values between 1 and 12. Raman experiments on the hybrids made of Pt/PtO attached to the reporters show that a red shift of the G-band of the hybrid material was generally measured with increasing pH and the position was referenced to evaluate the pH of unknown solutions.

The achievements of this thesis could be described into two main parts:

A) pH sensing from single-walled carbon nanotubes

We chose single-walled carbon nanotubes to design the first pH sensor because of their specific and attractive characteristics, which include strong Raman signal, high surface to volume ratio, insensitivity to pH, and ease of chemical functionalization to include redox-active species. These results showed a clear dependency of the Raman fingerprint peaks of the SWCNTs, the G-band and D-band, which is consistent with a doping of the SWCNTs.

We have investigated the dependency of the fingerprint Raman peak (G-band) of plasma torch SWCNTs (diameters between 0.9 nm and 1.5 nm) on the pH value. An excitation wavelength of λ_{ex} = 633 nm was selected to specifically target a Raman resonance of the metallic nanotubes in our sample.

The results showed that uncoated SWCNTs are not capable of forming good redox couples with their oxidized forms and gave only slow charge transfer kinetics. However, the platinum coated SWCNTs showed much improved results, which were shown to compete against the O_2/H_2O redox

pair already present in the solution. Uncoated (oxidized) SWCNTs nevertheless showed a slight red shift in the position of the G-band with changing pH, giving only a sluggish response.

The G+ mode, first peak at the highest Raman shift, is the least affected by pH whereas the G- mode and the G_f mode (low energy peak) of metallic SWCNTs are found to be the most sensitive to pH. The Raman response of semiconducting SWCNTs was also explored, but the shift of their response was found to be weak. To maximize the signal, we explored SWCNTs prepared by laser ablation method because of their narrow diameter distribution (1.1 nm – 1.5 nm), which allows a specific detection of the metallic SWCNTs in Raman measurements at 633 nm wavelength excitation. A much stronger pH-induced response was found for these metallic SWCNTs when placed in contact with Pt.

By considering the energy level of the two redox couples (O_2/H_2O and Pt/PtO) and Fermi level of SWCNTs, a model was presented and shown to describe the doping of uncoated and Pt-coated SWCNTs. This model for the Pt/PtO redox pair was shown to predict a p-doping of the SWCNTs in acidic solution and a quasi undoped state in basic solution. An inconsistency between the model and the experimental findings was noted and investigated using buffer solutions of different ionic strengths with Pt-coated SWCNTs. The results showed that the ionic strength impacts weakly the pH response, as evidenced by the parallel slopes of the G- and G_f modes. Decreasing the ionic strength generally reduces the doping level, which is ascribed to a reduced charge screening. Surprisingly, a reduction of the ionic strength, i.e., lower screening, reduces the doping state towards a position predicted by the model. The discrepancy between the observed Raman shifts and the presented model remains, however, a point to clarify.

Our previous results showed a high sensitivity of Pt-coated SWCNT sensor to the local pH. We investigated the potential errors introduced by the substrate to the pH measurements. Two kinds of surfaces were prepared: the parlyene-C deposited on an oxidized silicon wafer and an aminoalkyl-silanized oxidized silicon wafer and these were compared with an oxidized silicon substrate without any modification on the surface. The results demonstrated some deviation in basic solutions, which is ascribed to different densities of functional groups (silanols, protonated and deprotonated silanols). The experiment showed that the measurement is also influenced by the local charges, which induces additional shifts of the electrochemical potential in the bulk of the solution.

To solve the potential problem of uniformity in the preparation of the Pt-SWCNTs, we developed a synthesis procedure to prepare SWCNTs uniformly coated with Pt nanoparticles (Pt_N-SWCNTs) and assembled thin films of these Pt_N-SWCNTs for pH sensing. The Pt_N-SWCNTs provided the expected strong Raman response with pH, namely a shift of the G- mode by more than 7 cm^{-1} across the pH values between 2 and 12. As a proof of the feasibility of the Pt_N-SWCNT pH sensor for analytical measurements, we prepared three different Pt_N-SWCNT samples and exposed them to solutions of different pH. Test solutions measured by a conventional pH meter equipped with a combined glass electrode were used to determine an accuracy of the Raman-based measurements of ±700 mpH in basic solution and ±500 mpH in acidic solution. The precision of the remote pH sensor remains high across the full range of pH. The difference in accuracy for the acidic and basic solutions is ascribed to the response of the silanized surface.

The Pt_N-SWCNT-based Raman sensor in its current version shows a lower accuracy compared to conventional (electrode-based) pH meters. However, it has the advantage of operating optically without physical electrodes. The sensor has nanoscale dimensions and provides non-specific signals that can be mixed with other signals (contaminants, biomaterials, support, etc.) and a slight dependency on the concentration of the analyte.

To improve the response, we investigated the use of sorted samples of pure (>95%) metallic SWCNTs coated with nanoparticles of platinum, thanks to a one-pot synthesis of the Pt_N-m-SWCNTs hybrids. The results demonstrated a larger shift of the G- mode (10 cm^{-1}) compared to the Pt_N-SWCNTs (6 cm^{-1}) , a steeper slope (-1.02 ± 0.03 cm^{-1}/pH unit compared to -0.70 ± 0.02 cm^{-1}/pH unit for unsorted Pt_N-SWCNTs) and a reduced broadening of the G-band. The action of the platinum nanoparticles was compared with that of palladium and ruthenium (Pd_N-MSWCNTs and Ru_N-MSWCNTs). The Pd_N-MSWCNTs did not show any Raman shifting with pH, while the Ru_N-MSWCNTs demonstrated a clear Raman shifting but limited to the acidic region. These findings indicate that platinum is the best choice among these three metals.

B) pH sensing with graphene

The second achievement of this thesis is related to the results of Raman-pH sensing using graphene. Graphene is the fundamental building block of all carbon allotropes with its own unique

properties. Previous research encouraged us to investigate the Raman-pH dependency of graphene. We characterized the spectral response of platinum coated graphene to pH across a broad range of pH from 1 to 12 and compared it to that of uncoated graphene. The uncoated graphene sample demonstrated small perturbations of the Raman spectra compared to the platinum-coated graphene. A significant transformation of the Raman spectra with pH was measured with the Pt-graphene system in the region of the G-band. Similarly to the SWCNT hybrids, the phenomenon is ascribed to charge transfer doping between the Pt/PtO redox pair and the graphene electrode.

The shifting in position of the G-band in Pt-graphene (25.5 cm^{-1}) was more than two times larger than Pt_N-m-SWCNTs (10 cm^{-1}) and the slope was steeper (-2.4 ± 0.2 cm^{-1}/pH unit compared to -1.02 ± 0.03 cm^{-1}/pH unit). The increased sensitivity is related to the unique electronic structure of graphene. The highest Raman intensity of the SWCNTs makes overall better sensors, but of lower accuracy.

Nonetheless, our findings have the potential to impact the design of optical carbon-based pH sensors. These sensors can be miniaturized and are effective over the entire pH range, which would make them attractive in a multitude of applications such as in the food industry or in biomedical applications, to detect local changes in pH at the small scale.

Future research could continue to solve the Raman intensity problem of graphene samples using graphene nanoflakes. Next experiments will examine the accuracy of the pH sensor made with graphene and this will allow a direct comparison with the performance of pH sensors based on SWCNTs. Finally, we plan to prepare a prototype of the pH sensor having the best performances and adapt the sensor to industrial needs.

REFERENCES

1. Boyle, R., *Experimenta et considerationes de coloribus* (London, **1663**).

2. Arrhenius, S., On the dissociation of substances dissolved in water. *Z. Phys. Chem.* **1887,** *1*, 631.

3. Lesney, M., A basic history of acid-from Aristotle to Arnold. *J. Am. Chem. Soc.* **2003,** *12*, 47-50.

4. Macinnes, D. A., Criticism of a Definition of pH. *Science* **1948,** *108* (2816), 693.

5. Lipczynska-Kochany, E., Effect of climate change on humic substances and associated impacts on the quality of surface water and groundwater: A review. *Sci. Total Environ.* **2018,** *640*, 1548-1565.

6. Yidana, S. M.; Yidana, A., Assessing water quality using water quality index and multivariate analysis. *Environ. Earth Sci.* **2010,** *59* (7), 1461-1473.

7. Riché, E.; Carrié, A.; Andin, N.; Mabic, S., High-purity water and pH. *Am. Lab.* **2006,** *38* (13), 22.

8. Sumari, S. M.; Muhamad-Darus, F.; Kantasamy, N. In *Rainwater characterization at Global Atmospheric Watch in Danum Valley, Sabah*, 2010 International Conference on Science and Social Research (CSSR 2010), IEEE: 2010; pp 479-484.

9. Likens, G. E.; Bormann, F. H., Acid rain: a serious regional environmental problem. *Science* **1974,** *184* (4142), 1176-1179.

10. Warudkar, G.; Dorle, S. In *Review on sensing the fertility characteristics of agriculture soils*, 2016 International Conference on Information Communication and Embedded Systems (ICICES), IEEE: 2016; pp 1-6.

11. Andrés-Bello, A.; Barreto-Palacios, V.; García-Segovia, P.; Mir-Bel, J.; Martínez-Monzó, J., Effect of pH on color and texture of food products. *Food Eng. Rev.* **2013,** *5* (3), 158-170.

12. Schwartz, S.; Von Elbe, J., Kinetics of chlorophyll degradation to pyropheophytin in vegetables. *J. Food Sci.* **1983,** *48* (4), 1303-1306.

13. Tijskens, L.; Barringer, S.; Biekman, E., Modelling the effect of pH on the colour degradation of blanched broccoli. *Innov Food Sci Emerg Technol **2001,** 2 (4), 315-322.*

14. Dziezak, J. D., Acidulants: ingredients that do more than meet the acid test. *Food Sci. Technol.* **1990,** *44* (1), 76-83.

15. Doesburg, J., Relation between the behaviour of pectic substances and changes in firmness of horticultural products during heating. *Qual. Plant. Mater. Veg.* **1961,** *8* (2), 115-129.

16. Pérez, M. L.; Escalona, H.; Guerrero, I., Effect of calcium chloride marination on calpain and quality characteristics of meat from chicken, horse, cattle and rabbit. *Meat Sci.* **1998,** *48* (1-2), 125-134.

17. Koohmaraie, M., Muscle proteinases and meat aging. *Meat Sci.* **1994,** *36* (1-2), 93-104.

18. Schneider, L. A.; Korber, A.; Grabbe, S.; Dissemond, J., Influence of pH on wound-healing: a new perspective for wound-therapy? *Arch. Dermatol.* **2007,** *298* (9), 413-420.

19. Schreml, S.; Szeimies, R. M.; Karrer, S.; Heinlin, J.; Landthaler, M.; Babilas, P., The impact of the pH value on skin integrity and cutaneous wound healing. *J. Eur. Acad. Dermatol. Venereol.* **2010,** *24* (4), 373-378.

20. Sawyer, R. G.; Spengler, M. D.; Adams, R. B.; Pruett, T. L., The peritoneal environment during infection. The effect of monomicrobial and polymicrobial bacteria on pO_2 and pH. *Ann. Surg.* **1991,** *213* (3), 253.

21. Benomar, S.; Lansdon, P.; Bender, A. M.; Peterson, B. R.; Chandler, J. R.; Ackley, B. D., The C. elegans CHP1 homolog, pbo-1, functions in innate immunity by regulating the pH of the intestinal lumen. *PLoS Pathog.* **2020,** *16* (1), e1008134.

22. Swietach, P.; Vaughan-Jones, R. D.; Harris, A. L.; Hulikova, The chemistry, physiology and pathology of pH in cancer. *Phil. Trans. R. Soc. B* **2014,** *369* (1638), 20130099.

23. White, K. A.; Grillo-Hill, B. K.; Barber, D. L., Cancer cell behaviors mediated by dysregulated pH dynamics at a glance. *J. Cell Sci.* **2017,** *130* (4), 663-669.

24. Bard, A. J.; Faulkner, L. R. *Electrochemical Methods: Fundamentals and Applications*, 2nd ed.; John Wiley & Sons: New York, **2001**.

25. Sawyer, D. T.; Sobkowiak, A.; Roberts, J. L., Jr. *Electrochemistry for Chemists*, 2nd ed.; John Wiley and Sons: New York, **1995**.

26. Morf, W. E. *The Principles of Ion-Selective Electrodes and of Membrane Transport*; Elsevier: New York, **1981**.

27. Bergveld, P., Thirty years of ISFETOLOGY: What happened in the past 30 years and what may happen in the next 30 years. *Sens. Actuators B Chem.* **2003,** *88* (1), 1-20.

28. Lee, C.-S.; Kim, S. K.; Kim, M., Ion-sensitive field-effect transistor for biological sensing. *Sensors* **2009,** *9* (9), 7111-7131.

29. Jimenez-Jorquera, C.; Orozco, J.; Baldi, A., ISFET based microsensors for environmental monitoring. *Sensors* **2010,** *10* (1), 61-83.

30. Aßmann, S.; Frank, C.; Körtzinger, A., Spectrophotometric high-precision seawater pH determination for use in underway measuring systems. *Ocean Sci.* **2011,** *7* (5), 597-607.

31. Desmond, D.; Lane, B.; Alderman, J.; Glennon, J.; Diamond, D.; Arrigan, D., Evaluation of miniaturised solid state reference electrodes on a silicon-based component. *Sens. Actuators B Chem.* **1997,** *44* (1-3), 389-396.

32. Dickinson, J. W.; Bromley, M.; Andrieux, F. P.; Boxall, C., Fabrication and characterisation of the graphene ring micro electrode (GRiME) with an integrated, concentric Ag/AgCl reference electrode. *Sensors* **2013,** *13* (3), 3635-3651.

33. Zhou, J.; Ren, K.; Zheng, Y.; Su, J.; Zhao, Y.; Ryan, D.; Wu, H. J. E., Fabrication of a microfluidic Ag/AgCl reference electrode and its application for portable and disposable electrochemical microchips. *Electrophoresis* **2010,** *31* (18), 3083-3089.

34. Münzer, A.; Melzer, K.; Heimgreiter, M.; Scarpa, G., Random CNT network and regioregular poly (3-hexylthiophen) FETs for pH sensing applications: A comparison. *Biochim. Biophys. Acta, Gen. Subj.* **2013,** *1830* (9), 4353-4358.

35. Back, J. H.; Shim, M., pH-dependent electron-transport properties of carbon nanotubes. *J. Phys. Chem. B* **2006,** *110* (47), 23736-41.

36. Tang, Y.; Kotchey, G. P.; Vedala, H.; Star, A., Electrochemical detection with platinum decorated carbon nanomaterials. *Electroanalysis* **2011,** *23* (4), 870-877.

37. Zhao, Z.; Tu, H.; Kim, E. G.; Sloane, B. F.; Xu, Y., A flexible Ag/AgCl micro reference electrode based on a parylene tube structure. *Sens. Actuators, B* **2017,** *247*, 92-97.

38. Sophocleous, M.; Atkinson, J. K., A review of screen-printed silver/silver chloride (Ag/AgCl) reference electrodes potentially suitable for environmental potentiometric sensors. *Sens. Actuators, A* **2017,** *267*, 106-120.

39. Shibata, M.; Kato, M.; Iwamoto, Y.; Nomura, S.; Kakiuchi, T., Potentiometric determination of pH values of dilute sulfuric acid solutions with glass combination electrode equipped with ionic liquid salt bridge. *J. Electroanal. Chem.* **2013,** *705*, 81-85.

40. Fakih, I.; Mahvash, F.; Siaj, M.; Szkopek, T., Sensitive Precise pH Measurement with Large-Area Graphene Field-Effect Transistors at the Quantum-Capacitance Limit. *Phys. Rev. Applied* **2017,** *8* (4), 044022.

41. Kurzweil, P., Metal oxides and ion-exchanging surfaces as pH sensors in liquids: State-of-the-art and outlook. *Sensors* **2009,** *9* (6), 4955-4985.

42. Głab, S.; Hulanicki, A.; Edwall, G.; Ingman, F., Metal-metal oxide and metal oxide electrodes as pH sensors. *Crit. Rev. Anal. Chem.* **1989,** *21* (1), 29-47.

43. Chang, P. C.; Chen, H. Y.; Ye, J. S.; Sheu, F. S.; Lu, J. G., Vertically aligned antimony nanowires as solid-state pH sensors. *ChemPhysChem* **2007,** *8* (1), 57-61.

44. Kolthoff, I.; Hartong, B., The antimony electrode as an indicator for hydrogen ions and its application in potentiometric titrations of acids and bases. *Rec.Trav.Chim.Pays Bas* **1925,** *44* (2), 113-120.

45. Xu, K.; Zhang, X.; Hou, K.; Geng, M.; Zhao, L., The effects of antimony thin film thickness on antimony pH electrode coated with nafion membrane. *J. Electrochem. Soc.* **2016,** *163* (8), B417.

46. Fog, A.; Buck, R. P., Electronic semiconducting oxides as pH sensors. *Sens. Actuators* **1984,** *5* (2), 137-146.

47. Kreider, K. G.; Tarlov, M. J.; Cline, J. P., Sputtered thin-film pH electrodes of platinum, palladium, ruthenium, and iridium oxides. *Sens. Actuators, B* **1995,** *28* (3), 167-172.

48. Qin, Y.; Kwon, H.-J.; Howlader, M. M.; Deen, M. J., Microfabricated electrochemical pH and free chlorine sensors for water quality monitoring: recent advances and research challenges. *RSC Adv.* **2015,** *5* (85), 69086-69109.

49. Ghoneim, M.; Nguyen, A.; Dereje, N.; Huang, J.; Moore, G.; Murzynowski, P.; Dagdeviren, C., Recent progress in electrochemical pH-sensing materials and configurations for biomedical applications. *Chem. Rev.* **2019,** *119* (8), 5248-5297.

50. Roef, P., Attention focuses on optical fibre biosensors. *Sens. Rev.* **1987,** *7* (3), 127-132.

51. Wencel, D.; Abel, T.; McDonagh, C., Optical chemical pH sensors. *Anal. Chem.* **2014,** *86* (1), 15-29.

52. Lin, J., Recent development and applications of optical and fiber-optic pH sensors. *Trends Anal. Chem.* **2000,** *19* (9), 541-552.

53. Wolfbeis, O. S., Probes, sensors, and labels: why is real progress slow? *Angew. Chem. Int. Ed.* **2013,** *52* (38), 9864-9865.

54. Salis, A.; Monduzzi, M., Not only pH. Specific buffer effects in biological systems. *Curr. Opin. Colloid Interface Sci.* **2016,** *23*, 1-9.

55. Wang, J.; Long, L.; Xiao, X., A fast-responsive fluorescent probe for sulfite and its bioimaging. *Luminescence* **2016,** *31* (3), 775-781.

56. Ruan, C.; Zeng, K.; Grimes, C. A., A mass-sensitive pH sensor based on a stimuli-responsive polymer. *Anal. Chim. Acta* **2003,** *497* (1-2), 123-131.

57. Qi, J.; Liu, D.; Liu, X.; Guan, S.; Shi, F.; Chang, H.; He, H.; Yang, G., Fluorescent pH sensors for broad-range pH measurement based on a single fluorophore. *Anal. Chem.* **2015,** *87* (12), 5897-5904.

58. Ferrari, L.; Rovati, L.; Fabbri, P.; Pilati, F. J. S., Disposable fluorescence optical pH sensor for near neutral solutions. *Sensors* **2013,** *13* (1), 484-499.

59. Capel-Cuevas, S.; Cuéllar, M.; de Orbe-Payá, I.; Pegalajar, M.; Capitán-Vallvey, L. J. A. c. a., Full-range optical pH sensor array based on neural networks. *Microchem. J.* **2011,** *97* (2), 225-233.

60. Capel-Cuevas, S.; Cuéllar, M.; de Orbe-Payá, I.; Pegalajar, M.; Capitán-Vallvey, L. J. A. c. a., Full-range optical pH sensor based on imaging techniques. *Anal. Chim. Acta* **2010,** *681* (1-2), 71-81.

61. Tormo, L.; Bustamante, N.; Colmenarejo, G.; Orellana, G., Can luminescent Ru (II) polypyridyl dyes measure pH directly? *Anal. Chem.* **2010,** *82* (12), 5195-5204.

62. Burns, A.; Ow, H.; Wiesner, U., Fluorescent core–shell silica nanoparticles: towards "Lab on a Particle" architectures for nanobiotechnology. *Chem. Soc. Rev.* **2006,** *35* (11), 1028-1042

63. Melucci, M.; Durso, M.; Zambianchi, M.; Treossi, E.; Xia, Z.-Y.; Manet, I.; Giambastiani, G.; Ortolani, L.; Morandi, V.; De Angelis, F., Graphene–organic hybrids as processable, tunable platforms for pH-dependent photoemission, obtained by a new modular approach. *J. Mater. Chem.* **2012,** *22* (35), 18237-18243.

64. Gorji, M.; Sadeghianmaryan, A.; Rajabinejad, H.; Nasherolahkam, S.; Chen, X., Development of highly pH-sensitive hybrid membranes by simultaneous electrospinning of amphiphilic nanofibers reinforced with graphene oxide. *J. Funct. Biomater.* **2019,** *10* (2), 23.

65. Yan, L.; Chang, Y.-N.; Yin, W.; Liu, X.; Xiao, D.; Xing, G.; Zhao, L.; Gu, Z.; Zhao, Y. J. P. C. C. P., Biocompatible and flexible graphene oxide/upconversion nanoparticle hybrid film for optical pH sensing. *Phys. Chem. Chem. Phys.* **2014,** *16* (4), 1576-1582.

66. Hong, G.; Diao, S.; Antaris, A. L.; Dai, H., Carbon nanomaterials for biological imaging and nanomedicinal therapy. *Chem. Rev.* **2015,** *115* (19), 10816-10906.

67. Thakur, M.; Kumawat, M. K.; Srivastava, R., Multifunctional graphene quantum dots for combined photothermal and photodynamic therapy coupled with cancer cell tracking applications. *RSC adv.* **2017,** *7* (9), 5251-5261.

68. Kumawat, M. K.; Thakur, M.; Gurung, R. B.; Srivastava, R., Graphene quantum dots from mangifera indica: application in near-infrared bioimaging and intracellular nanothermometry. *ACS Sustain. Chem. Eng.* **2017,** *5* (2), 1382-1391.

69 Kumawat, M. K.; Thakur, M.; Gurung, R. B.; Srivastava, R., Graphene quantum dots for cell proliferation, nucleus imaging, and photoluminescent sensing applications. *Sci. Rep.* **2017,** *7* (1), 1-16.

70. Paek, K.; Yang, H.; Lee, J.; Park, J.; Kim, B. J. J. A. N., Efficient colorimetric pH sensor based on responsive polymer–quantum dot integrated graphene oxide. *Acs Nano* **2014,** *8* (3), 2848-2856.

71. Kulkarni, M. V.; Kale, B. B., Studies of conducting polyaniline (PANI) wrapped-multiwalled carbon nanotubes (MWCNTs) nanocomposite and its application for optical pH sensing. *Sens. Actuators, B* **2013,** *187*, 407-412.

72. Kaempgen, M.; Roth, S., Transparent and flexible carbon nanotube/polyaniline pH sensors. *J. Electroanal. Chem.* **2006,** *586* (1), 72-76.

73. Salem, D. P.; Gong, X.; Liu, A. T.; Koman, V. B.; Dong, J.; Strano, M. S., Ionic strength-mediated phase transitions of surface-adsorbed DNA on single-walled carbon nanotubes. *J. Am. Chem. Soc.* **2017,** *139* (46), 16791-16802.

74. Nakayama-Ratchford, N.; Bangsaruntip, S.; Sun, X.; Welsher, K.; Dai, H., Noncovalent functionalization of carbon nanotubes by fluorescein− polyethylene glycol: supramolecular conjugates with pH-dependent absorbance and fluorescence. *J. Am. Chem. Soc.* **2007,** *129* (9), 2448-2449.

75. Chen, P.; Wang, Z.; Zong, S.; Chen, H.; Zhu, D.; Zhong, Y.; Cui, Y., A wide range optical pH sensor for living cells using Au@ Ag nanoparticles functionalized carbon nanotubes based on SERS signals. *Anal. Bioanal. Chem.* **2014,** *406* (25), 6337-6346.

76. Zhao, L.; Shingaya, Y.; Tomimoto, H.; Huang, Q.; Nakayama, T., Functionalized carbon nanotubes for pH sensors based on SERS. *J. Mater. Chem.* **2008,** *18* (40), 4759-4761.

77. Paulus, G. L.; Nelson, J. T.; Lee, K. Y.; Wang, Q. H.; Reuel, N. F.; Grassbaugh, B. R.; Kruss, S.; Landry, M. P.; Kang, J. W.; Vander Ende, E., A graphene-based physiometer array for the analysis of single biological cells. *Sci. Rep.* **2014,** *4*, 6865.

78. Camerlingo, C.; Verde, A.; Manti, L.; Meschini, R.; Delfino, I.; Lepore, M., Graphene-based Raman spectroscopy for pH sensing of X-rays exposed and unexposed culture media and cells. *Sensors* **2018,** *18* (7), 2242.

79. Camerlingo, C.; Di Meo, G.; Lepore, M.; Lisitskiy, M.; Poli, A.; Portaccio, M.; Romano, I.; Di Donato, P., Graphene-Based and Surface-Enhanced Raman Spectroscopy for Monitoring the Physio-Chemical Response of Thermophilic Bacterial Spores to Low Temperatures Exposure. *Sensors* **2020,** *20* (15), 4150.

80. Zuccaro, L.; Kern, K.; Balasubramanian, K., Identifying chemical functionalization on individual carbon nanotubes and graphene by local vibrational fingerprinting. *ACS Nano* **2015,** *9* (3), 3314-3323.

81. Mažeikienė, R.; Tomkutė, V.; Kuodis, Z.; Niaura, G.; Malinauskas, A. J. V. S., Raman spectroelectrochemical study of polyaniline and sulfonated polyaniline in solutions of different pH. *Vib. Spectrosc.* **2007,** *44* (2), 201-208.

82. Kim, W.; Cho, S.; Lee, J. S., Comparative Study on the Effect of Protonation Control for Resistive Gas Sensor Based on Close-Packed Polypyrrole Nanoparticles. *Appl. Sci.* **2020,** *10* (5), 1850.

83. Andreas, H., The era of carbon allotropes. *Nat. Mater.* **2010,** *9*, 868.

84. Jorio, A.; Dresselhaus, G.; Dresselhaus, M. S., *Carbon nanotubes: advanced topics in the synthesis, structure, properties and applications*. Springer Science & Business Media: 2007; Vol. 111.

85. Kioto, H.; Heath, J.; O'Brien, S.; Curl, R.; Smalley, R., C 60: Buckminsterfullerene. *Nature* **1985,** *318*, 162-163.

86. Iijima, S., Helical microtubules of graphitic carbon. *Nature* **1991,** *354* (6348), 56-58.

87. Novoselov, K. S.; Geim, A. K.; Morozov, S. V.; Jiang, D.; Zhang, Y.; Dubonos, S. V.; Grigorieva, I. V.; Firsov, A. A., Electric field effect in atomically thin carbon films. *science* **2004,** *306* (5696), 666-669.

88. Novoselov, K. S.; Geim, A., The rise of graphene. *Nat. Mater.* **2007,** *6* (3), 183-191.

89. Gao, W.; Kono, J., Science and applications of wafer-scale crystalline carbon nanotube films prepared through controlled vacuum filtration. *R. Soc. Open Sci.* **2019,** *6* (3), 181605.

90. Cui, J.; Yang, D.; Zeng, X.; Zhou, N.; Liu, H. J. N., Recent progress on the structure separation of single-wall carbon nanotubes. *Nanotechnology* **2017,** *28* (45), 452001.

91. Charlier, J.-C.; Blase, X.; Roche, S., Electronic and transport properties of nanotubes. *Rev. Mod. Phys.* **2007,** *79* (2), 677.

92. Saito, R.; Dresselhaus, G.; Dresselhaus, M. S. *Physical Properties of Carbon Nanotubes*; Imperial College Press: London, U.K., **1998**.

93. Jorio, A. *Raman Spectroscopy in Graphene Related Systems*; WileyVCH: Weinheim, Germany, 2011.

94. Cooper, D. R.; D'Anjou, B.; Ghattamaneni, N.; Harack, B.; Hilke, M.; Horth, A.; Majlis, N.; Massicotte, M.; Vandsburger, L.; Whiteway, E.; Yu, V. Experimental Review of Graphene. ISRN *Condens. Matter Phys*. 2012, 2012, 501686.

95. Weiss, N. O.; Zhou, H. H.; Liao, L.; Liu, Y.; Jiang, S.; Huang, Y.; Duan, X. F. Graphene: An Emerging Electronic Materials. *Adv. Mater*. 2012, 24, 5776−5776.

96. Samsonidze, G. G.; Saito, A. R.; Jorio, D. A.; Pimenta, E.; Souza, F.; Grüneis, F. A.; Dresselhaus, D. G.; Dresselhausa, M., The concept of cutting lines in carbon nanotube science. *J. Nanosci. Nanotechnol.* **2003,** *3* (6), 431-458.

97. Tanaka, K., Iijima, S., Eds. Carbon Nanotubes and Graphene, 2nd ed.; Elsevier, 2014.

98. Tian, Y.; Jiang, H.; Laiho, P.; Kauppinen, E. I., Validity of measuring metallic and semiconducting single-walled carbon nanotube fractions by quantitative Raman spectroscopy. *Anal. Chem.* **2018,** *90* (4), 2517-2525.

99. Hersam, M. C., Progress towards monodisperse single-walled carbon nanotubes. *Nat. Nanotechnol.* **2008,** *3* (7), 387-394.

100. Nanot, S.; Hároz, E. H.; Kim, J. H.; Hauge, R. H.; Kono, J., Optoelectronic Properties of Single-Wall Carbon Nanotubes. *Adv. Mater.* **2012,** *24* (36), 4977-4994.

101. Dresselhaus, M.; Dresselhaus, G.; Jorio, A.; Souza Filho, A.; Pimenta, M.; Saito, R., Single nanotube Raman spectroscopy. *Acc. Chem. Res.* **2002,** *35* (12), 1070-1078.

102. Kuzmany, H.; Plank, W.; Hulman, M.; Kramberger, C.; Grüneis, A.; Pichler, T.; Peterlik, H.; Kataura, H.; Achiba, Y., Determination of SWCNT diameters from the Raman response of the radial breathing mode. *Eur. Phys. J. B* **2001,** *22* (3), 307-320.

103. Rao, A. M.; Richter, E.; Bandow, S.; Chase, B.; Eklund, P.; Williams, K.; Fang, S.; Subbaswamy, K.; Menon, M.; Thess, A., Diameter-selective Raman scattering from vibrational modes in carbon nanotubes. *Science* **1997,** *275* (5297), 187-191.

104. Kataura, H.; Kumazawa, Y.; Maniwa, Y.; Umezu, I.; Suzuki, S.; Ohtsuka, Y.; Achiba, Y., Optical properties of single-wall carbon nanotubes. *Synth. Met.* **1999,** *103* (1-3), 2555-2558.

105. Weisman, R. B.; Bachilo, S. M., Dependence of optical transition energies on structure for single-walled carbon nanotubes in aqueous suspension: an empirical Kataura plot. *Nano Lett.* **2003,** *3* (9), 1235-1238.

106. Cataldo, S.; Salice, P.; Menna, E.; Pignataro, B. J. E., Carbon nanotubes and organic solar cells. *Energy Environ. Sci.* **2012,** *5* (3), 5919-5940.

107. Alon, O. E., Number of Raman-and infrared-active vibrations in single-walled carbon nanotubes. *Phys. Rev. B* **2001,** *63* (20), 201403.

108. Barros, E.; Jorio, A.; Samsonidze, G.; Capaz, R., Filho, AGS; Dresselhaus, G.; Dresselhaus, MS. *Phys. Rep* **2006,** *431*, 261-302.

109. Dresselhaus, M. S.; Dresselhaus, G.; Saito, R.; Jorio, A., Raman spectroscopy of carbon nanotubes. *Phys. Rep.* **2005,** *409* (2), 47-99.

110. Das, R. S.; Agrawal, Y., Raman spectroscopy: recent advancements, techniques and applications. *Vib. Spectrosc.* **2011,** *57* (2), 163-176.

111. Gardiner, D. J. *Practical Raman Spectroscopy*; Springer-Verlag: Berlin, 1989**.**

112. Long, D. A. *In the Raman Effect*; John Wiley & Sons, Ltd.; New York, 2002.

113. Malard, L.; Pimenta, M. A.; Dresselhaus, G.; Dresselhaus, M., Raman spectroscopy in graphene. *Phys. Rep.* **2009,** *473* (5-6), 51-87.

114. Wang, Z.; Wu, S.; Ciacchi, L. C.; Wei, G., Graphene-based nanoplatforms for surface-enhanced Raman scattering sensing. *Analyst* **2018,** *143* (21), 5074-5089.

115. Lazzeri, M.; Attaccalite, C.; Wirtz, L.; Mauri, F., Impact of the electron-electron correlation on phonon dispersion: Failure of LDA and GGA DFT functionals in graphene and graphite. *Phys. Rev. B* **2008,** *78* (8), 081406.

116. Bachilo, S. M.; Balzano, L.; Herrera, J. E.; Pompeo, F.; Resasco, D. E.; Weisman, R. B., Narrow (n, m)-distribution of single-walled carbon nanotubes grown using a solid supported catalyst. *J. Am. Chem. Soc.* **2003,** *125* (37), 11186-11187.

117. Hartschuh, A.; Pedrosa, H. N.; Novotny, L.; Krauss, T. D., Simultaneous fluorescence and Raman scattering from single carbon nanotubes. *Science* **2003,** *301* (5638), 1354-1356.

118. Jorio, A.; Saito, R.; Hafner, J.; Lieber, C.; Hunter, D.; McClure, T.; Dresselhaus, G.; Dresselhaus, M., Structural (n, m) determination of isolated single-wall carbon nanotubes by resonant Raman scattering. *Phys. Rev. Lett.* **2001,** *86* (6), 1118.

119. Milnera, M.; Kürti, J.; Hulman, M.; Kuzmany, H., Periodic resonance excitation and intertube interaction from quasicontinuous distributed helicities in single-wall carbon nanotubes. *Phys. Rev. Lett.* **2000,** *84* (6), 1324.

120. Reich, S.; Thomsen, C., Maultzsch, J. Carbon Nanotubes: *Basic Concepts and Physical Properties*; Wiley-VCH: Weinheim, Germany, 2004.

121. Souza Filho, A.; Chou, S.; Samsonidze, G. G.; Dresselhaus, G.; Dresselhaus, M.; An, L.; Liu, J.; Swan, A. K.; Ünlü, M.; Goldberg, B., Stokes and anti-Stokes Raman spectra of small-diameter isolated carbon nanotubes. *Phys. Rev. B* **2004,** *69* (11), 115428.

122. Reich, S.; Thomsen, C., Raman spectroscopy of graphite. *Phil. Trans. R. Soc. A.* **2004,** *362*, 2271-2288.

123. Telg, H.; Duque, J. G.; Staiger, M.; Tu, X.; Hennrich, F.; Kappes, M. M.; Zheng, M.; Maultzsch, J.; Thomsen, C.; Doorn, S. K., Chiral index dependence of the G+ and G–Raman modes in semiconducting carbon nanotubes. *ACS Nano* **2012,** *6* (1), 904-911.

124. Dubay, O.; Kresse, G.; Kuzmany, H., Phonon softening in metallic nanotubes by a Peierls-like mechanism. *Phys. Rev. Lett.* **2002,** *88* (23), 235506.

125. Lazzeri, M.; Piscanec, S.; Mauri, F.; Ferrari, A.; Robertson, J., Phonon linewidths and electron-phonon coupling in graphite and nanotubes. *Phys. Rev. B* **2006,** *73* (15), 155426.

126. Piscanec, S.; Lazzeri, M.; Robertson, J.; Ferrari, A. C.; Mauri, F., Optical phonons in carbon nanotubes: Kohn anomalies, Peierls distortions, and dynamic effects. *Phys. Rev. B* **2007,** *75* (3), 035427.

127. Kohn, W., Image of the Fermi Surface in the Vibration Spectrum of a Metal. *Phys. Rev. Lett.* **1959,** *2* (9), 393.

128. Kürti, J.; Zólyomi, V.; Grüneis, A.; Kuzmany, H., Double resonant Raman phenomena enhanced by van Hove singularities in single-wall carbon nanotubes. *Phys. Rev. B* **2002,** *65* (16), 165433.

129. Dieing, T.; Hollricher, O.; Toporski, J. *Confocal Raman Microscopy*; Springer: Heidelberg, Germany, Dordrecht, The Netherlands, London, New York, 2011.

130. Saito, R.; Grüneis, A.; Samsonidze, G. G.; Brar, V.; Dresselhaus, G.; Dresselhaus, M.; Jorio, A.; Cançado, L.; Fantini, C.; Pimenta, M., Double resonance Raman spectroscopy of single-wall carbon nanotubes. *New J. Phys.* **2003,** *5* (1), 157.

131. Memming, R., Electron transfer theories. *Semicond. Electrochem.* **2015**, 127-168.

132. Trasatti, S., The absolute electrode potential: an explanatory note. *Pure Appl. Chem.* **1986,** *58* (7), 955-966.

133. Reiss, H., The Fermi level and the redox potential. *J. Phys. Chem.* **1985,** *89* (18), 3783-3791.

134. Ferrari, A. C.; Meyer, J.; Scardaci, V.; Casiraghi, C.; Lazzeri, M.; Mauri, F.; Piscanec, S.; Jiang, D.; Novoselov, K.; Roth, S., Raman spectrum of graphene and graphene layers. *Phys. Rev. Lett.* **2006,** *97* (18), 187401.

135. Pisana, S.; Lazzeri, M.; Casiraghi, C.; Novoselov, K. S.; Geim, A. K.; Ferrari, A. C.; Mauri, F., Breakdown of the adiabatic Born–Oppenheimer approximation in graphene. *Nat. Mater.* **2007,** *6* (3), 198-201.

136. Yan, J.; Zhang, Y.; Kim, P.; Pinczuk, A., Electric field effect tuning of electron-phonon coupling in graphene. *Phys. Rev. Lett.* **2007,** *98* (16), 166802.

137. Maciel, I. O.; Anderson, N.; Pimenta, M. A.; Hartschuh, A.; Qian, H.; Terrones, M.; Terrones, H.; Campos-Delgado, J.; Rao, A. M.; Novotny, L., Electron and phonon renormalization near charged defects in carbon nanotubes. *Nat. Mater.* **2008,** *7* (11), 878-883.

138. Rao, A. M.; Eklund, P.; Bandow, S.; Thess, A.; Smalley, R. E., Evidence for charge transfer in doped carbon nanotube bundles from Raman scattering. *Nature* **1997,** *388* (6639), 257-259.

139. McGuire, K.; Gothard, N.; Gai, P.; Dresselhaus, M.; Sumanasekera, G.; Rao, A., Synthesis and Raman characterization of boron-doped single-walled carbon nanotubes. *Carbon* **2005,** *43* (2), 219-227.

140. Piscanec, S.; Lazzeri, M.; Mauri, F.; Ferrari, A.; Robertson, J., Kohn anomalies and electron-phonon interactions in graphite. *Phys. Rev. Lett.* **2004,** *93* (18), 185503.

141. Das, A.; Pisana, S.; Chakraborty, B.; Piscanec, S.; Saha, S. K.; Waghmare, U. V.; Novoselov, K. S.; Krishnamurthy, H. R.; Geim, A. K.; Ferrari, A. C., Monitoring dopants by Raman scattering in an electrochemically top-gated graphene transistor. *Nat. Nanotechnol.* **2008,** *3* (4), 210-215.

142. Lazzeri, M.; Mauri, F., Nonadiabatic Kohn anomaly in a doped graphene monolayer. *Phys. Rev. Lett.* **2006,** *97* (26), 266407.

143. Popov, V. N.; Lambin, P., Radius and chirality dependence of the radial breathing mode and the G-band phonon modes of single-walled carbon nanotubes. *Phys. Rev. B* **2006,** *73* (8), 085407.

144. Sasaki, K.; Saito, R.; Dresselhaus, G.; Dresselhaus, M. S.; Farhat, H.; Kong, J., Curvature-induced optical phonon frequency shift in metallic carbon nanotubes. *Phys. Rev. B* **2008,** *77* (24), 245441.

145. Nguyen, K. T.; Gaur, A.; Shim, M., Fano lineshape and phonon softening in single isolated metallic carbon nanotubes. *Phys. Rev. Lett.* **2007,** *98* (14), 145504.

146. Farhat, H.; Son, H.; Samsonidze, G. G.; Reich, S.; Dresselhaus, M.; Kong, J., Phonon softening in individual metallic carbon nanotubes due to the Kohn anomaly. *Phys. Rev. Lett.* **2007,** *99* (14), 145506.

147. Tsang, J.; Freitag, M.; Perebeinos, V.; Liu, J.; Avouris, P., Doping and phonon renormalization in carbon nanotubes. *Nat. Nanotechnol.* **2007,** *2* (11), 725-730.

148. Dresselhaus, M. S.; Dresselhaus, G.; Charlier, J. C.; Hernandez, E. Philos. Electronic, thermal and mechanical properties of carbon nanotubes. *Trans. R. Soc. London*, **2004,** *362* (1823), 2065-2098.

149. Avouris, P.; Appenzeller, J.; Martel, R.; Wind, S. J., Carbon nanotube electronics. *Proc. IEEE* **2003,** *91* (11), 1772-1784.

150. Tey, J. N.; Ho, X.; Wei, J., Effect of doping on single-walled carbon nanotubes network of different metallicity. *Nanoscale Res. Lett.* **2012,** *7* (1), 548.

151. Jackson, R.; Domercq, B.; Jain, R.; Kippelen, B.; Graham, S., Stability of doped transparent carbon nanotube electrodes. *Adv. Funct. Mater.* **2008,** *18* (17), 2548-2554.

152. Parekh, B. B.; Fanchini, G.; Eda, G.; Chhowalla, M., Improved conductivity of transparent single-wall carbon nanotube thin films via stable postdeposition functionalization. *Appl. Phys. Lett.* **2007,** *90* (12), 121913.

153. Zhang, Z.-B.; Li, J.; Cabezas, A. L.; Zhang, S.-L. J. C. P. L., Characterization of acid-treated carbon nanotube thin films by means of Raman spectroscopy and field-effect response. *Chem. Phys. Lett.* **2009,** *476* (4-6), 258-261.

154. Zhou, W.; Vavro, J.; Nemes, N. M.; Fischer, J. E.; Borondics, F.; Kamaras, K.; Tanner, D., Charge transfer and Fermi level shift in p-doped single-walled carbon nanotubes. *Phys. Rev. B* **2005,** *71* (20), 205423.

155. Joanis, P.; Tie, M.; Dhirani, A.-A., Influence of low energy barrier contact resistance in charge transport measurements of gold nanoparticle+ dithiol-based self-assembled films. *Langmuir* **2013,** *29* (4), 1264-1272.

156. Choubak, S.; Levesque, P. L.; Gaufres, E.; Biron, M.; Desjardins, P.; Martel, R., Graphene CVD: interplay between growth and etching on morphology and stacking by hydrogen and oxidizing impurities. *J. Phys. Chem. C* **2014,** *118* (37), 21532-21540.

157. Suk, J. W.; Kitt, A.; Magnuson, C. W.; Hao, Y.; Ahmed, S.; An, J.; Swan, A. K.; Goldberg, B. B.; Ruoff, R. S. Transfer of CVD Grown Monolayer Graphene onto Arbitrary Substrates. ACS Nano 2011, 5, 6916–6924.

158. Kingston, C. T.; Jakubek, Z. J.; Dénommée, S.; Simard, B., Efficient laser synthesis of single-walled carbon nanotubes through laser heating of the condensing vaporization plume. *Carbon* **2004,** *42* (8-9), 1657-1664.

159. Gaufrès, E.; Tang, N. W.; Lapointe, F.; Cabana, J.; Nadon, M.-A.; Cottenye, N.; Raymond, F.; Szkopek, T.; Martel, R., Giant Raman scattering from J-aggregated dyes inside carbon nanotubes for multispectral imaging. *Nat. Photonics* **2014,** *8* (1), 72-78.

160. Maghsodi, A.; Hoseini, M. M.; Mobarakeh, M. D.; Kheirmand, M.; Samiee, L.; Shoghi, F.; Kameli, M., Exploration of bimetallic Pt-Pd/C nanoparticles as an electrocatalyst for oxygen reduction reaction. *Appl. Surf. Sci.* **2011,** *257* (15), 6353-6357.

161. Liu, J.; Casavant, M. J.; Cox, M.; Walters, D.; Boul, P.; Lu, W.; Rimberg, A.; Smith, K.; Colbert, D. T.; Smalley, R. E., Controlled deposition of individual single-walled carbon nanotubes on chemically functionalized templates. *Chem. Phys. Lett.* **1999,** *303* (1-2), 125-129.

162. Cabana, J.; Paillet, M.; Martel, R., Directed assembly of SWNTs by electrostatic interactions and its application for making network transistors. *Langmuir* **2010,** *26* (1), 607-612.

163. Wu, Z.; Chen, Z.; Du, X.; Logan, J. M.; Sippel, J.; Nikolou, M.; Kamaras, K.; Reynolds, J. R.; Tanner, D. B.; Hebard, A. F., Transparent, conductive carbon nanotube films. *Science* **2004,** *305* (5688), 1273-1276.

164. McIlvaine, T.C., Preparation of buffers. *J. Biol. Chem* **1921,** *49* (183), 20.

165. Mongay, C.; Cerda, V., Britton–Robinson buffer of known ionic strength. *Ann. Chim.* **1974,** *64*, 409-412.

166. Branca, C.; Frusteri, F.; Magazu, V.; Mangione, A., Characterization of carbon nanotubes by TEM and infrared spectroscopy. *J. Phys. Chem. B* **2004,** *108* (11), 3469-3473.

167. Monteiro-Riviere, N. A.; Nemanich, R. J.; Inman, A. O.; Wang, Y. Y.; Riviere, J. E., Multi-walled carbon nanotube interactions with human epidermal keratinocytes. *Toxicol. Lett.* **2005,** *155* (3), 377-384.

168. Wang, L.; Zhu, X.; Xie, C.; Ding, N.; Weng, X.; Lu, W.; Wei, X.; Li, C., Imaging acidosis in tumors using a pH-activated near-infrared fluorescence probe. *Chem. Commun.* **2012,** *48* (95), 11677-11679.

169. Friedrich, T.; Timmermann, A.; Abe-Ouchi, A.; Bates, N.; Chikamoto, M.; Church, M.; Dore, J.; Gledhill, D.; Gonzalez-Davila, M.; Heinemann, M., Detecting regional anthropogenic trends in ocean acidification against natural variability. *Nat. Clim. Change* **2012,** *2* (3), 167-171.

170. Lauvset, S. K.; Gruber, N.; Landschützer, P.; Olsen, A.; Tjiputra, J. F., Trends and drivers in global surface ocean pH over the past 3 decades. *Biogeosciences* **2015,** *12* (5), 1285-1298.

171. Slessarev, E.; Lin, Y.; Bingham, N.; Johnson, J.; Dai, Y.; Schimel, J.; Chadwick, O., Water balance creates a threshold in soil pH at the global scale. *Nature* **2016,** *540* (7634), 567-569.

172. Duncan, T. V., Applications of nanotechnology in food packaging and food safety: barrier materials, antimicrobials and sensors. *J. Colloid Interface Sci.* **2011,** *363* (1), 1-24.

173. Pacquit, A.; Frisby, J.; Diamond, D.; Lau, K. T.; Farrell, A.; Quilty, B.; Diamond, D., Development of a smart packaging for the monitoring of fish spoilage. *Food Chem.* **2007,** *102* (2), 466-470.

174. Skoog, D. A.; Holler, F. J.; Crouch, S. R. *Instrumental Analysis*, 6th ed.; Brooks/Cole: India, **2007**.

175. Han, J.; Burgess, K., Fluorescent indicators for intracellular pH. *Chem. Rev.* **2010,** *110* (5), 2709-2728.

176. Liu, Y.-S.; Sun, Y.; Vernier, P. T.; Liang, C.-H.; Chong, S. Y. C.; Gundersen, M. A., pH-sensitive photoluminescence of CdSe/ZnSe/ZnS quantum dots in human ovarian cancer cells. *J. Phys. Chem. C* **2007,** *111* (7), 2872-2878.

177. Wu, W.; Shen, J.; Banerjee, P.; Zhou, S., Chitosan-based responsive hybrid nanogels for integration of optical pH-sensing, tumor cell imaging and controlled drug delivery. *Biomaterials* **2010,** *31* (32), 8371-8381.

178. Ferrer-Anglada, N.; Kaempgen, M.; Roth, S., Transparent and flexible carbon nanotube/polypyrrole and carbon nanotube/polyaniline pH sensors. *Phys. Status Solidi* **2006,** *243* (13), 3519-3523.

179. Pietsch, C.; Hoogenboom, R.; Schubert, U. S., Soluble polymeric dual sensor for temperature and pH value. *Angew. Chem.* **2009,** *121* (31), 5763-5766.

180. Safavi, A.; Abdollahi, H., Optical sensor for high pH values. *Anal. Chim. Acta* **1998,** *367* (1-3), 167-173.

181. Zong, C.; Xu, M.; Xu, L.-J.; Wei, T.; Ma, X.; Zheng, X.-S.; Hu, R.; Ren, B., Surface-enhanced Raman spectroscopy for bioanalysis: reliability and challenges. *Chem. Rev.* **2018,** *118* (10), 4946-4980.

182. Dresselhaus, M.; Dresselhaus, G.; Jorio, A., Raman spectroscopy of carbon nanotubes in 1997 and 2007. *J. Phys. Chem. C* **2007,** *111* (48), 17887-17893.

183. Balasubramanian, K.; Burghard, M., Biosensors based on carbon nanotubes. *Anal. Bioanal. Chem.* **2006,** *385* (3), 452-468.

184. Gaufrès, E.; Marcet, S.; Aymong, V.; Tang, N. Y. W.; Favron, A.; Thouin, F.; Allard, C.; Rioux, D.; Cottenye, N.; Verhaegen, M., Hyperspectral Raman imaging using Bragg tunable filters of graphene and other low-dimensional materials. *J. Raman Spectrosc.* **2018,** *49* (1), 174-182.

185. Heller, D. A.; Jeng, E. S.; Yeung, T.-K.; Martinez, B. M.; Moll, A. E.; Gastala, J. B.; Strano, M. S., Optical detection of DNA conformational polymorphism on single-walled carbon nanotubes. *Science* **2006,** *311* (5760), 508-511.

186. Schroeder, V.; Savagatrup, S.; He, M.; Lin, S.; Swager, T. M., Carbon nanotube chemical sensors. *Chem. Rev.* **2018,** *119* (1), 599-663.

187. Anglaret, E.; Dragin, F.; Pénicaud, A.; Martel, R., Raman studies of solutions of single-wall carbon nanotube salts. *J. Phys. Chem. B* **2006,** *110* (9), 3949-3954.

188. Jouguelet, E.; Mathis, C.; Petit, P., Controlling the electronic properties of single-wall carbon nanotubes by chemical doping. *Chem. Phys. Lett.* **2000,** *318* (6), 561-564.

189. Petit, P.; Mathis, C.; Journet, C.; Bernier, P., Tuning and monitoring the electronic structure of carbon nanotubes. *Chem. Phys. Lett.* **1999,** *305* (5-6), 370-374.

190. Zhang, L.; Huang, L.; O'Brien, S. P.; Yu, Z., Electrostatic doping-induced phonon shift of metallic single-wall carbon nanotubes. *J. Phys. Chem. C* **2008,** *112* (51), 20118-20122.

191. Kresse, G.; Dubay, O.; Kuzmany, H. In *phonon softening in metallic nanotubes by a Peierls' like mechanism*, AIP Conference Proceedings, American Institute of Physics: 2002; pp 371-375.

192. Wu, Y.; Maultzsch, J.; Knoesel, E.; Chandra, B.; Huang, M.; Sfeir, M. Y.; Brus, L. E.; Hone, J.; Heinz, T. F., Variable electron-phonon coupling in isolated metallic carbon nanotubes observed by Raman scattering. *Phys. Rev. Lett.* **2007,** *99* (2), 027402.

193. Gao, Y. Q.; Georgievskii, Y.; Marcus, R., On the theory of electron transfer reactions at semiconductor electrode/liquid interfaces. *J. Chem. Phys.* **2000,** *112* (7), 3358-3369.

194. Marcus, R. A., On the theory of oxidation-reduction reactions involving electron transfer. I. *J. Chem. Phys.* **1956,** *24* (5), 966-978.

195. Aguirre, C. M.; Levesque, P. L.; Paillet, M.; Lapointe, F.; St-Antoine, B. C.; Desjardins, P.; Martel, R., The role of the oxygen/water redox couple in suppressing electron conduction in field-effect transistors. *Adv. Mater.* **2009,** *21* (30), 3087-3091.

196. Chakrapani, V.; Angus, J. C.; Anderson, A. B.; Wolter, S. D.; Stoner, B. R.; Sumanasekera, G. U., Charge transfer equilibria between diamond and an aqueous oxygen electrochemical redox couple. *Science* **2007,** *318* (5855), 1424-1430.

197. Cherevko, S.; Zeradjanin, A. R.; Keeley, G. P.; Mayrhofer, K. J., A comparative study on gold and platinum dissolution in acidic and alkaline media. *J. Electrochem. Soc.* **2014,** *161* (12), H822.

198. Zambelli, T.; Barth, J.; Wintterlin, J.; Ertl, G. J. N., Complex pathways in dissociative adsorption of oxygen on platinum. *Nature* **1997,** *390* (6659), 495-497.

199. Yuan, X.-Z.; Wang, H., PEM fuel cell fundamentals. In *PEM fuel cell electrocatalysts and catalyst layers*, Springer: 2008; pp 1-87.

200. Kazaoui, S.; Minami, N.; Matsuda, N.; Kataura, H.; Achiba, Y., Electrochemical tuning of electronic states in single-wall carbon nanotubes studied by in situ absorption spectroscopy and ac resistance. *Appl. Phys. Lett.* **2001,** *78* (22), 3433-3435.

201. Dragin, F.; Pénicaud, A.; Iurlo, M.; Marcaccio, M.; Paolucci, F.; Anglaret, E.; Martel, R., Raman doping profiles of polyelectrolyte SWNTs in solution. *ACS Nano* **2011,** *5* (12), 9892-9897.

202. Sulpizi, M.; Gaigeot, M.-P.; Sprik, M. J., The silica–water interface: how the silanols determine the surface acidity and modulate the water properties. *Chem. Theory Comput.* **2012,** *8* (3), 1037-1047.

203. Bishnoi, S. W.; Rozell, C. J.; Levin, C. S.; Gheith, M. K.; Johnson, B. R.; Johnson, D. H.; Halas, N. J., All-optical nanoscale pH meter. *Nano Lett.* **2006,** *6* (8), 1687-1692.

204. Gotor, R. l.; Ashokkumar, P.; Hecht, M.; Keil, K.; Rurack, K., Optical pH sensor covering the range from pH 0–14 compatible with mobile-device readout and based on a set of rationally designed indicator dyes. *Anal. Chem.* **2017,** *89* (16), 8437-8444.

205. Wang, L.; Li, M.; Li, W.; Han, Y.; Liu, Y.; Li, Z.; Zhang, B.; Pan, D., Rationally designed efficient dual-mode colorimetric/fluorescence sensor based on carbon dots for detection of pH and Cu^{2+} ions. *ACS Sustain. Chem. Eng.* **2018,** *6* (10), 12668-12674.

206. Ortigoza-Diaz, J.; Scholten, K.; Larson, C.; Cobo, A.; Hudson, T.; Yoo, J.; Baldwin, A.; Weltman Hirschberg, A.; Meng, E., Techniques and considerations in the microfabrication of Parylene C microelectromechanical systems. *Micromachines* **2018,** *9* (9), 422.

207. Davis, E. M.; Benetatos, N. M.; Regnault, W. F.; Winey, K. I.; Elabd, Y. A., The influence of thermal history on structure and water transport in Parylene C coatings. *Polymer* **2011,** *52* (23), 5378-5386.

208. Von Metzen, R. P.; Stieglitz, T., The effects of annealing on mechanical, chemical, and physical properties and structural stability of Parylene C. *Biomed. Microdevices* **2013,** *15* (5), 727-735.

209. Vakil, A.; Engheta, N., Transformation optics using graphene. *Science* **2011,** *332* (6035), 1291-1294.

210. Pinto, H.; Markevich, A., Electronic and electrochemical doping of graphene by surface adsorbates. *Beilstein J. Nanotechnol.* **2014,** *5* (1), 1842-1848.

211. Stankovich, S.; Dikin, D. A.; Dommett, G. H.; Kohlhaas, K. M.; Zimney, E. J.; Stach, E. A.; Piner, R. D.; Nguyen, S. T.; Ruoff, R. S., Graphene-based composite materials. *Nature* **2006,** *442* (7100), 282-286.

212. Docherty, C. J.; Lin, C.-T.; Joyce, H. J.; Nicholas, R. J.; Herz, L. M.; Li, L.-J.; Johnston, M. B., Extreme sensitivity of graphene photoconductivity to environmental gases. *Nat. Commun.* **2012,** *3* (1), 1-6.

213. Perreault, F.; De Faria, A. F.; Elimelech, M., Environmental applications of graphene-based nanomaterials. *Chem. Soc. Rev.* **2015,** *44* (16), 5861-5896.

214. Krishnan, S. K.; Singh, E.; Singh, P.; Meyyappan, M.; Nalwa, H. S., A review on graphene-based nanocomposites for electrochemical and fluorescent biosensors. *RSC adv.* **2019,** *9* (16), 8778-8881.

215. Zubiarrain-Laserna, A.; Kruse, P., Graphene-Based Water Quality Sensors. *J. Electrochem. Soc.* **2020,** *167* (3), 037539.

216. Reddy, D.; Register, L. F.; Carpenter, G. D.; Banerjee, S. K., Graphene field-effect transistors. *J. Phys. D: Appl. Phys.* **2011,** *44* (31), 313001.

217. Levesque, P. L.; Sabri, S. S.; Aguirre, C. M.; Guillemette, J.; Siaj, M.; Desjardins, P.; Szkopek, T.; Martel, R., Probing charge transfer at surfaces using graphene transistors. *Nano lett.* **2011,** *11* (1), 132-137.

218. Fu, W.; Nef, C.; Knopfmacher, O.; Tarasov, A.; Weiss, M.; Calame, M.; Schönenberger, C. Graphene Transistors Are Insensitive to pH Changes in Solution. *Nano Lett*. **2011**, 11, 3597–3600

219. Shan, X. N.; Chen, S.; Wang, H.; Chen, Z. X.; Guan, Y.; Wang, Y. X.; Wang, S. P.; Chen, H. Y.; Tao, N. J. Mapping Local Quantum Capacitance and Charged Impurities in Graphene via Plasmonic Impedance Imaging. *Adv. Mater.* **2015**, 27, 6213−6219

220. Fakih, I.; Durnan, O.; Mahvash, F.; Napal, I.; Centeno, A.; Zurutuza, A.; Yargeau, V.; Szkopek, T., Selective ion sensing with high resolution large area graphene field effect transistor arrays. *Nat. Commun.* **2020,** *11* (1), 1-12.

221. Lide, D. R., *CRC handbook of physics and chemistry*. CRC Press, Boca Raton, USA **2001,** *76*, 1995-1996.

222. Sque, S. J.; Jones, R.; Briddon, P. R., The transfer doping of graphite and graphene. *Phys. Status Solidi* **2007,** *204* (9), 3078-3084

223. Barone, V.; Hod, O.; Scuseria, G. E., Electronic structure and stability of semiconducting graphene nanoribbons. *Nano lett.* **2006,** *6* (12), 2748-2754.
224. Whitfield, M., Thermodynamic limitations on the use of the platinum electrode in Eh measurements. *Limnol. Oceanogr.* **1974,** *19* (5), 857-865.